The effect of radiation pressure from massive stars and black holes in the dusty interstellar medium

(ダスト存在下での大質量星やブラックホールからの輻射圧の影響)

Shohei Ishiki (一色 翔平)
Department of Cosmosciences, Graduate School of Science,
Hokkaido University

March 2020

Abstract

Dust is one of the important elements in astrophysics. Radiation pressure on dust grains affects the gas dynamics in star formation and black hole growth. We develop the numerical radiation hydrodynamic code to reveal the effect of radiation pressure from massive stars and black holes in the dusty interstellar medium. The results are as follows:

[1] Radiation feedback in dusty clouds (Ishiki & Okamoto 2017)

We have investigated the impact of photoionization and radiation pressure on a dusty star-forming cloud using one-dimensional radiation hydrodynamic simulations, which include absorption and re-emission of photons by dust. We find that, in a cloud of mass 10^5 $M_\odot$ and radius 17 pc, the effect of radiation pressure is negligible when star formation efficiency is 2 %. The importance of radiation pressure increases with increasing star formation efficiency or an increasing dust-to-gas mass ratio. The net effect of radiation feedback, however, becomes smaller with the increasing dust-to-gas mass ratio, since the absorption of ultra-violet photons by dust grains suppresses photoionization and hence photoheating.

[2] The effect of radiation pressure on spatial distribution of dust inside H_{II} regions (Ishiki et al. 2018)

We investigate the impact of radiation pressure on spatial dust distribution inside H II regions using one-dimensional radiation hydrodynamic simulations, which include absorption and re-emission of photons by dust. In order to investigate grain size effects as well, we introduce two additional fluid components describing large and small dust grains in the simulations. Relative velocity between dust and gas strongly depends on the drag force. We include collisional drag force and coulomb drag force. We find that, in a compact H II region, a dust cavity region is formed by radiation pressure. Resulting dust cavity sizes (~ 0.2 pc) agree with observational estimates reasonably well. In addition, in a cloud of mass 10^5 $M_\odot$, we find that the radiation pressure changes the grain size distribution inside H II regions. Since large (0.1 μm) dust grains are accelerated more efficiently than small (0.01 μm) grains, the large to small grain mass ratio becomes smaller by an order of magnitude compared with the initial one.

[3] Growth of massive black holes in dusty clouds: impacts of relative velocity between dust and gas

We investigate the impacts of the relative motions between dust and gas on the accretion rate onto Intermediate Mass Black Holes (IMBHs) by using one-dimensional radiation hydrodynamic simulations. To investigate the effect of grain size on the gas accretion, we introduce two additional fluid components to gas, which describe large (0.1 μm) and small (0.01 μm) dust grains in the simulations. We find that the accretion rate is reduced due to the radiation force compared with dust free case. We also find that the dust-to-gas mass ratio significantly changes within H II regions because of the relative motions of dust and gas. The decoupling

of dust from gas alleviates the suppression of black hole growth compared with the complete coupling case. This effect may allow moderate growth of black holes even in dusty clouds. In addition, relative motion between dust and gas affects the spectral energy distribution (SED) owing to dust re-emission at wavelength $\lambda \sim 10$ μm.

Contents

Chapter 1

Introduction

Dust plays an important role in astrophysics. The existence of interstellar dust grains in the universe is firstly inferred by Trumpler (1930). Resent observation indicates that dust exist not only in the Milky Way but also in high redshift galaxies at $z \gtrsim 7$ (e.g. z=7.5, Watson et al. 2015; z=7.2, Hashimoto et al. 2019; z=8.3, Tamura et al. 2019).

Interstellar dust grain is the solid particle and its size is $\lesssim 1$ μm. Some important roles of dust in astrophysics are as follows:

1. Radiation pressure on dust grains
2. Absorption and scattering of photons from radiation sources
3. Infrared re-emission from dust grains
4. Photoelectric grain heating in interstellar medium
5. Chemical reaction on grain surface

Radiation pressure on dust affects the dusty gas dynamics. For example, Okamoto et al. (2014) concluded that radiation pressure on dust grains plays an important role on galaxy evolution. Absorption and scattering of photons from radiation sources affect the observation results. By detecting infrared re-emission from dust grains, we are able to analyse Galactic structures (e.g. Schlegel et al. 1998) or star formation in galaxies (e.g. Kennicutt 1998). Photoelectric grain heating is one of the important heating processes of the dusty gas in the interstellar medium (Draine 1978) and may suppress the star formation in dwarf galaxies (Forbes et al. 2016). The molecular gas plays a crucial role in star formations. The molecular hydrogen is one of the dominant elements in molecular gas and it is efficiently formed on grain surface (e.g. Gould & Salpeter 1963; Katz et al. 1999).

In this thesis, we mainly investigate the effect of radiation pressure from massive stars and black holes in the dusty interstellar medium.

1.1 Properties of dust and dust grain size distribution

In this section, we mainly discuss the important properties of dust grains.

1.1.1 Composition and size of dust grains

Mathis et al. (1977) and Draine & Lee (1984) showed that following dust grain model reproduces the extinction feature from the infrared to the ultraviolet wavelength:

1. Dust is consist of silicate and graphite.
2. Dust grain size distribution is $dn(a_{\rm d})/da_{\rm d} \propto a_{\rm d}^{-3.5}$ for $a_{\rm min,d} < a_{\rm d} < a_{\rm max,d}$, where $a_{\rm d}$ is dust grain size, $a_{\rm min,d} (\simeq 0.005\ \mu{\rm m})$ is the minimum dust grain size, $a_{\rm max,d} (\simeq 0.25\ \mu{\rm m})$ is the maximum dust grain size, and $n(a_{\rm d})da_{\rm d}$ is the number of dust within size $(a_{\rm d},\ a_{\rm d} + da_{\rm d})$. We call this power-law size distribution as the Mathis-Rumpl-Nordsieck (MRN) size distribution (Mathis et al. 1977).

Weingartner & Draine (2001b), however, suggested that dust grain size distribution is not simple and depends on the environment of interstellar medium.

1.1.2 Dust formation and size evolution in galaxies

In order to reveal the dust formation and size evolution history in galaxies, Asano et al. (2013a;b) constructed the dust evolution model considering the dust formation processes and dust grain size evolution processes. They concluded that following dust production and evolution processes affects the amount of dust and its size distribution in galaxies: (i) the dust production by Type II supernovae (SNe II), (ii) the dust production by asymptotic giant branch (AGB) stars, (iii) dust destruction by SN shocks, (iv) metal accretion onto the surface of dust-grains (i.e. grain growth), (v) coagulation, and (vi) shattering. Since calculating the full evolution of dust grain size distribution in galaxy scales is computationally heavy, Hirashita (2015) developed the two-size approximation model to calculate the grain size evolution in galaxies.

Using the dust formation and size evolution model developed by Hirashita (2015), Aoyama et al. (2017) and Hou et al. (2017) performed the numerical simulation including the dust grain size evolution in isolated galaxies. They showed that their numerical simulations reproduce the extinction feature (i.e. extinction curve) of the Milky Way by including their dust grain size evolution model. In addition, their results broadly reproduce the radial gradient of dust-to-gas mass ratio in nearby galaxies. These results indicate that dust model of Asano et al. (2013b;a) and Hirashita (2015) broadly explain the dust formation and evolution in galaxies. However, Hou et al. (2017) was not able to reproduce the extinction curves in Large/Small Magellanic Clouds (LMC/SMC).

In order to reveal the dust properties in LMC and SMC, Bekki et al. (2015) performed one-zone numerical simulations including chemical evolutions and dust grain evolution model (Hirashita 2015). They concluded that extinction curves in LMC and SMC are able to be reproduced if small carbon grains ($a_{\rm d} < 0.03\ \mu{\rm m}$) is selectively removed. In other words, they indicated that relative motion between dust grains and gas may be also important.

1.1.3 Relative motion between dust grains and gas in HII regions near massive stars

Relative motion between dust grains and gas is also suggested by observations. Inoue (2002) argued that the presence of the central dust cavity region in compact/ultra-compact H II regions. He also argued that radiation pressure or stellar wind from stars selectively remove the dust grains from the centre of H II regions.

Akimkin et al. (2015; 2017) assumed the relative motion between dust and gas and performed the radiation hydrodynamic simulations around massive stars. In their numerical simulations, they included the effect of coulomb drag force and collisional drag force in order to determine the relative velocity between dust and gas. They showed the following results: (i) Radiation pressure selectively removes dust grains from the centre of H II regions and forms dust cavity regions. (ii) Coulomb drag force has stronger effect on relative motion between dust and gas than collisional drag force. (iii) Since radiation pressure and drag force strongly depend on dust grain size, relative motion changes dust grain size distribution inside H II regions. They, however, do not compare their simulation results with observational data, such as dust cavity size in H II regions.

1.2 The effect of radiation pressure and dust grains on gas dynamics

In this section, we mainly discuss the effect of radiation pressure on dust grains in gas dynamics.

1.2.1 Galaxy formation and evolutions

Radiation from young massive stars affects the galaxy evolution mainly by two processes: photoionization heating (i.e. thermal pressure) and radiation pressure.

Ultraviolet (UV) photons from young massive stars ionize the surrounding neutral gas and form H II regions (i.e. ionized regions). UV photons also increase gas temperature by photoionization heating. Since the gas temperature increases, and hence thermal pressure increases, the H II region expands. This process disperses star-forming clouds (Walch et al. 2012) and changes star formation efficiency (Mac Low & Klessen 2004; McKee & Ostriker 2007).

By absorbing photons from young stars, dust grains acquire momentum. The momentum pushes the material outward and may drive galaxy scale outflows (e.g. Murray et al. 2005; Oppenheimer & Davé 2006). This process suppress the star formation in galaxies and affects galaxy evolutions (e.g. Hopkins et al. 2011; Brook et al. 2012; Stinson et al. 2013; Agertz et al. 2013; Okamoto et al. 2014).

Krumholz & Matzner (2009) compared the relative importance of photoionization heating and radiation pressure analytically. They revealed the condition which process, radiation pressure or photoionization heating, becomes important. Sales et al. (2014), then, performed the numerical radiation hydrodynamic simulations and concluded that radiation pressure is negligible compare with pho-

toionization heating. Sales et al. (2014), however, did not include the dust in their simulations.

1.2.2 Black hole evolutions

Revealing the formation process of suppermassive black holes (SMBHs) is one of the big challenges in modern astrophysics. Recent observation indicated that SMBHs are already formed even at redshift $z \gtrsim 6$ (Mortlock et al. 2011; Wu et al. 2015). Formation process of those SMBHs at high redshift is, however, not well known.

It is widely believed that gas accretion onto black holes is one of the important process to form the SMBHs (e.g. Haiman 2013). When gas accretes onto black holes, an accretion disk is formed and emits strong radiation. The radiative luminosity from an accretion disk is defined as follows:

$$L_{\rm acc} = \eta \dot{m} c^2, \tag{1.1}$$

where η is constant radiative efficiency, $\dot{m}$ is accretion rate, and c is speed of light. This radiation prevents the gas accreting onto black holes.

One of the important parameter to determine the accretion rate is Eddington luminosity. Eddington luminosity is the luminosity when radiation pressure and gravitational force is equal. For example, Eddington luminosity of primordial gas is defined as follows:

$$L_{\rm Edd} \equiv \frac{4\pi G M_{\rm BH} m_{\rm p} c}{\sigma_{\rm T}}, \tag{1.2}$$

where G is the gravitational constant, $M_{\rm BH}$ is black hole mass, $m_{\rm p}$ is the proton mass, and $\sigma_{\rm T}$ is the Thomson cross section.

Since radiation pressure on dust also prevents the dusty gas accreting onto the black holes, Eddington luminosity of dusty gas becomes as follows:

$$L^*_{\rm Edd}(Z) \equiv \frac{4\pi G M_{\rm BH} m_{\rm p} c}{\sigma_{\rm T} + D(Z)\sigma_{\rm dust}}, \tag{1.3}$$

where $D(Z)$ is dust-to-gas mass ratio and $\sigma_{\rm dust}$ is the cross section of dust grains. Accretion rate of dusty gas onto black holes, therefore, becomes small if the gas includes the large amount of dust grains. In other words, accretion rate of dusty gas onto black holes may increase by removing dust grains from black hole neighbor.

1.3 Basic physics

In this section, we explain the important physics for radiation pressure and relative motion between dust grains and gas.

1.3.1 Absorption cross section of dust grains

Radiation pressure on dust grains strongly depends on absorption cross section. Absorption cross section $\sigma_{\rm d}$ of dust grains with radius $a_{\rm d}$ is

$$\sigma_{\rm d} = \pi a_{\rm d}^2 Q_{\rm abs}(a_{\rm d}), \tag{1.4}$$

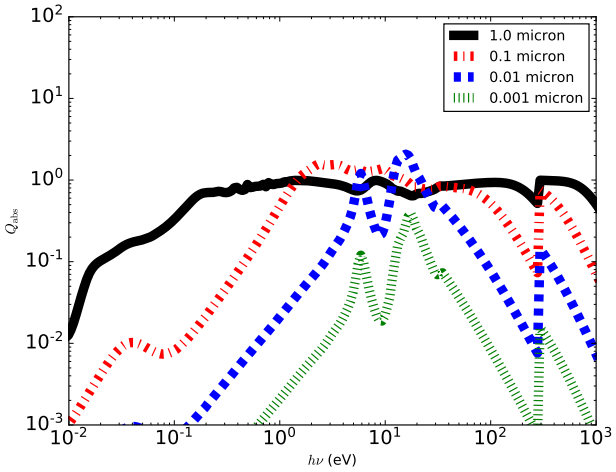

Figure 1.1: Absorption coefficient $Q_{\rm abs}$ for spherical graphite grains as functions of wavelength and dust radius. Black solid line, red dot-dashed line, blue dashed line, and green dotted line represent absorption coefficient for graphite grains with radius 1.0 μm, 0.1 μm, 0.01 μm, and 0.001 μm, respectively. (Draine & Lee 1984; Laor & Draine 1993)

where $Q_{\rm abs}(a_{\rm d})$ is absorption coefficient of dust grains with radius $a_{\rm d}$.

Fig. 1.1 shows the absorption coefficient for graphite grains as a function of wavelength and grain size. Larger dust grains have larger absorption coefficient than smaller dust grains with ionization photons ($h\nu \gtrsim 30$ eV).

1.3.2 Drag force

Drag force plays an important role to determine the relative velocity between dust and gas. The drag force $F_{\rm drag}$ on a dust of charge $Z_{\rm d}$ and radius $a_{\rm d}$ is defined as follows (Draine & Salpeter 1979):

$$F_{\rm drag} = 2\pi a_{\rm d}^2 k_{\rm B} T_{\rm g} \left[\sum_{\rm i} n_{\rm i} \left(G_0(s_{\rm i}) + z_{\rm i}^2 \phi^2 \ln(\Lambda/z_{\rm i}) G_2(s_{\rm i}) \right) \right], \tag{1.5}$$

where

$$\begin{aligned} s_{\rm i} &\equiv \sqrt{m_{\rm i}(v_{\rm i} - v_{\rm d})^2/(2k_{\rm B}T_{\rm g})}, \\ G_0(s_{\rm i}) &\approx 8s_{\rm i}/(3\sqrt{\pi})\sqrt{1 + 9\pi s_{\rm i}^2/64}, \\ G_2(s_{\rm i}) &\approx s_{\rm i}/(3\sqrt{\pi}/4 + s_{\rm i}^3), \\ \phi &\equiv Z_{\rm d} e^2/(a_{\rm d} k_{\rm B} T_{\rm g}), \\ \Lambda &\equiv 3/(2a_{\rm d} e|\phi|)\sqrt{k_{\rm B}T_{\rm g}/\pi n_{\rm e}}, \end{aligned}$$

$k_{\rm B}$ is Boltzmann constant, $T_{\rm g}$ is the temperature of gas, $n_{\rm i}$ is the number density of ith gas species (i =H I, H II, He I, He II, and He III), $v_{\rm i}$ is the velocity of ith

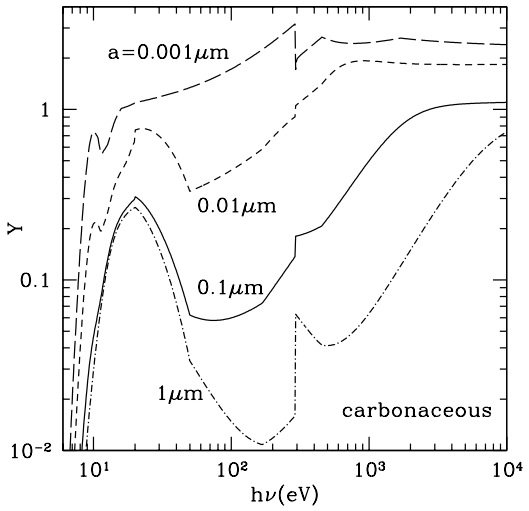

Figure 1.2: Photoelectric yield Y for uncharged carbonaceous grains as functions of photon energy and dust grain radius. (Weingartner et al. 2006)

species, $n_{\rm e}$ is the number density of electron, $z_{\rm i}$ is the charge of ith species, and $m_{\rm i}$ is the mass of ith species. First term of the equation (1.5) is the collisional drag force and second term is the coulomb drag force.

1.3.3 Dust charge

Since coulomb drag force depends on the grain electric potential, we have to determine the dust grain charge. The dust grain charge $Q_{\rm d}(\equiv Z_{\rm d}e)$ is derived as follows:

$$\frac{dQ_{\rm d}}{dt} = e(J_{\rm pe} + \sum_{\rm j} J_{\rm j}), \tag{1.6}$$

where e is electric charge, $J_{\rm pe}$ is the photoemission rate, and $J_{\rm j}$ is the collisional charging rate by ions or electrons.

The photoemission rate is derived as follows (Weingartner & Draine 2001a; Weingartner et al. 2006):

$$J_{\rm pe} = \pi a_{\rm d}^2 \int d\nu \frac{cu_\nu}{h\nu} Q_{\rm abs} Y, \tag{1.7}$$

where $a_{\rm d}$ is dust grain radius, ν is frequency, c is speed of light, u_ν is radiation density per unit frequency range, $Q_{\rm abs}$ is absorption coefficient of dust grains, and Y is photoelectric yield. Fig. 1.2 shows the photoelectric yield Y of uncharged carbonaceous grains as a functions of photon energy and dust grain radius (Weingartner et al. 2006). Small dust grains tend to have large photoelectric yield compared with large dust grains.

The collisional charge rate of species j (j =H II, He II, He III, e) with charge

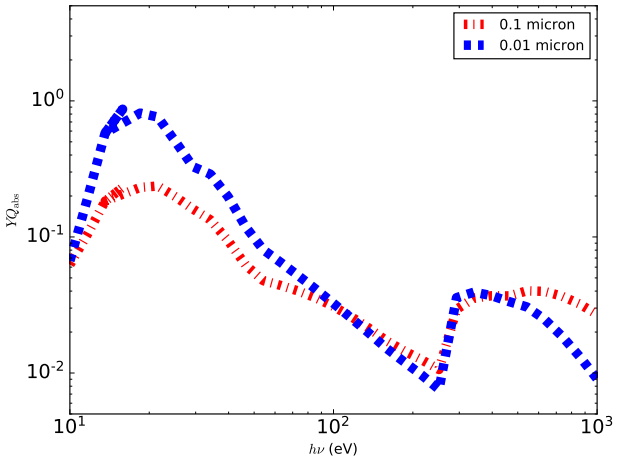

Figure 1.3: Photoelectric yield times absorption coefficient $YQ_{\rm abs,d}$ for uncharged carbonaceous grains as functions of photon energy and dust grain radius. Red dot-dashed line and blue dashed line represent $YQ_{\rm abs,d}$ for graphite grains with radius 0.1 μm and 0.01 μm, respectively.

$Z_{\rm j}e$ is:

$$J_{\rm j} = (Z_{\rm j}s_{\rm j} + \delta_{\rm j})n_j\sqrt{\frac{8k_{\rm B}T_{\rm g}}{\pi m_j}}\pi a_{\rm d}^2 g(Z_{\rm j}\phi), \tag{1.8}$$

where $s_{\rm j}$ is the sticking coefficients for species j, $\delta_{\rm j}$ is the secondary electron coefficient of ions or the effective secondary emission coefficient of electrons, $n_{\rm j}$ is the number density of species j, $k_{\rm B}$ is Boltzmann constant, $T_{\rm g}$ is temperature of gas, $m_{\rm j}$ is the mass of species j, and

$$g(x) = \begin{cases} {\rm e}^{-{\rm x}} \ (x > 0), \\ 1 - x, (x < 0). \end{cases}$$

From equations (1.6), (1.7), and (1.8), $YQ_{\rm abs,d}$ is one of the important factor to determine the electric potential of dust grains. Fig. 1.3 shows the $YQ_{\rm abs,d}$ of uncharged graphite grains as a functions of photon energy and dust grain radius. Small dust grains, therefore, tends to have larger electric potential than large dust if photons with 10 eV $\lesssim h\nu \lesssim 10^2$ eV are dominant factor to determine the electric potential.

1.3.4 Hydrodynamics

By solving the hydrodynamic equations, the spatial distribution of dust grains and gas is determined. Hydrodynamics equations of dust and gas are as follows:

$$
\begin{aligned}
\frac{\partial}{\partial t}\rho_{\rm g} + \frac{\partial}{\partial x}\rho_{\rm g} v_{\rm g} &= 0 \\
\frac{\partial}{\partial t}\rho_{\rm d,k} + \frac{\partial}{\partial x}\rho_{\rm d,k} v_{\rm d,k} &= 0 \\
\frac{\partial}{\partial t}\rho_{\rm g} v_{\rm g} + \frac{\partial}{\partial x}\rho_{\rm g} v_{\rm g}^2 &= \rho_{\rm g} a_{\rm gra} + f_{\rm rad,g} - \frac{\partial}{\partial x} P_{\rm g} \\
&\quad \sum_{\rm k} K_{\rm d,k}(v_{\rm d,k} - v_{\rm g}) \\
\frac{\partial}{\partial t}\rho_{\rm d,k} v_{\rm d,k} + \frac{\partial}{\partial x}\rho_{\rm d,k} v_{\rm d,k}^2 &= \rho_{\rm d,k} a_{\rm gra} + f_{\rm rad,d,k} \\
&\quad + K_{\rm d,k}(v_{\rm g} - v_{\rm d,k}) \\
\frac{\partial}{\partial t}\left(\frac{1}{2}\rho_{\rm g} v_{\rm g}^2 + e_{\rm g}\right) &+ \sum_{\rm k} \frac{\partial}{\partial t}\left(\frac{1}{2}\rho_{\rm d,k} v_{\rm d,k}^2\right) \\
+\frac{\partial}{\partial x}\left(\frac{1}{2}\rho_{\rm g} v_{\rm g}^2 + h_{\rm g}\right) v_{\rm g} &+ \sum_{\rm k} \frac{\partial}{\partial x}\left(\frac{1}{2}\rho_{\rm d,k} v_{\rm d,k}^3\right) \\
&= \left(\rho_{\rm g} v_{\rm g} + \sum_{\rm k} \rho_{\rm d,k} v_{\rm d,k}\right) a_{\rm gra} \\
&\quad + f_{\rm rad,g} v_{\rm g} + \sum_{\rm k} f_{\rm rad,d,k} v_{\rm d,k} + (\Gamma - \Lambda)
\end{aligned}
$$

where $\rho_{\rm g}$ is the mass density of gas, $\rho_{\rm d,k}$ is the mass density of dust-k, $v_{\rm g}$ is the velocity of gas, $v_{\rm d,k}$ is the velocity of dust-k, $a_{\rm gra}$ is the gravitational acceleration, $f_{\rm rad,g}$ is the radiation pressure gradient force on gas, $f_{\rm rad,d,k}$ is the radiation pressure gradient force on dust-k, $K_{\rm d,k}$ is the drag coefficient between gas and dust-k, $e_{\rm g}$ is the internal energy of gas, $h_{\rm g}$ is the enthalpy of gas, Γ is the heating rate by radiation, and Λ is the cooling rate by gas.

The drag coefficient $K_{\rm d}$ between gas and dust is defined as follows:

$$
K_{\rm d} \equiv \frac{n_{\rm d} F_{\rm drag}}{|\boldsymbol{v}_{\rm d} - \boldsymbol{v}_{\rm g}|}, \tag{1.9}
$$

where $n_{\rm d}$ is the number density of dust grains, and $v_{\rm d}$ is the velocity of dust grains.

Radiation pressure gradient force $f_{\rm rad,p}$ on species p is defined as follows:

$$
f_{\rm rad} = \frac{n_{\rm p}}{c} \int d\nu \int d\Omega \sigma_{\nu,p} I_\nu \cos^2\theta, \tag{1.10}
$$

where $n_{\rm p}$ is number density of species p, $\sigma_{\rm p}$ is cross section of species p, $d\Omega$ is a solid angle, and I_ν is the specific intensity (i.e. brightness). The detail description of I_ν is in section 2.3.1.

Heating Γ and cooling Λ are depend on ionization state of gas and strength of radiation field. The detail descriptions of Γ and Λ are in section 2.3.2.

For completely coupled case (i.e. $K_{\rm d,k} \to \infty$), hydrodynamics equations becomes as follows:

$$\begin{aligned}
\frac{\partial}{\partial t}\rho + \frac{\partial}{\partial x}\rho v &= 0 \\
\frac{\partial}{\partial t}\rho v + \frac{\partial}{\partial x}\rho v^2 &= \rho a_{\rm gra} + f_{\rm rad} - \frac{\partial}{\partial x}P_{\rm g} \\
\frac{\partial}{\partial t}\left(\frac{1}{2}\rho v^2 + e_{\rm g}\right) + \frac{\partial}{\partial x}\left(\frac{1}{2}\rho v^2 + h_{\rm g}\right) v &= \left(\rho a_{\rm gra} + f_{\rm rad}\right) v + (\Gamma - \Lambda),
\end{aligned}$$

where v is the velocity of gas and dust,

$$\begin{aligned}
\rho &\equiv \rho_{\rm g} + \sum_{\rm k} \rho_{\rm d,k}, \\
f_{\rm rad} &\equiv f_{\rm rad,g} + \sum_{\rm k} f_{\rm rad,d,k}.
\end{aligned}$$

1.4 Aim of this thesis

We develop the numerical radiation hydrodynamic code to reveal the effect of radiation pressure from massive stars and black holes in the dusty interstellar medium.

In this thesis we focus on following themes:

1. The effect of radiation pressure on dusty clouds
2. Relative motion between dust grains and gas around massive stars
3. Relative motion between dust grains and gas around black holes

In the first theme (chapter 2), as we discussed in section 1.2.1, relative importance of photoionization heating and radiation pressure is not discussed by radiation hydrodynamic simulations including dust grains. We, therefore, perform numerical hydrodynamic simulations with dust grains and reveal the relative importance of radiation pressure and photoionization heating. In this chapter, we assume that dust and gas are completely coupled (i.e. $K_{\rm d} \to \infty$), since we are interested in the relative importance of radiation pressure and photoionization heating and spatial distribution of dust-to-gas mass ratio is not important.

In the second theme (chapter 3), as we discuss in section 1.1.2, relative motion between dust grains and gas may be an important process for understanding dust properties. As discussed in section 1.1.3, radiation pressure may play the key role in the relative motion between dust grains and gas inside H II regions. We, therefore, perform radiation hydrodynamic simulations assuming relative motion between dust and gas and compare our numerical simulation results and observational estimates in order to confirm the role of radiation pressure in the spatial distribution of dust grains inside H II regions.

In the third theme (chapter 4), as we discuss in section 1.2.2, the amount of dust grains strongly affects the gas accretion rate onto black holes. We, therefore, perform radiation hydrodynamic simulations including the relative motion between dust grains and gas and reveal the effect of relative motion on dusty gas accretion rate.

Chapter 2

Radiation feedback in dusty clouds

2.1 Abstract

We have investigated the impact of photoionization and radiation pressure on a dusty star-forming cloud using one-dimensional radiation hydrodynamic simulations, which include absorption and re-emission of photons by dust. We find that, in a cloud of mass 10^5 $M_\odot$ and radius 17 pc, the effect of radiation pressure is negligible when star formation efficiency is 2 %. The importance of radiation pressure increases with increasing star formation efficiency or an increasing dust-to-gas mass ratio. The net effect of radiation feedback, however, becomes smaller with the increasing dust-to-gas mass ratio, since the absorption of ultra-violet photons by dust grains suppresses photoionization and hence photoheating.

2.2 Introduction

Radiative transfer is known to be very important in many astrophysical phenomena. Feedback from young, massive stars plays a crucial role in determining star formation activity and galaxy evolution. The energy and momentum input by stellar radiation from young, massive stars is most influential in a star-forming cloud before the explosion of the first supernova.

The radiation from young, massive stars can affect the surrounding medium through two channels. First, ultraviolet (UV) photons ionize the surrounding neutral gas and increase its temperature by photoheating.

The H II region expands owing to the increased thermal pressure. This process disperses star-forming clouds (Walch et al. 2012) and changes star formation efficiency (Mac Low & Klessen 2004; McKee & Ostriker 2007). Secondly, neutral gas and dust absorb photons and acquire their momentum. The momentum pushes the material outward. This process may drive galaxy scale outflows (Murray et al. 2005; Oppenheimer & Davé 2006). The ionization feedback (Dale et al. 2007; Peters et al. 2010; Dale et al. 2012; Hosokawa et al. 2015) and radiation pressure feedback (Krumholz et al. 2007; Kuiper et al. 2010b; 2011; 2012; Kuiper & Yorke

2013; Harries et al. 2014) are also important for individual star formation.

Recently, Sales et al. (2014) have studied these processes and have concluded that radiation pressure has negligible effect compared with photoheating. They, however, do not include dust in their simulations. On the other hand, Wise et al. (2012) perform radiation hydrodynamic simulations in full cosmological context and show that momentum input partially affect star formation by increasing the turbulent support in early low-mass galaxies, while they ignore the dust since dust is unimportant in these low metallicity systems.

The presence of dust increases the importance of radiation pressure because, unlike hydrogen and helium, dust can always absorb UV photons. Moreover, absorbed photons are re-radiated as infrared (IR) photons and again dust absorbs IR photons. Iterative process of the absorption and the re-emission increases the efficiency of converting photon energy to dust momentum. The creation of H II regions by UV radiation and momentum-driven gas outflows by absorption of re-emitted IR photons now become important ingredients in galaxy formation simulations, which are modelled as phenomenological subgrid physics (e.g. Hopkins et al. 2011; Brook et al. 2012; Stinson et al. 2013; Agertz et al. 2013; Okamoto et al. 2014).

It is therefore important to investigate the radiative feedback by radiation hydrodynamic simulations that include re-emission from dust grains. To this end, we perform one-dimensional radiation hydrodynamic simulations in the presence of dust. In this chapter, we solve radiation transfer including angular dependence in order to deal with re-emission from dust and gas.

2.3 Methods

We place a radiation source at the centre of a spherically symmetric gas distribution. To compare the effect of thermal and radiation pressure, we perform simulations with and without radiation pressure and investigate relative importance of these processes.

2.3.1 Radiation transfer

We here describe the algorithm that we use to solve the steady radiative transfer equation for a given frequency, ν:

$$\frac{dI_\nu}{d\tau_\nu} = -I_\nu + S_\nu, \tag{2.1}$$

where I_ν, τ_ν, and S_ν are the specific intensity, the optical depth, and the source function, respectively. Optical depth of a ray segment, $\Delta\tau_\nu$, is determined as

$$\Delta\tau_\nu = \kappa_\nu \Delta x = \sum_i n_i \sigma_i \Delta x, \tag{2.2}$$

where κ_ν, n_i, and σ_i are the absorption coefficient, the number density, and the cross section of ith species of interest, respectively, and Δx is the length of the

ray segment that intersects the cell. The species we include in our simulations are H I, H II, He I, He II, He III, electrons, and dust. We employ the cross-sections of H I, He I, and He II given in Osterbrock D. E. (2006) and that of dust in Draine & Lee (1984) and Laor & Draine (1993)[1].

The recombination radiation from ionized hydrogen and helium is calculated as

$$\frac{S_{\nu,i}}{\kappa_\nu} = \frac{\alpha_i(T) n_\mathrm{e} n_i h\nu}{4\pi\sqrt{\pi}\Delta\nu_{\mathrm{D},i}} \mathrm{e}^{-(\nu-\nu_0)^2/(\Delta\nu_\mathrm{D})^2}, \tag{2.3}$$

where h is the plank constant, α_i is the recombination coefficient for a transition from ionized state to ground state, $\nu_{0,i}$ is the threshold frequency of the ith species, n_e is the electron number density, T is gas temperature, and $\Delta\nu_{\mathrm{D},i}$ is the Doppler width defined as:

$$\Delta\nu_{\mathrm{D},i} = \frac{\nu_0}{c}\sqrt{\frac{2kT}{m_i}}, \tag{2.4}$$

where k is the Boltzmann constant and c is the speed of light. For spherically symmetric systems, intensities are functions of radius and angle if the problem involves re-emission of photons as in our case. We therefore employ a scheme called the impact parameter method (Hummer & Rybicki 1971).

2.3.2 Chemical reactions and radiative heating and cooling

In our simulations, we solve a network of chemistry consists of H I, H II, He I, He II, He III, and electrons, which can be described by a following set of equations:

$$\frac{dn_i}{dt} = C_i - D_i n_i, \tag{2.5}$$

where n_i is number density of the ith species, C_i is the collective source term responsible for the creation of the ith species, and the second term involving D_i represents the destruction mechanisms for the ith species. Since equation (2.5) is a stiff set of differential equations, we need an implicit scheme for solving them. We thus employ a backward difference formula (Anninos et al. 1997; Okamoto et al. 2012):

$$n_i^{t+\Delta t} = \frac{C_i^{t+\Delta t} + n_i^t}{1 + D_i^{t+\Delta t}\Delta t}, \tag{2.6}$$

where $C_i^{t+\Delta t}$ and $D_i^{t+\Delta t}$ are evaluated at the advanced timestep. Unfortunately, not all source terms can be evaluated at the advanced timestep due to the intrinsic non-linearity of equation (2.5). We thus sequentially update the number densities of all species in the order of increasing ionization states.

The chemical reactions included in our simulations are the recombination (Hummer 1994; Hummer & Storey 1998), the collisional ionization (Janev et al. 1987; Abel et al. 1997), the dielectronic recombination (Aldrovandi & Pequignot 1973), and the photoionization (Cen 1992).

[1] http://www.astro.princeton.edu/ draine/dust/dust.diel.html

In order to determine the temperature of gas, we consider following radiative cooling and heating processes: the photoionization heating, the collisional ionization cooling, the dielectronic recombination cooling, the collisional excitation cooling (Cen 1992); the bremsstrahlung cooling (Hummer 1994); and the inverse Compton cooling (Ikeuchi & Ostriker 1986) by assuming the cosmic microwave background radiation at $z = 0$. Collisions between gas and dust grains and heating due to photoejection from grains (Yorke & Welz 1996) are not included in our simulations. We integrate the energy equation of gas implicitly as described in Okamoto et al. (2012).

2.3.3 Dust

We include absorption and thermal emission of photons by dust grains in our simulations. To convert mass density to number density, we assume a graphite grain whose size and density are $0.1\,\mu$m and $1.0\,\mathrm{g\,cm^3}$, respectively, as a typical dust particle (Draine 2011a). Dust temperature is determined by the radiative equilibrium, and thus the dust temperature is independent from gas temperature. We assume that the dust sublimation temperature is 1500 K; however, dust never be heated to this temperature in our simulations. We do not include photon scattering by dust grains for simplicity. Neglecting this process may overestimate the radiation pressure on dust grains as we will discuss later.

2.3.4 Time stepping

Since we have to solve the static radiative transfer equation, the chemical reaction, and energy equations for gas and dust simultaneously. We thus iteratively solve these equations (Okamoto et al. 2012; Tanaka et al. 2015) until the relative difference in the electron number density, n_e, and in the dust temperature, T_d in all cells become smaller than 0.5 %.

For this implicit time integration, we employ a timestep that is defined by the time-scale of the chemical reactions:

$$\Delta t_{\mathrm{chem},k} = 0.1 \left| \frac{n_\mathrm{e}}{\dot{n}_\mathrm{e}} \right|_k + 1 \times 10^{-3} \left| \frac{n_\mathrm{H}}{\dot{n}_\mathrm{H}} \right|_k \tag{2.7}$$

where the subscript, k, denotes the cell number. The second term in the right-hand side prevents the timestep from becoming too short when the medium is almost neutral. We follow the evolution of the system with the minimum of the individual chemical timestep, $\Delta t_\mathrm{chem} = \min(\Delta t_{\mathrm{chem},k})$, if this timestep is shorter than a timestep defined by the Courant-Friedrichs-Lewy (CFL) condition.

2.3.5 Hydrodynamics

Hydrodynamics is solved by using a scheme called AUSM+ (Liou 1996) in the second order accuracy in space and time. In order to prevent cell density from becoming zero or a negative value, we set the minimum number density, $n_\mathrm{H} \simeq 10^{-10}\ \mathrm{cm^{-3}}$. We have confirmed that our results are not sensitive to the choice of

the threshold density as long as the threshold density is sufficiently low. Throughout this chapter, we assume that dust and gas are dynamically tightly coupled. We have performed test simulations described in Bisbas et al. (2015) and confirmed that our code reproduces their results.

2.3.6 Relative importance of radiation pressure and thermal pressure

Krumholz & Matzner (2009) introduce a parameter, ζ, for quantifying the relative importance of radiation pressure and thermal pressure. The parameter is defined as

$$\zeta = \frac{r_{\rm ch}}{r_{\rm St}}, \tag{2.8}$$

where $r_{\rm ch}$ is the radius at which the thermal pressure and the radiation pressure forces on an expanding shell are equal and $r_{\rm St}$ is the Strömgren radius calculated for the initial density distribution. For $\zeta > 1$, the expansion becomes radiation pressure dominated. In general, the value of ζ increases with luminosity of a radiation source and a dust-to-gas mass ratio. We estimate ζ for each simulation to compare our numerical results with the analytic predictions. To calculate $r_{\rm ch}$, we need to know how many times on average a photon is absorbed or scattered in a shell, $f_{\rm trap}$ (Krumholz & Matzner 2009). We estimate this value by an iterative procedure and obtain $f_{\rm trap} = 1$ for all our simulations.

2.4 Simulation setup

Table 2.1: Initial conditions and numerical setup for simulations. The radius and the total mass of each cloud are indicated by $r_{\rm cloud}$ and $M_{\rm total}$. The number densities, $n_{\rm H}$, $n_{\rm He}$, and $n_{\rm d}$ indicate the initial number densities of hydrogen, helium, and dust in the innermost cell, respectively. The initial temperature of gas and dust are represented by $T_{\rm g}$ and $T_{\rm d}$, respectively. The mass of a central radiation source, which determines the luminosity, is indicated by $M_{\rm star}$. The dust optical depths from the centre to $r_{\rm cloud}$ at 3.29×10^{15} and 1.76×10^{13} Hz are, respectively, shown as $\tau_{\rm d,UV}$ and $\tau_{\rm d,IR}$.

Cloud	$r_{\rm cloud}$ (pc)	$M_{\rm total}$ ($M_\odot$)	$n_{\rm H}$ (cm^{-3})	$n_{\rm He}$ (cm^{-3})	$n_{\rm d}$ (10^{-9} cm^{-3})	$T_{\rm g}$ (K)	$T_{\rm d}$ (K)	$M_{\rm star}$ (10^3 $M_\odot$)	$\tau_{\rm d,UV}$	$\tau_{\rm d,IR}$	ζ
Cloud 1	17	10^5	796	67	0	1074	10	2	0	0	0.13
Cloud 2	17	10^5	791	67	2.9	1082	10	2	22	0.15	0.54
Cloud 3	17	10^5	761	64	19	1134	10	2	146	1.0	4.5
Cloud X2	17	10^5	791	67	2.9	1082	10	20	22	0.15	5.0
Cloud X3	17	10^5	761	64	19	1134	10	20	146	1.0	43

To study radiation feedback in star-forming clouds, we model each cloud as a Bonnor–Ebert sphere of mass $10^5\ M_\odot$. The radius of a cloud is set to obey the Larson's law (Larson 1981). This gives the radius of a cloud to be 17 pc. As a radiation source, we place a simple stellar population (SSP) at the centre of the sphere. The SSP has the solar metallicity. We vary the mass of a radiation source for testing the role of source luminosity. We compute its luminosity and spectral-energy distribution as functions of time by using a population synthesis model, PÉGASE.2 (Fioc & Rocca-Volmerange 1997; 1999), assuming the Salpeter initial mass function (Salpeter 1955). We use linearly spaced 128 meshes in radial direction, 128 meshes in angular direction, and 256 meshes in frequency direction to solve radiation hydrodynamics. We use reflective boundary conditions at the inner boundary and semi-permeable boundary condition at the outer boundary.

Materials at radius, r, feel the radial gravitational acceleration,

$$a_{\rm g} = -G\frac{M(<r)}{r^2} - G\frac{M_{\rm star}}{\max\left(r^3, r_{\rm soft}^3\right)}r \tag{2.9}$$

where $M(<r)$ represents the total mass of gas inside r and $M_{\rm star}$ is the mass of the central radiation source. The gravitational force due to the radiation source is softened for numerical stability by introducing the softening length $r_{\rm soft}$, which is set to 0.5 pc.

To study the importance of dust in radiation feedback, we use five initial conditions, Clouds 1, 2, 3, X2, and X3 in which we vary the dust mass fraction and mass of the radiation source as follows. Cloud 1 is a dustless cloud, while Clouds 2 and X2 have the solar metallicity[2] and we assume that half of the metals are in dust. Although Clouds 2 and X2 have a typical metallicity of star-forming clouds, its IR optical depth from the cloud centre to the edge, $\tau_{\rm IR} = 0.15$ ($\sigma_{\rm IR} = 2.3 \times 10^{-12}$ cm^{-2}), is much lower than the value of typical star-forming clouds ($\tau_{\rm IR} \sim 1$; Agertz et al. 2013) because of the low central concentration of a Bonnor-Ebert sphere. We therefore apply a higher metallicity for Clouds 3 and X3 so that the IR optical depths of the clouds become unity. The initial mass of the radiation source is 2 % for Clouds 1, 2, and 3, while 20 % for Clouds X2, and X3. The details of initial conditions are listed in Table 2.1.

2.5 Results

We present density, ionization fraction, dust temperature, and velocity profiles of each cloud in Fig. 2.1. In order to investigate the relative importance of each process, we perform simulations in which several physical processes are switched off. Simulations that include effect of increased thermal pressure due to photoheating are indicated by a label 'PH'. When simulations do not have this label, hydrogen and helium are transparent for photons (photoionization and photoheating are switched off). Simulations in which we consider radiation pressure are labelled 'RP'; in the simulations labelled 'RP', radiation pressure on hydrogen, helium,

[2]We employ the solar metallicity by Asplund et al. (2009).

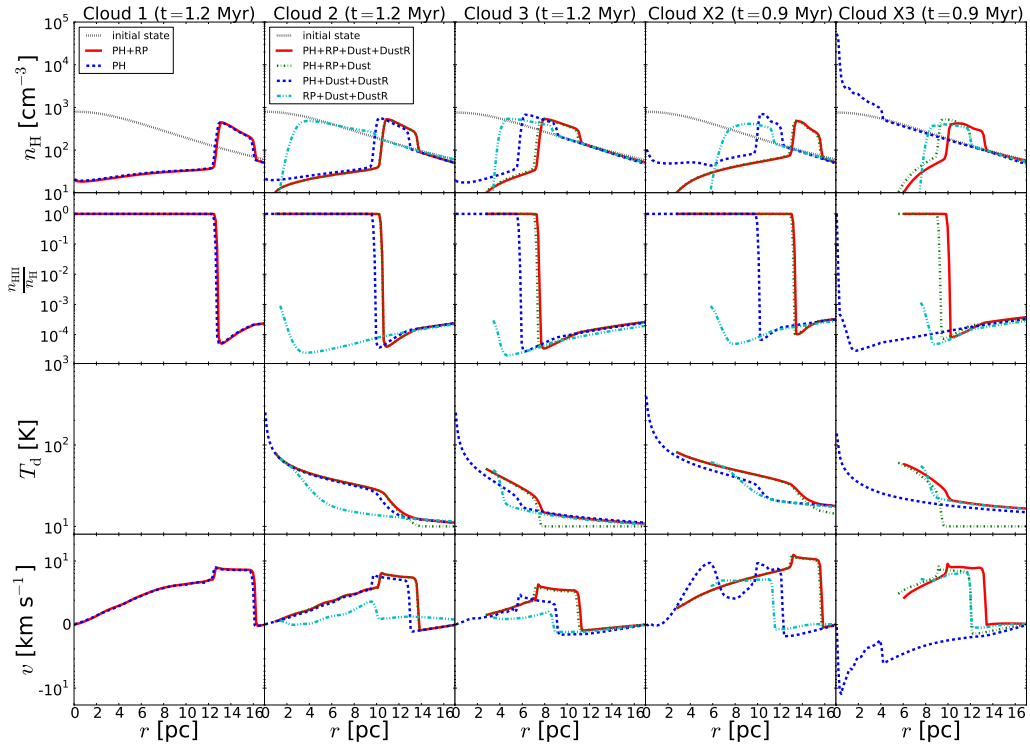

Figure 2.1: Density (top), ionization fraction (second from the top), dust temperature (second from the bottom), and velocity (bottom) profiles at $t = 0.2$ Myr. From left to right, we show the results for Clouds 1, 2, 3, X2, and X3. The black dotted lines in the top panels indicate the initial density profiles. The red solid lines represent the results of simulations that include all radiative transfer effects ('PH+RP' for Cloud 1 and 'PH+RP+Dust+DustR' for Clouds 2 ,3, X2 and X3). The blue dashed lines show the results of simulations in which we ignore radiation pressure ('PH' for Cloud 1 and 'PH+Dust+DustR' for Clouds 2, 3, X2, and X3). For Clouds 2, 3, X2, and X3, we perform simulations in which we include radiation pressure but we do not include absorption of re-emitted photons ('PH+RP+Dust'; green dot–dashed lines). Hydrogen and helium do not interact with photons in simulations labelled as 'RP+Dust+DustR', and hence photoheating is disabled in these simulations (cyan double dot–dashed lines).

and dust is all included. Clouds 2, 3, X2, and X3 have dust, and thus simulations for these clouds have a label, 'Dust'. In some simulations that include dust, we ignore absorption of re-emitted photons from dust. The label 'DustR' indicates that dust can absorb re-emitted photons and hence multiple events of absorption and re-emission are enabled. Simulations that include dust and all radiative processes are named 'PH+RP+Dust+DustR'.

By comparing simulations of Cloud 1, 'PH' and 'PH+RP', we confirm earlier results by Sales et al. (2014), that is, the effect of radiation pressure is negligible in dustless clouds. Radiation pressure is also negligible in Cloud 2 as expected from the value of $\zeta = 0.54$. The shell expansion in this cloud is almost identical to that in Cloud 1. In Cloud 3 where the dust-to-gas mass ratio is increased, the effect of radiation pressure becomes visible.

To isolate the effect of radiation pressure on dust, we run simulations in which we ignore the photoheating (and photoionization) of hydrogen and helium ('RP+Dust+DustR'). By comparing 'PH+Dust+DustR' and 'RP+Dust+DustR' in Cloud 3, we find that thermal pressure plays a more important role than radiation pressure in Cloud 3 in spite of the large value of ζ.

Adopting a higher star formation efficiency, i.e. higher source luminosity, also increases the relative importance of radiation pressure. In Clouds X2 and X3, radiation pressure is more important than in Clouds 2 and 3, respectively. In particular, thermal pressure is negligible in Cloud X3 compared with radiation pressure. Since we increase the mass of the radiation source, thermal pressure force alone cannot compete the gravitational force (see 'PH+Dust+DustR'); shell expansion is driven almost solely by radiation pressure in this case (see 'RP+Dust+DustR').

We then investigate the impact of absorption of re-emitted photons by dust by comparing 'PH+RP+Dust' and 'PH+RP+Dust+DustR'. We find that this effect is negligible in almost all clouds. Only in Cloud X3, radiation pressure is slightly enhanced by this process. Since Clouds 3 and X3 have the same IR optical depth, the importance of absorption of re-emitted IR photons should depend not only on the IR optical depth but also on the source luminosity.

For a given luminosity of a radiation source, a higher dust-to-gas mass ratio increases importance of radiation pressure. We, however, find that the net effect of radiation feedback (i.e. radiation pressure plus photo-heating) is decreased by the increased dust-to-gas mass ratio; the shell radii in Clouds 1, 2, and 3 become smaller in the increasing order of the dust-to-gas mass ratio. The shell radius in Cloud X3 is also smaller than that in Cloud X2. Since the shell expansion in Cloud X3 is dominated by radiation pressure, radiation feedback might become stronger than in Cloud X2 by increasing the dust-to-gas mass ratio further. Doing that would enhance the radiation pressure via multiple events of absorption of re-emitted photons. The adopted dust-to-gas mass ration for Cloud X3 is, however, already unrealistically high and, therefore, such a high dust-to-gas mass ratio would not be realised.

2.6 Discussion and Conclusions

We have investigated radiation feedback in dusty clouds of radius 17 pc by one-dimensional radiation hydrodynamic simulations. In order to treat recombination radiation and re-emission from dust, we utilize the impact parameter method for radiation transfer.

We find that radiation pressure is negligible in a dustless cloud as pointed out by Sales et al. (2014). Radiation pressure is almost negligible when we adopt the solar metallicity and a low star formation efficiency (2 %: Cloud 2). This result seems to support the idea proposed by Krumholz & Matzner (2009), that is, shell expansion is mainly driven by thermal pressure when the parameter, ζ, is smaller than unity. By increasing a dust-to-gas mass ratio, the importance of radiation pressure is increased. Although values of ζ in Cloud 3, and X2 are significantly larger than unity, thermal pressure is still more dominant than radiation pressure in driving shell expansion. In all cases, radiation feedback creates a high density, neutral, expanding shell, which may trigger succeeding star formation (Hosokawa & Inutsuka 2006).

We also find that effect of absorption of re-emitted photons is negligible in almost all clouds. Only in Cloud X3, radiation pressure is slightly enhanced by this process. We conclude that radiation pressure cannot be significantly boosted by this process on cloud scale unless either the star formation efficiency or the dust-to-gas mass ratio is extremely high.

In our simulations, radiation feedback becomes weaker for a given source luminosity as the dust-to-gas mass ratio increases by suppression of photoheating. This result is inconsistent with the assumption commonly made in cosmological simulations, that is, radiation feedback becomes stronger with the IR optical depth due to multiple events of absorption and re-emission of IR photons. (e.g. Hopkins et al. 2011; Aumer et al. 2013; Agertz et al. 2013; Okamoto et al. 2014). Our simulations are, however, on cloud scale and the IR optical depth is unity at maximum. Krumholz & Matzner (2009) estimate ζ in star burst galaxies and they find, in some cases, ζ exceeds 1000. For such a large value of ζ, radiation energy would be efficiently converted into radiation pressure, and radiation feedback might become stronger for a larger IR optical depth. To test this we have to perform radiation hydrodynamic simulations for star burst galaxies.

Our simulations likely overestimate the impact of radiation feedback by three reasons. First, we model a star-forming cloud as a Bonnor–Ebert sphere. In reality, however, star-forming clouds are highly turbulent and characterized by self-similar fractal structure (Falgarone et al. 1991; Elmegreen & Falgarone 1996; Stutzki et al. 1998). Photons preferentially escape through low density medium due to the anisotropy of the thermal radiation field when a cloud has such complex density structure, and thus dust obtains less momentum compared with that in a spherically symmetric cloud (Kuiper et al. 2010b; 2011; 2012; Kuiper & Yorke 2013). In order to properly deal with this situation, we should perform three-dimensional radiative hydrodynamics simulations that include re-emission from dust, which are currently computationally too expensive (but see Kuiper et al. 2010a). Secondly, we assume that gas and dust are tightly coupled. Although

this assumption is commonly made (e.g. Netzer & Elitzur 1993), dust would leave gas behind at the shock front because dust grains obtain large momentum from photons and create sharp shocks in our simulations. If this had happened, the net impact of radiation pressure on gas would become weaker than in our simulations. Finally, we do not include photon scattering by dust grains. In reality, grains are moderately reflective and strongly forward scattering in UV (see Draine 2003). The forward scattering of UV photons could strongly decrease the radiative pressure feedback. We defer these issues to future studies.

Chapter 3

The effect of radiation pressure on spatial distribution of dust inside H_{II} regions

3.1 Abstract

We investigate the impact of radiation pressure on spatial dust distribution inside H II regions using one-dimensional radiation hydrodynamic simulations, which include absorption and re-emission of photons by dust. In order to investigate grain size effects as well, we introduce two additional fluid components describing large and small dust grains in the simulations. Relative velocity between dust and gas strongly depends on the drag force. We include collisional drag force and coulomb drag force. We find that, in a compact H II region, a dust cavity region is formed by radiation pressure. Resulting dust cavity sizes (~ 0.2 pc) agree with observational estimates reasonably well. Since dust inside an H II region is strongly charged, relative velocity between dust and gas is mainly determined by the coulomb drag force. Strength of the coulomb drag force is about 2-order of magnitude larger than that of the collisional drag force. In addition, in a cloud of mass 10^5 $M_\odot$, we find that the radiation pressure changes the grain size distribution inside H II regions. Since large (0.1 μm) dust grains are accelerated more efficiently than small (0.01 μm) grains, the large to small grain mass ratio becomes smaller by an order of magnitude compared with the initial one. Resulting dust size distributions depend on the luminosity of the radiation source. The large and small grain segregation becomes weaker when we assume stronger radiation source, since dust grain charges become larger under stronger radiation and hence coulomb drag force becomes stronger.

3.2 Introduction

Radiation from young massive stars plays a crucial role in star forming regions, and its effect on spatial dust distribution inside H II regions is also non-negligible. O'dell & Hubbard (1965) firstly observed dust inside the H II region and many

other observations found dust in H II regions (O'dell et al. 1966; Ishida & Kawajiri 1968; Harper & Low 1971). O'dell & Hubbard (1965) observationally estimated the distribution of dust inside H II regions, concluding that gas-to-dust mass ratio decreases as a function of distance from the centre of the nebulae. Nakano et al. (1983) and Chini et al. (1987) observationally suggested the existence of dust cavity regions. There have been some theoretical attempts to reveal dust distribution inside H II regions (Mathews 1967; Gail & Sedlmayr 1979a;b). Gail & Sedlmayr (1979b) suggested that a dust cavity can be created by radiation pressure.

Radiation pressure may also produce spatial variations in the grain size distribution inside H II regions as suggested by recent observational data of IR bubbles. From the Galactic Legacy infrared Mid-Plane Survey Extraordinaire (GLIMPSE; Benjamin et al. 2003), Churchwell et al. (2006) found that about 25% of IR bubbles are associated with known H II regions and they claimed that the IR bubbles are primarily formed around hot young stars. Deharveng et al. (2010) then pointed out that 86% of IR bubbles are associated with ionized gas. Since Churchwell et al. (2006) missed the large ($>$ 10 arcmin) and small ($<$ 2 arcmin) bubbles, Simpson et al. (2012) presented a new catalogure of 5106 IR bubbles. Paladini et al. (2012) found that the peak of 250 μm continuum emission appears further from radiation source than that of 8 μm continuum emission. Since they assumed that 250 μm continuum emission traces the big grains (BGs) and 8 μm continuum emission traces the polycyclic aromatic hydrocarbons (PAHs), they argued that the dust size distribution depends on the distance from a radiation source.

Inoue (2002) argued the presence of the central dust depleted region — dust cavity — in compact/ultra-compact H II regions in the Galaxy by comparing the observed infrared-to-radio flux ratios with a simple spherical radiation transfer model. The dust cavity radius is estimated to be 30% of the Stromgren radius on average, which is too large to be explained by dust sublimation. The formation mechanism of the cavity is still an open question, while the radiation pressure and/or the stellar wind from the excitation stars have been suggested as responsible mechanisms. We will examine whether the radiation pressure can produce the cavity in this chapter. By considering the effect of radiation pressure on dust and assuming steady H II regions, Draine (2011b) theoretically explained the dust cavity size that Inoue (2002) estimated from observational data.

Akimkin et al. (2015; 2017) estimated dust size distribution by solving motion of dust and gas respectively, and they concluded that radiation pressure preferentially removes large dust from H II regions. Their simulations have, however, assumed a single OB star as a radiation source. As mentioned by Akimkin et al. (2015), grain electric potential is the main factor that affects the dust size distribution. If we assume a stronger radiation source, such as a star cluster, dust would been more strongly charged and their conclusions might change.

In this chapter, we investigate the effect of radiation pressure on spatial dust distribution inside compact H II regions and compare it with the observational estimates (Inoue 2002). In addition, we perform multi-dust-size simulations and study the effect of the luminosity of the radiation source on dust size distribution inside H II regions.

The structure of this chapter is as follows: In Section 3.3, we describe our

simulations. In Section 3.4, we describe our simulation setup. In Section 3.5, we present simulation results. In Section 3.6, we discuss the results and present our conclusions.

3.3 Methods

We place a radiation source at the centre of a spherically symmetric gas distribution. The species we include in our simulations are H I, H II, He I, He II, He III, electrons, and dust. We assume the dust-to-gas mass ratio to be 6.7×10^{-3} corresponding to a half of the abundance of elements heavier than He (so-called 'metal') in the Sun (Asplund et al. 2009). We neglect gas-phase metal elements in this chapter. We solve the radiation hydrodynamic equations at each timestep as follows:

step 1 Hydrodynamic equations

step 2 Radiative transfer and other related processes

substep 2.1 Static radiative transfer equations

substep 2.2 Chemical reactions

substep 2.3 Radiative heating and cooling

substep 2.4 Grain electric potential

The methods we use for radiation transfer, chemical reactions, radiative heating, cooling and time stepping are the same as Ishiki & Okamoto (2017) or Chapter 2.

3.3.1 Dust model

We include absorption and thermal emission of photons by dust grains in our simulations. To convert the dust mass density to the grain number density, we assume a graphite grain whose material density is $2.26\,\mathrm{g\,cm^{-3}}$ (Draine & Salpeter 1979). We employ the cross-sections of dust in Draine & Lee (1984) and Laor & Draine (1993)[1]. Dust sizes we assume are 0.1 μm or 0.01 μm. Dust temperature is determined by the radiative equilibrium, and thus the dust temperature is independent from gas temperature. We assume that the dust sublimation temperature is 1500 K; however, dust never be heated to this temperature in our simulations. We do not include photon scattering by dust grains for simplicity.

3.3.2 Grain electric potential

In our simulations, we solve hydrodynamics including the coulomb drag force which depends on grain electric potential. In order to determine the grain electric potential, we consider following processes: primary photoelectric emission, auger electron emission, secondary electron emission, and electron and ion collisions (Weingartner & Draine 2001a; Weingartner et al. 2006). The effect of auger

[1] http://www.astro.princeton.edu/~draine/dust/dust.diel.html

electron emission and secondary electron emission is, however, almost negligible in our simulations, because high energy photons ($> 10^2$ eV) responsible for the two processes are negligible in the radiation sources considered in this chapter. Since the time scale of dust charging processes is so small ($\lesssim$1 yr), we integrate the equation of grain electric potential implicitly.

3.3.3 Dust drag force

In our simulations, we calculate the effect of drag force $F_{\rm drag}$ on a dust of charge $Z_{\rm d}$ and radius $a_{\rm d}$ (Draine & Salpeter 1979) as follows:

$$F_{\rm drag} = 2\pi a_{\rm d}^2 kT_{\rm g}\left[\sum_{\rm i} n_{\rm i}\left(G_0(s_{\rm i}) + z_{\rm i}^2\phi^2 \ln(\Lambda/z_{\rm i}) G_2(s_{\rm i})\right)\right],$$

where

$$\begin{aligned} s_{\rm i} &\equiv \sqrt{m_{\rm i}v^2/(2kT_{\rm g})}, \\ G_0(s_{\rm i}) &\approx 8s_{\rm i}/(3\sqrt{\pi})\sqrt{1+9\pi s_{\rm i}^2/64}, \\ G_2(s_{\rm i}) &\approx s_{\rm i}/(3\sqrt{\pi}/4 + s_{\rm i}^3), \\ \phi &\equiv Z_{\rm d}e^2/(a_{\rm d}kT_{\rm g}), \\ \Lambda &\equiv 3/(2a_{\rm d}e|\phi|)\sqrt{kT_{\rm g}/\pi n_{\rm e}}, \end{aligned}$$

k is the Boltzmann constant, $T_{\rm g}$ is the temperature of gas, $n_{\rm i}$ is the number density of ith gas species, $n_{\rm e}$ is the number density of electron, $z_{\rm i}$ is the charge of ith gas species (i = H I, H II, He I, He II, He III), and $m_{\rm i}$ is the mass of ith species.

3.3.4 Hydrodynamics

dust and gas dynamics

In this section we describe the procedure to solve the set of hydrodynamic equations:

$$\begin{aligned} \frac{\partial}{\partial t}\rho_{\rm g} + \frac{\partial}{\partial x}\rho_{\rm g}v_{\rm g} &= 0 \\ \frac{\partial}{\partial t}\rho_{\rm d} + \frac{\partial}{\partial x}\rho_{\rm d}v_{\rm d} &= 0 \\ \frac{\partial}{\partial t}\rho_{\rm g}v_{\rm g} + \frac{\partial}{\partial x}\rho_{\rm g}v_{\rm g}^2 &= \rho_{\rm g}a_{\rm gra} + f_{\rm rad,g} - \frac{\partial}{\partial x}P_{\rm g} \\ &\quad + K_{\rm d}(v_{\rm d} - v_{\rm g}) \\ \frac{\partial}{\partial t}\rho_{\rm d}v_{\rm d} + \frac{\partial}{\partial x}\rho_{\rm d}v_{\rm d}^2 &= \rho_{\rm d}a_{\rm gra} + f_{\rm rad,d} \\ &\quad + K_{\rm d}(v_{\rm g} - v_{\rm d}) \\ \frac{\partial}{\partial t}\left(\frac{1}{2}\rho_{\rm g}v_{\rm g}^2 + \frac{1}{2}\rho_{\rm d}v_{\rm d}^2 + e_{\rm g}\right) + \frac{\partial}{\partial x}\left[\left(\frac{1}{2}\rho_{\rm g}v_{\rm g}^2 + h_{\rm g}\right)v_{\rm g} + \frac{1}{2}\rho_{\rm d}v_{\rm d}^3\right] &= \left(\rho_{\rm g}v_{\rm g} + \rho_{\rm d}v_{\rm d}\right)a_{\rm gra} \\ &\quad + f_{\rm rad,g}v_{\rm g} + f_{\rm rad,d}v_{\rm d} \end{aligned}$$

where $\rho_{\rm g}$ is the mass density of gas, $\rho_{\rm d}$ is the mass density of dust, $v_{\rm g}$ is the velocity of gas, $v_{\rm d}$ is the velocity of dust, $a_{\rm gra}$ is the gravitational acceleration, $f_{\rm rad,g}$ is the radiation pressure gradient force on gas, $f_{\rm rad,d}$ is the radiation pressure gradient force on dust, $P_{\rm g}$ is the gas pressure, $e_{\rm g}$ is the internal energy of gas, $h_{\rm g}$ is the enthalpy of gas, and $K_{\rm d}$ is the drag coefficient between gas and dust defined as follows:

$$K_{\rm d} \equiv \frac{n_{\rm d} F_{\rm drag}}{|\boldsymbol{v}_{\rm d} - \boldsymbol{v}_{\rm g}|},$$

where $n_{\rm d}$ is the number density of dust grains.

In order to solve the dust drag force stably, we use following algorithm for the momentum equations:

$$\begin{bmatrix} p_{\rm d}^{*} \left(= \rho_{\rm d}^{\rm t+\Delta t} v_{\rm d}^{*}\right) \\ p_{g}^{*} \left(= \rho_{\rm g}^{\rm t+\Delta t} v_{\rm g}^{*}\right) \end{bmatrix} = \begin{bmatrix} p_{\rm d}^{t} \\ p_{g}^{t} \end{bmatrix} + \begin{bmatrix} F_{\rm p,d}(\rho_{\rm d}^{t}, v_{\rm d}^{t}) \\ F_{\rm p,g}(\rho_{g}^{t}, v_{\rm g}^{t}, e_{g}^{t}) \end{bmatrix} \Delta t, \tag{3.1}$$

$$\begin{aligned} \begin{bmatrix} p_{\rm d}^{\rm t+\Delta t} \\ p_{\rm g}^{\rm t+\Delta t} \end{bmatrix} &= \begin{bmatrix} \rho_{\rm d}^{\rm t+\Delta t} \\ \rho_{\rm g}^{\rm t+\Delta t} \end{bmatrix} \frac{p_{\rm d}^{*} + p_{\rm g}^{*}}{\rho_{\rm d}^{\rm t+\Delta t} + \rho_{g}^{\rm t+\Delta t}} \\ &+ \begin{bmatrix} \rho_{\rm d}^{\rm t+\Delta t} \\ \rho_{\rm g}^{\rm t+\Delta t} \end{bmatrix} \left[a_{\rm gra} + \frac{f_{\rm d} + f_{g}}{\rho_{\rm d}^{\rm t+\Delta t} + \rho_{g}^{\rm t+\Delta t}} \right] \Delta t \\ &+ \begin{bmatrix} -1 \\ 1 \end{bmatrix} \frac{\rho_{g}^{\rm t+\Delta t} \rho_{d}^{\rm t+\Delta t}}{\rho_{g}^{\rm t+\Delta t} + \rho_{d}^{\rm t+\Delta t}} \left(v_{\rm g}^{*} - v_{\rm d}^{*}\right) {\rm e}^{-\frac{\Delta t}{t_d}} \\ &+ \begin{bmatrix} -1 \\ 1 \end{bmatrix} t_d \frac{\rho_{d}^{\rm t+\Delta t} f_{g} - \rho_{g}^{\rm t+\Delta t} f_{d}}{\rho_{g} + \rho_{d}} (1 - {\rm e}^{-\frac{\Delta t}{t_d}}), \end{aligned} \tag{3.2}$$

where Δt is the time step, $\rho_{\rm i}^{\rm t}$ is the mass density of ith species at time t, $p_{\rm i}^{\rm t}$ is the momentum of ith species at time t, $e_{\rm g}^{\rm t}$ is the internal energy of gas at time t, $F_{\rm X,i}$ is the advection of the physical quantity X of the ith species, $f_{\rm d}$ is the force on dust ($f_{\rm d} = f_{\rm rad,d}$), $f_{\rm g}$ is the force on gas ($f_{\rm g} = f_{\rm rad,g} - \partial P_{\rm g}/\partial x$), and the inverse of the drag stopping time, $t_{\rm d}$, is

$$t_{\rm d}^{-1} = K_{\rm d} \frac{\rho_{\rm d}^{\rm t+\Delta t} + \rho_{\rm g}^{\rm t+\Delta t}}{\rho_{\rm d}^{\rm t+\Delta t} \rho_{\rm g}^{\rm t+\Delta t}}. \tag{3.3}$$

Equation (3.2) that determines the relative velocity between dust and gas is the exact solution of the following equations:

$$\begin{aligned} \rho_{\rm g} \frac{d}{dt} v_{\rm g} &= f_{\rm rad,g} - \frac{\partial}{\partial x} P_{\rm g} + \rho_{\rm g} a_{\rm gra} + K_{\rm d}(v_{\rm d} - v_{\rm g}), \\ \rho_{\rm d} \frac{d}{dt} v_{\rm d} &= f_{\rm rad,d} + \rho_{\rm d} a_{\rm gra} + K_{\rm d}(v_{\rm g} - v_{\rm d}). \end{aligned} \tag{3.4}$$

Momentum advection and other hydrodynamic equations are solved by using AUSM+ (Liou 1996). We solve the hydrodynamics in the second order accuracy in space and time. In order to prevent cell density from becoming zero or a negative value, we set the minimum number density, $n_{\rm H} \simeq 10^{-13}$ cm^{-3}. We have confirmed

that our results are not sensitive to the choice of the threshold density as long as the threshold density is sufficiently low.

In order to investigate whether our method is reliable, we perform shock tube tests in Appendix A. ln Appendix B, we describe how we deal with the dust grains with two sizes.

3.4 Simulation setup

Table 3.1: Initial conditions and numerical setup for the simulations. The radius of each cloud are shown as $r_{\rm cloud}$. The number densities, $n_{\rm H}$, $n_{\rm He}$, and $n_{\rm d}$ indicate the initial number densities of hydrogen, helium, and dust in the innermost cell, respectively. Spatial distribution of dust and gas are indicated by 'C' (constant density) and 'BE' (Bonnor-Ebert sphere) in the 7th column. The spectrum of a radiation source is shown in the 8th column, where 'SSP' and 'BB' respectively indicate a simple stellar population with solar metallicity and the black body spectrum of given temperature. $\dot{N}_{\rm ion}$ represents the number of ionized photon emitted from a radiation source per unit time. The initial temperature of gas and dust are represented by $T_{\rm g}$ and $T_{\rm d}$, respectively. The mass of a central radiation source is indicated by $M_{\rm star}$. The number of dust sizes is shown in the 13th column. When 'Gravity' is on/off, we include/ignore gravitation force in the simulations.

Cloud	$r_{\rm cloud}$ (pc)	$n_{\rm H}$ ($\rm cm^{-3}$)	$n_{\rm He}$ ($\rm cm^{-3}$)	$n_{\rm d,Large}$ (10^{-10} $\rm cm^{-3}$)	$n_{\rm d,Small}$ (10^{-7} $\rm cm^{-3}$)	Distribution	Source	$\dot{N}_{\rm ion}$ (10^{49} $\rm s^{-1}$)	$T_{\rm g}$ (K)	$T_{\rm d}$ (K)	$M_{\rm star}$ (10^3 $M_\odot$)	Dust	Gravity
Cloud 1	1.2	4×10^5	3.4×10^4	6.4×10^3	0	C	BB (50100K)	6.2	100	10	0.08	1	off
Cloud 2	17	791	67	9.6	3.0	BE	BB (38500K)	0.72	1082	10	0.05	2	on
Cloud 3	17	791	67	9.6	3.0	BE	SSP	5.8	1082	10	2	2	on
Cloud 4	17	791	67	9.6	3.0	BE	SSP	58	1082	10	20	2	on

In the first simulation, in order to investigate whether our simulation derives a consistent result with the observational estimate for compact/ultra-compact H II regions (Inoue 2002), we model a constant density cloud of hydrogen number density 4×10^5 cm^{-3} and radius 1.2 pc. As a radiation source, we place a single star (i.e. black body) at the centre of the sphere. Since we are interested in the formation of a dust cavity, we neglect the gravity which does not affect the relative velocity between dust grains and gas (see equation (3.2)). We assume a single dust grain size in this simulation.

In the second set of simulations, in order to investigate the effect of radiation pressure on the dust grain size distribution inside a large gas cloud, we model a cloud as a Bonner-Ebert sphere of mass 10^5 $M_\odot$ and radius 17 pc. As the radiation source, we consider a single star (black body, BB) or a star cluster (a simple stellar population, SSP) and we change the luminosity of the radiation source to investigate the dependence of the dust size distribution on the luminosity of the radiation source. We compute its luminosity and spectral-energy distribution as a function of time by using a population synthesis code, PÉGASE.2 (Fioc & Rocca-Volmerange 1997; 1999), assuming the Salpeter initial mass function (Salpeter 1955) and the solar metallicity. We set the mass range of the initial mass function to be 0.1 to 120 $M_\odot$.

Materials at radius, r, feel the radial gravitational acceleration,

$$a_{\rm gra}(r) = -G\frac{M_{\rm star}r}{(r^2+r_{\rm soft}^2)^{3/2}} - G\frac{M(<r)}{r^2}$$

where $M(<r)$ represents the total mass of gas inside r and $M_{\rm star}$ is the mass of the central radiation source, which is 50 $M_\odot$ for the single star case and 2×10^3 or 2×10^4 $M_\odot$ for the two star cluster cases. Since the gravity from the radiation source has a non-negligible effect on simulation results and causes numerical instability in the case of SSP, we need to introduce softening length, $r_{\rm soft}$. We set it to 0.5 pc for the SSP. Since the gravity from a single star is negligible effect on simulation results, we set 0 pc for the single star.

Following the dust size distribution of Mathis et al. (1977), so-called MRN distribution, we assume two dust size in these simulations. We assume the initial number ratio of large to small dust as

$$n_{\rm d,Large} : n_{\rm d,Small} = 1 : 10^{2.5},$$

where $n_{\rm d,Large}$ and $n_{\rm d,Small}$ are the number density of dust grains of 0.1 μm and 0.01 μm in size, respectively.

The details of initial conditions are listed in Table 3.1. We use linearly spaced 128 meshes in radial direction, 128 meshes in angular direction, and 256 meshes in frequency direction in all simulations to solve radiation hydrodynamics.

3.5 Results

3.5.1 Dust cavity radius

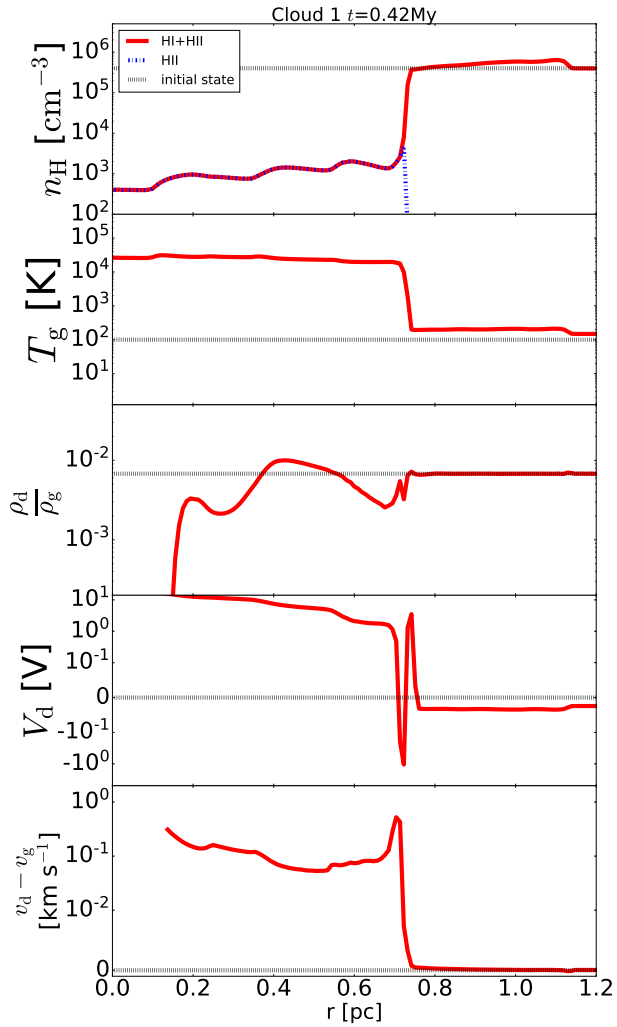

Figure 3.1: Density (top-row), gas temperature (second-row), dust-to-gas mass ratio (third-row), grain electric potential (fourth-row), and relative velocity between dust and gas (bottom-row) profile at $t = 0.42$ Myr. The black dotted lines show the initial profiles. The red solid lines represent the simulation results. The blue dashed lines in the top panel shows the ionized hydrogen density profile.

Table 3.2: Comparison between the simulation results ($t = 0.42$ Myr) and the observational estimates. The number densities of ionized electrons inside H II regions are represented by $\overline{n}_{\rm e}$. The number of ionized photons emitted from radiation sources per unit time is represented by $\dot{N}_{\rm ion}$. The radius of H II region is represented by $r_{\rm H\,II}$. The radius of dust cavity radius is represented by $r_{\rm d}$. The parameter $y_{\rm d}$ is defined by $y_{\rm d} \equiv r_{\rm d}/R_{\rm St}$, where $R_{\rm St}$ is the Strömgren radius. Since, observationally, the number density is driven from the column density, the electron number density in the simulation is defined as by $\overline{n}_{\rm e} \equiv \int_0^{r_{\rm H\,II}} n_{\rm e} dx / r_{\rm H\,II}$. In addition, in order to match the definition of $r_{\rm d}$ with Inoue (2002), the dust cavity radius is defined by $r_{\rm d} \equiv r_{\rm H\,II} \left(1 - \int_0^{r_{\rm H\,II}} \rho_{\rm d} dx / \int_0^{r_{\rm H\,II}} \rho_{\rm g} (\rho_{\rm d}/\rho_{\rm g})_{\rm initial} dx\right)$, where $(\rho_{\rm d}/\rho_{\rm g})_{\rm initial}$ represents the initial dust-to-gas mass ratio.

	$\overline{n}_{\rm e}$ ($\rm cm^{-3}$)	$\dot{N}_{\rm ion}$ ($10^{49}\rm s^{-1}$)	$r_{\rm H\,II}$ (pc)	$r_{\rm d}$ (pc)	$y_{\rm d} \equiv r_{\rm d}/R_{\rm St}$
this work ($t = 0.42$ Myr)	1247	6.2	0.73	0.21	0.20
Inoue (2002)	1200 ± 400	6.8 ± 3.9	0.72 ± 0.098	0.28 ± 0.13	0.30 ± 0.12

We present density, gas temperature, dust-to-gas mass ratio, grain electric potential ($V_{\rm d} \equiv eZ_d/a_{\rm d}$), and relative velocity between dust and gas as functions of radius in Fig. 3.1. In the top panels, the hydrogen number density is indicated by the red solid line. The number density of H II is indicated by the blue dash-dotted line. The initial state of the simulation is shown by the black dotted line.

The average electron number density within an H II region, $\overline{n}_{\rm e}$, the H II region radius, $r_{\rm H\,II}$, the dust cavity radius, $r_{\rm d}$, and the ratio between the radius of the dust cavity to the Strömgren radius, $y_{\rm d}$, obtained by our simulation ($t = 0.42$ Myr) and the observational estimate are shown in Table 3.2. We find that our simulation results are in broad agreement with the observational estimate. The dust cavities, hence, could be created by radiation pressure. The parameter $y_{\rm d}$ obtained by the simulation is somewhat smaller than the observational estimate. However, we could find a better agreement if we tuned the initial condition such as the gas density. In addition, the agreement would be better if we included the effect of stellar winds, which was neglected in this chapter.

Since dust inside the H II region is strongly charged, relative velocity between dust and gas is determined by coulomb drag force. Magnitude of the coulomb drag force is about 2-order of magnitude larger than that of the collisional drag force. The relative velocity, thus, becomes largest when the dust charge is neutral.

Grain electric potential gradually decreases with radius and then suddenly drops to negative value. Near the ionization front, the number of ionized photons decreases and hence collisional charging becomes important. This is the reason behind the sudden decrease of the grain electric potential. In the neutral region, there is no photon which is able to ionize the gas and hence there is few electrons that collide with dust grains. On the other hand, there are photons that photoelectrically charge dust grains. Therefore, the grain electric potential becomes positive again at just outside of the H II region. Then, the UV photons are consumed and the electron collisional charging becomes dominant again in the neutral region.

3.5.2 Spatial distribution of large dust grains and small dust grains

We present densities, gas temperature, dust-to-gas mass ratios for large and small grains, large-dust-to-small-dust mass ratios ($\rho_{\rm d,Large}/\rho_{\rm d,Small}$), the grain electric potential, and relative velocity between dust and gas as functions of radius in Fig. 3.2. In order to compare the simulation results on the dust size distribution with each other, we present the results at the time when the shock front reaches to $\sim$15 pc. In order to study the dependence of the dust size distribution on time and the luminosity of the radiation source, we also present the simulation result of Cloud 2 at t =1.1 My: the same irradiation time as Cloud 4. In the top panels, the hydrogen number density is indicated by the red solid lines and that of H II is indicated by the blue dot-dashed lines. Initial states of the simulations are shown by black dotted lines. In the sixth-row, the charges of dust grains with size 0.1 μm and 0.01 μm are indicated by the red solid and blue dot-dashed lines, respectively. The black dotted lines show the initial profiles (i.e. 0 V). In the

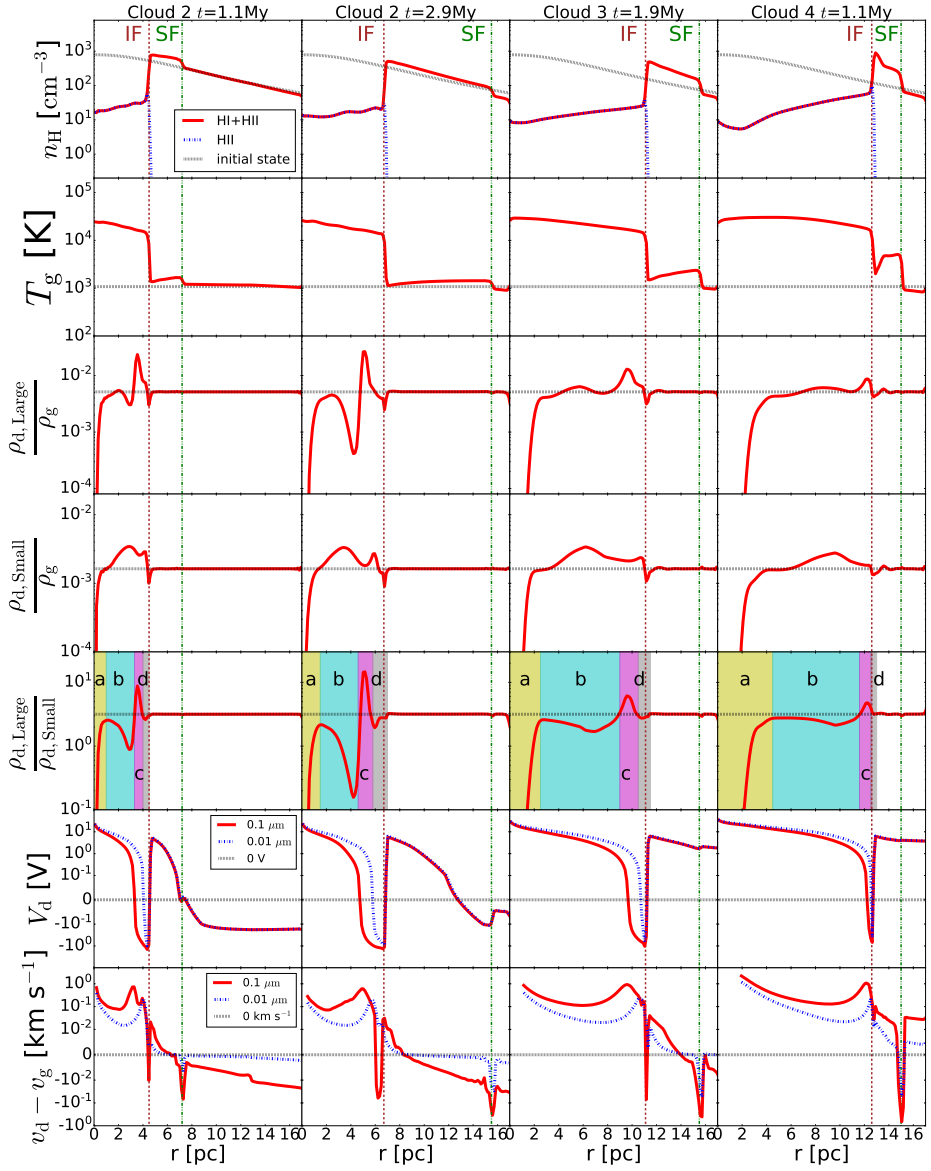

Figure 3.2: Density (top-row), gas temperature (second-row), large-dust-to-gas-mass ratio (third-row), small-dust-to-gas-mass ratio (fourth-row), large-dust-to-small-dust-mass ratio (fifth-row), grain electric potential (sixth-row), and relative velocity between dust and gas (bottom-row) profiles. From left to right, we show the results for Clouds 2 at t = 1.1 Myr, Cloud 2 at t = 2.9 Myr, Cloud 3 at t = 1.9 Myr, and Cloud 4 at t = 1.1 Myr. The black dotted lines show the initial profiles. The red solid lines represent the results of simulations. The blue dashed lines at the top panels show the ionized hydrogen density profiles. In the sixth-row, the red solid and blue dashed lines show the charge of the large dust and the small dust, respectively. In the bottom panels, the red solid and blue dashed lines show the relative velocity between the large dust and gas and between the small dust and gas, respectively. Ionization front (IF) is indicated by vertical brown dashed lines and the shock front (SF) is indicated by vertical green dot-dot-dashed lines.

bottom panels, the relative velocity between dust grains with size 0.1 μm and gas and between dust grains with size 0.01 μm and gas are indicated by the red solid and blue dot-dashed lines, respectively. Note that the radiation source becomes stronger from Cloud 2 to Cloud 4.

We find that radiation pressure affects the dust distribution within an H II region depending on the grain size. In Fig. 3.2, we divide them into the following four regions:

(a) From the central part, radiation pressure removes both large and small dust grains and creates a dust cavity (the yellow shaded region).

(b) Within an H II region, $\rho_{\rm d,Large}/\rho_{\rm d,Small}$ has a peak. Between the region 'a' and this peak, there is a region where $\rho_{\rm d,Large}/\rho_{\rm d,Small}$ takes the local minimum value (the cyan shaded region), for example, at $r \sim 4$ pc in Cloud 2 at $t = 2.9$ Myr.

(c) The region that contains the peak mentioned above is shaded by magenta.

(d) The $\rho_{\rm d,Large}/\rho_{\rm d,Small}$ is also reduced just behind the ionization front (the gray shaded region), for example, at $r \sim 6$ pc in Cloud 2 at $t = 2.9$ Myr.

We find that the dust cavity radius becomes larger as the radiation source becomes brighter (the regions 'a'). The reasons are as follows. Grain electric potential of the dust grains with the same size within $r = 2$ pc is almost the same among all simulations and the number density of the gas becomes smaller for stronger radiation source. Since the dust drag force strongly depends on the grain electric potential, the number density of gas, and radiation pressure on dust, relative velocity between dust and gas becomes larger for the brighter source.

In the region 'b' and 'd', the ratio $\rho_{\rm d,Large}/\rho_{\rm d,Small}$ is decreased from the initial condition when the radiation source is a single OB star (Cloud 2). Except in the ionization front (vertical brown dashed lines) which is contained in the region 'd', radiation pressure preferentially removes large dust grains from these regions. The photoelectric yield of the large dust grains is smaller than that of the small dust grains, and hence grain electric potential of the large dust grains becomes smaller than that of the small dust grains. Coulomb drag between large dust grains and gas therefore becomes weaker than that between small dust grains and gas. On the other hand, since Cloud 4 has the strongest radiation source and hence it makes grain electric potentials largest among the simulations, the dust size segregation in the regions 'b' and 'd' is less prominent. Even when we compare Cloud 2 and 4 at the same irradiation time, t =1.1 Myr, the dust size distributions inside H II regions are different. Luminosity of the radiation source must be the main cause of the dust size segregation.

The ratio $\rho_{\rm d,Large}/\rho_{\rm d,Small}$ in all simulations has a peak in the regions 'c'. Since dust grains have large negative charge in the regions 'c' and 'd', the coulomb drag force between dust and gas is strong and hence dust and gas are tightly coupled each other. Large dust grains are, therefore, removed from the regions 'a' and 'b' and gathered in the regions 'c'.

At the ionization front and the shock front (vertical green dot-dot-dashed lines), the relative velocity, $v_{\rm d} - v_{\rm g}$ has downward peaks. In theses fronts, gas pressure force exceeds radiation pressure force. Since the dust drag time depends on the dust grain size, the dust-gas relative velocity also depends on the grain size. As a result, $\rho_{\rm d,Large}/\rho_{\rm d,Small}$ is slightly reduced in these fronts.

3.6 Discussion and Conclusions

We have investigated radiation feedback in dusty clouds by one-dimensional multi-fluid hydrodynamic simulations. In order to study spatial dust distribution inside H II regions, we solve gas and dust motion self-consistently. We also investigate dust size distribution within H II regions by considering dust grains with two different sizes.

We find that radiation pressure creates dust cavity regions. We confirm that the size of the dust cavity region is broadly agree with the observational estimate (Inoue 2002).

We also find that radiation pressure preferentially removes large dust from H II regions in the case of a single OB star. This result is almost the same as in Akimkin et al. (2015). The dust size distribution is, however, less affected when the radiation source is a star cluster, in other word, a more luminous case. Resulting dust size distributions largely depend on the luminosity of the radiation source.

We assume dust is graphite. There are, however, other forms of dust such as silicate. Since the photoelectric yield and the absorption coefficient depend on a dust model, spatial dust distribution of dust grains may become different when we use a different dust model. For example, since silicate has a larger work function and a smaller absorption coefficient than graphite, the cavity size in the silicate case may become larger than that in the graphite case (see Akimkin et al. 2015; 2017 for details).

In our simulations, we neglect the effect of sputtering that changes the dust grain size. We estimate this according to Nozawa et al. (2006), and confirm that sputtering effect is negligible in our simulations. However, if we consider the smaller dust grains, we may have to include the sputtering.

Chapter 4

Growth of massive black holes in dusty clouds: impacts of relative velocity between dust and gas

4.1 Abstract

We investigate the impacts of the relative motions between dust and gas on the accretion rate onto Intermediate Mass Black Holes (IMBHs) by using one-dimensional radiation hydrodynamic simulations. To investigate the effect of grain size on the gas accretion, we introduce two additional fluid components to gas, which describe large (0.1 μm) and small (0.01 μm) dust grains in the simulations. We find that the accretion rate is reduced due to the radiation force compared with dust free case. We also find that the dust-to-gas mass ratio significantly changes within H II regions because of the relative motions of dust and gas. The decoupling of dust from gas alleviates the suppression of black hole growth compared with the complete coupling case. This effect may allow moderate growth of black holes even in dusty clouds. In addition, relative motion between dust and gas affects the spectral energy distribution (SED) owing to dust re-emission at wavelength $\lambda \sim 10$ μm.

4.2 Introduction

Revealing the formation process of supermassive black holes (SMBHs) is one of the big challenges in modern astrophysics. Recent observation indicated that SMBHs are already formed even at redshift $z \gtrsim 6$ (Mortlock et al. 2011; Wu et al. 2015). However, the formation process of those SMBHs at high redshift is not well understood.

It is widely believed that SMBHs at high redshifts were formed by the following steps: (1) Formation of the "seed" black holes (BHs); (2) Formation of the

SMBHs by gas accretion onto seed BHs. The formation process of seed BHs is not well understood yet and various formation scenarios of seed BHs have been suggested; stellar-mass BHs of Population III star remnants (Yoshida et al. 2008; Alvarez et al. 2009; Susa et al. 2014), direct collapse of supermassive stars (Omukai 2001; Bromm & Loeb 2006; Begelman et al. 2006; Hosokawa et al. 2012; 2013; Inayoshi et al. 2014; Sugimura et al. 2014), and formation by core collapse of dense star clusters (Portegies Zwart & McMillan 2002; Omukai et al. 2008; Devecchi & Volonteri 2009; Katz et al. 2015; Yajima & Khochfar 2016). If gas accretes onto BHs at Eddington accretion rate (assuming 10 % radiative efficiency), it takes about 5×10^2 Myr to be SMBHs of mass $10^9\ M_\odot$ from seed BHs of mass $10^5\ M_\odot$. Since $z \sim 6$ is about $t \sim 9 \times 10^8$ yr for the ΛCDM model, SMBHs can grow by the observed redshifts if the gas accretes onto BHs at the Eddington accretion rate. Radiation hydrodynamic simulations, however, indicate that radiation from accretion disks suppresses the growth of BHs as discussed in the next paragraph.

Milosavljević et al. (2009) and Park & Ricotti (2011; 2012) performed radiation hydrodynamic simulations of the gas accretion process, resolving Bondi radius. They showed that radiation from accretion disks suppresses the gas accretion rate lower than Eddington ratio by both radiation pressure and photoinoization (however, for sufficiently dense environments, see Inayoshi et al. 2016). They assumed primordial gas in their simulations.

Recent observations and numerical simulations suggested that not only metal but dust exists in early universe and indicate that assuming primordial gas is not appropriate for some cases. Inoue et al. (2016) detected the metal at redshift $z \gtrsim 7$. Dust grains were also detected by dust re-emission or dust extinction in galaxies at $z \gtrsim 7$ (e.g. z=7.5, Watson et al. 2015; z=7.2, Hashimoto et al. 2019; z=8.3, Tamura et al. 2019) or in quasars at $z \gtrsim 6$ (e.g. z=6.4, Bertoldi et al. 2003; z=6.2 Maiolino et al. 2004; z=7.1, Venemans et al. 2012; z=7.5, Venemans et al. 2017) Numerical simulation indicated that the dust-to-gas mass ratio of massive galaxies in an overdense region could reach to the solar neighborhood value at $z \gtrsim 6$ (Yajima et al. 2015). BH, therefore, may grow in dust rich environments even at high redshift.

Since the cross section of dust grains is much larger than Thomson cross section, existence of dust suppresses the gas accretion onto BHs. Yajima et al. (2017) studied the dusty gas accretion onto BHs by performing 1D radiation hydrodynamic simulations. They concluded that the radiation pressure on dust suppresses the gas accretion onto BHs, and accretion rate of dusty gas onto BHs becomes smaller than that of primordial gas. (however, for sufficiently dense environments, see Toyouchi et al. 2019). Yajima et al. (2017), however, did not consider the relative motion between dust and gas.

This relative motion was considered for the star formation regions (Draine 2011b; Akimkin et al. 2015; 2017; Ishiki et al. 2018), interstellar medium (Inoue & Inutsuka 2008), and galaxy formation (Bekki 2015; Fukushima et al. 2018; Hirashita & Inoue 2019). Especially, Akimkin et al. (2015; 2017) and Ishiki et al. (2018) estimated spatial distribution of dust by solving motion of dust and gas respectively, and they concluded that radiation pressure preferentially removes

dust from H II regions.

By considering the relative motion between dust grains and gas, radiation pressure may remove the dust grains which suppress the gas accretion onto BHs. In this chapter, we investigate this effect.

The structure of this chapter is as follows: In Section 4.3, we describe our simulations. In Section 4.4, we explain our simulation setup. In Section 4.5, we present simulation results. In Section 4.6, we discuss the results. In Section 4.7, we present our conclusions.

4.3 Methods

We place a BH at the centre of a spherically symmetric gas distribution. The chemical species we include in our simulations are H I, H II, He I, He II, He III, electrons, and dust. In order to determine the mass ratio of H, He, we assume the Solar chemical abundance (Asplund et al. 2009). We assume the dust-to-gas mass ratio to be $M_{\rm dust}/M_{\rm gas} = 6.0\times10^{-3}(Z/Z_{\odot})$ corresponding to the dust-to-gas mass ratio in the solar neighborhood (Spitzer 1978). We neglect gas-phase metal elements in this chapter.

We solve the radiation hydrodynamic equations at each timestep as follows:

step 1 Hydrodynamic equations

step 2 Radiative transfer and other related processes

substep 2.1 Radiative transfer equations

substep 2.2 Chemical reactions

substep 2.3 Radiative heating and cooling

substep 2.4 Grain electric potential

In addition, using simulation results, we estimate the spectral energy distribution by dust re-emission.

The methods we use for radiation transfer, chemical reactions, radiative heating, cooling, time stepping, dust model (we assume dust grains are graphite), grain electric potential, and dust drag force are the same as our previous work (Ishiki et al. 2018; hereafter paper I) or chapter 3 except some details. We list the major difference in methods and parameters between this work and paper I in Table 4.1. In the following sub-sections, we describe the changes we made for this chapter.

Table 4.1: Difference of methods and parameters between this chapter and previous chapter.

Methods and parameters	chapter 3 (or paper I)	this chapter	explanatory notes
Re-emission from gas	included	not included	For detail, see Section 4.3.1.
Re-emission from dust	included	not included	However, we include re-emission from dust for post-process analysis in this chapter. For detail, see Section 4.3.1.
Recombination coefficient of gas	Case A	Case B	For detail, see Section 4.3.2.
Hydrodynamic Scheme	AUSM+	SLAU2	For detail, see Section 4.3.3.
Dust temperature	Radiative equilibrium	Radiative equilibrium + dust-gas collision	For detail, see Section 4.4.2.

4.3.1 Radiation transfer

We here describe the algorithm that we use to solve the steady radiative transfer equation for a given frequency, ν:

$$\frac{dI_\nu}{d\tau_\nu} = -I_\nu + S_\nu, \tag{4.1}$$

where I_ν, τ_ν, and S_ν are the specific intensity, the optical depth, and the source function, respectively. Optical depth of a ray segment, $\Delta\tau_\nu$, is calculated by the same parameter as in paper I. Neglecting the effect of re-emission from dust should not affect our simulation results since optical thickness at infrared wavelength is much smaller than unity, and hence the effect of radiation pressure caused by infrared re-emission from dust grains is negligible. We, therefore, neglect the source function for radiation hydrodynamic simulations in this chapter.

Using the simulation results, we also perform the post-processing radiation transfer analysis to derive the spectral energy distribution (SED) of infrared re-emission from dust. In this analysis, we include the re-emission from dust as we did in paper I.

4.3.2 Chemical reaction and radiative cooling

Since we do not include the re-emission from gas in this chapter, we assume Case B for recombination coefficient of gas. In addition, we neglect the cooling below $< 10^4$ K. Other methods and parameters for chemical reaction and radiative cooling are same as in paper I.

4.3.3 Hydrodynamics

To investigate the spatial variation of the grain size distribution, we solve following hydrodynamics equations, where we consider dust grains with two sizes (dust-1

and dust-2):

$$
\begin{aligned}
\frac{\partial}{\partial t}\rho_{\rm g} + \frac{\partial}{\partial x}\rho_{\rm g} v_{\rm g} &= 0 \\
\frac{\partial}{\partial t}\rho_{\rm d1} + \frac{\partial}{\partial x}\rho_{\rm d1} v_{\rm d1} &= 0 \\
\frac{\partial}{\partial t}\rho_{\rm d2} + \frac{\partial}{\partial x}\rho_{\rm d2} v_{\rm d2} &= 0 \\
\frac{\partial}{\partial t}\rho_{\rm g} v_{\rm g} + \frac{\partial}{\partial x}\rho_{\rm g} v_{\rm g}^2 &= \rho_{\rm g} a_{\rm gra} + f_{\rm rad,g} - \frac{\partial}{\partial x} P_{\rm g} \\
&\quad + K_{\rm d1}(v_{\rm d1} - v_{\rm g}) + K_{\rm d2}(v_{\rm d1} - v_{\rm g}) \\
\frac{\partial}{\partial t}\rho_{\rm d1} v_{\rm d1} + \frac{\partial}{\partial x}\rho_{\rm d1} v_{\rm d1}^2 &= \rho_{\rm d1} a_{\rm gra} + f_{\rm rad,d1} \\
&\quad + K_{\rm d1}(v_{\rm g} - v_{\rm d1}) \qquad (4.2) \\
\frac{\partial}{\partial t}\rho_{\rm d2} v_{\rm d2} + \frac{\partial}{\partial x}\rho_{\rm d2} v_{\rm d2}^2 &= \rho_{\rm d2} a_{\rm gra} + f_{\rm rad,d2} \\
&\quad + K_{\rm d2}(v_{\rm g} - v_{\rm d2}) \qquad (4.3) \\
\frac{\partial}{\partial t}\left(\frac{1}{2}\rho_{\rm g} v_{\rm g}^2 + e_{\rm g}\right) &+ \frac{\partial}{\partial t}\left(\frac{1}{2}\rho_{\rm d1} v_{\rm d1}^2 + \frac{1}{2}\rho_{\rm d2} v_{\rm d2}^2\right) \\
+\frac{\partial}{\partial x}\left(\frac{1}{2}\rho_{\rm g} v_{\rm g}^2 + h_{\rm g}\right) v_{\rm g} &+ \frac{\partial}{\partial x}\left(\frac{1}{2}\rho_{\rm d1} v_{\rm d1}^3 + \frac{1}{2}\rho_{\rm d2} v_{\rm d2}^3\right) \\
&= (\rho_{\rm g} v_{\rm g} + \rho_{\rm d1} v_{\rm d1} + \rho_{\rm d2} v_{\rm d2})\, a_{\rm gra} \\
&\quad + f_{\rm rad,g} v_{\rm g} + f_{\rm rad,d1} v_{\rm d1} + f_{\rm rad,d2} v_{\rm d2}
\end{aligned}
$$

where $\rho_{\rm g}$ is the mass density of gas, $\rho_{\rm d1}$ is the mass density of dust-1, $\rho_{\rm d2}$ is the mass density of dust-2, $v_{\rm g}$ is the velocity of gas, $v_{\rm d1}$ is the velocity of dust-1, $v_{\rm d2}$ is the velocity of dust-2, $a_{\rm gra}$ is the gravitational acceleration, $f_{\rm rad,g}$ is the radiation pressure gradient force on gas, $f_{\rm rad,d1}$ is the radiation pressure gradient force on dust-1, $f_{\rm rad,d2}$ is the radiation pressure gradient force on dust-2, $K_{\rm d1}$ is the drag coefficient between gas and dust-1, $K_{\rm d2}$ is the drag coefficient between gas and dust-2, $e_{\rm g}$ is the internal energy of gas, and $h_{\rm g}$ is the enthalpy of gas. We define the gravitational acceleration $a_{\rm gra}$ as follows:

$$
a_{\rm gra} = -\frac{G M_{\rm BH}}{r^2},
$$

where $M_{\rm BH}$ is black hole mass, G is the gravitational constant, and r is the distance from a BH.

The drag coefficient $K_{\rm d}$ between gas and dust is defined as follows:

$$
K_{\rm d} \equiv \frac{n_{\rm d} F_{\rm drag}}{|\boldsymbol{v}_{\rm d} - \boldsymbol{v}_{\rm g}|}, \qquad (4.4)
$$

where $n_{\rm d}$ is the number density of dust grains, $v_{\rm d}$ is the velocity of dust grains, and $F_{\rm drag}$ is the drag force on dust grains. We calculate the drag force $F_{\rm drag}$ on dust of charge $Z_{\rm d}$ and radius $a_{\rm d}$ (Draine & Salpeter 1979) as follows:

$$
F_{\rm drag} = 2\pi a_{\rm d}^2 k_{\rm B} T_{\rm g} \left[\sum_i n_i \left(G_0(s_i) + z_i^2 \phi^2 \ln(\Lambda/z_i) G_2(s_i)\right)\right], \qquad (4.5)
$$

where

$$
\begin{aligned}
s_i &\equiv \sqrt{m_i(v_i - v_{\rm d})^2/(2k_{\rm B}T_{\rm g})}, \\
G_0(s_i) &\approx 8s_i/(3\sqrt{\pi})\sqrt{1 + 9\pi s_i^2/64}, \\
G_2(s_i) &\approx s_i/(3\sqrt{\pi}/4 + s_i^3), \\
\phi &\equiv Z_{\rm d}e^2/(a_{\rm d}k_{\rm B}T_{\rm g}), \\
\Lambda &\equiv 3/(2a_{\rm d}e|\phi|)\sqrt{k_{\rm B}T_{\rm g}/\pi n_{\rm e}},
\end{aligned}
$$

$k_{\rm B}$ is Boltzmann constant, $T_{\rm g}$ is the temperature of gas, n_i is the number density of the ith gas species (i =H I, H II, He I, He II, and He III), v_i is the velocity of the ith species, $n_{\rm e}$ is the number density of electron, z_i is the charge of the ith species, and m_i is the mass of the ith species.

In order to avoid the timesteps becoming too small, we set the maximum speed of the fluids. We assume that gas and dust can not exceed the speed of light. In addition, if the dust-to-gas mass ratio becomes smaller than 10^{-6} of the initial dust-to-gas mass ratio, we assume that speed of dust can not exceed three times larger than the speed of gas, since speed of dust tends to become too large in dust deficient regions. We have confirmed that these assumption do not affect our simulation results.

Hydrodynamics is solved by using a scheme called SLAU2 (Kitamura & Shima 2013). In addition, we use the sound speed as defined in Appendix D. Other methods for hydrodynamics (e.g. the method we solve the relative velocity between dust and gas) are same as in paper I.

4.4 Simulation setup

4.4.1 Dusty gas accretion and relative motion between dust and gas

In the first simulations (Section 4.5.1), in order to investigate whether relative motion between dust and gas affects the dusty gas accretion onto a BH, we perform three-fluid radiation hydrodynamic simulations. Since the typical mass of BHs formed by direct collapse is about 10^5 $M_\odot$ (e.g. Omukai et al. 2008), we set the mass of the BH as 10^5 $M_\odot$. For simplicity, we model a constant density cloud. As typical number density of molecular cloud in the interstellar medium is 10 cm^{-3} $\lesssim n_{\rm H} \lesssim$ 100 cm^{-3}, we set the hydrogen number density as $n_{\rm H}$ = 10, 30, and 100 cm^{-3}. Since we are interested in the effect of radiation pressure on dust grains on accretion rate, we need dust rich environments. We, therefore, set the metallicity as Z = 0.1 and 1.0 $Z_\odot$. In Appendix E and F, we perform additional simulation with different metallicity ($Z = 0.3$ $Z_\odot$) or black hole mass ($M_{\rm BH} = 3.33 \times 10^5$ and 10^6 $M_\odot$) to investigate the dependence of metallicity and black hole mass on accretion rate.

As the BH, we put a sink cell at the centre of the cloud. In order to resolve the Bondi radius $r_{\rm Bondi}$ ($r_{\rm Bondi} \sim 0.4(M_{\rm BH}/10^5 M_\odot)$ pc) within the H II regions, we

Table 4.2: Summary of the parameters we use in our simulations. $M_{\rm BH}$, $n_{\rm H}$, Z, and η indicate the BH mass, the initial number densities of hydrogen, metallicity, and radiative efficiency, respectively, in our simulations.

parameters	
$M_{\rm BH}$	$10^5 \ \ M_\odot$
$n_{\rm H}$	10, 30, 100 cm^{-3}
Z	0.1, 1.0 Z$_\odot$
η	0.1, 0.3

set the radius of the inner boundary (i.e. sink cell) as $10^{-2}(M_{\rm BH}/10^5 M_\odot)$ pc. To capture the H II regions inside the simulation box, we set the radius of the outer boundary as $10^3(M_{\rm BH}/10^5 M_\odot)$ pc. We set the number density of outer boundary as the initial number density of each simulations.

The radiative luminosity $L_{\rm acc}$ is defined as

$$L_{\rm acc} \equiv \eta \dot{m} c^2, \tag{4.6}$$

where η is constant radiative efficiency and $\dot{m}$ is the accretion rate, defined as the inflow rate into the sink cell. Since radiative efficiency η depends on the spin of BHs (Thorne 1974) and varies from ~ 0.05 to ~ 0.3, we set radiative efficiency as $\eta = 0.1, 0.3$ to investigate the effect of η on the accretion rates. We assume energy distribution L_ν as $L_\nu \propto \nu^{-1.5}$ with the frequency range 13.6 eV$\leq \nu \leq 10^4$ eV. We summarize the parameters we use in our simulations in Table 4.2.

To allow the dust grain-size distribution to change, we introduce two dust grains with two sizes, 0.01 and 0.1 μm. We call dust grains with size 0.1 μm and with size 0.01 μm dust as large dust and small dust, respectively. We assume the initial number ratio of large to small dust as

$$n_{\rm d,Large} : n_{\rm d,Small} = 1 : 10^{2.5},$$

where $n_{\rm d,Large}$ and $n_{\rm d,Small}$ are the number density of the large and small dust, respectively. This number ratio reproduces the mass absorption coefficient by the dust-size distribution of Mathis, Rumpl & Nordsieck (1977), so-called MRN distribution. We use logarithmically spaced 128 meshes in the radial direction and 60 meshes in the frequency direction in all simulations to solve radiation hydrodynamics. We perform each simulation for 10 Myrs to derive the time averaged and median values.

4.4.2 Spectral Energy Distribution (SED) of IR re-emission from dust

The lack of high temperature dust around active galactic nuclei was suggested by observations (e.g. z$\sim$ 6, Jiang et al. 2010; z$<$ 1, Lyu et al. 2017). To study whether relative motion can reproduce the lack of high temperature dust, we derive the SED of IR re-emission from dust by using the spatial distribution of dust and BH

luminosity obtained by the simulations. In order to derive the SED from dust IR re-emission, we determine the dust temperature $T_{\rm d}$ by using following equation:

$$4\pi \int \sigma_{{\rm d},\nu} B_{\rm v}(T_{\rm d}) d\nu = \Gamma_{\rm d} + \int \int \sigma_{{\rm d},\nu} I_{\nu}(\Omega) d\Omega d\nu, \tag{4.7}$$

where $\sigma_{{\rm d},\nu}$ is the cross section, $B_{\nu}(T_{\rm d})$ is the black body spectra, $\Gamma_{\rm d}$ is the collisional heating rate by gas (Draine & Sutin 1987), and Ω is solid angle. In order to remove the effect of the outer boundary regions, we only consider the re-emission from dust grains in H II regions. In the post-process SED calculations, we do not include the re-emission from dust grains if the number density is smaller than 10^{-10} times the initial number density, since the re-emission from dust grains with small number density is negligible.

Since stars are the main supplier of dust and stars mainly produce large dust, dust size distribution is dominated by large dust in the early stage of the galaxy evolution (Asano et al. 2013b; Aoyama et al. 2017; Hou et al. 2017). We, therefore, perform the additional numerical simulations assuming single large dust grain size (0.1 μm), in order to derive the SED of IR re-emission from dust in an early evolutionary stage of galaxies.

4.5 Results

4.5.1 The Eddington ratio and spatial distribution of dust

Time averaged Eddington ratio

Fig. 4.1 shows the time averaged Eddington ratio $\langle f_{\rm Edd} \rangle (\equiv \langle L_{\rm acc} \rangle / L_{\rm Edd})$, where $\langle L_{\rm acc} \rangle$ is the time averaged radiative luminosity and $L_{\rm Edd}$ is the Eddington luminosity derived by the cross section of electron. We derive the time averaged luminosity as:

$$\langle L_{\rm acc} \rangle \equiv \int_{0\ {\rm Myr}}^{10\ {\rm Myr}} L_{\rm acc} dt / (10\ {\rm Myr}). \tag{4.8}$$

The definition of $L_{\rm Edd}$ as follows:

$$L_{\rm Edd} \equiv \frac{4\pi G M_{\rm BH} m_{\rm p} c}{\sigma_{\rm T}}, \tag{4.9}$$

where $m_{\rm p}$ is the proton mass, $\sigma_{\rm T}$ is the Thomson cross section, and c is speed of light, In this chapter, Eddington luminosity is $L_{\rm Edd} \simeq 1.3{\times}10^{43} (M_{\rm BH}/10^5 M_{\odot})$ erg s^{-1}. We present $\langle f_{\rm Edd} \rangle$ as functions of the hydrogen number density $n_{\rm H}$, the metallicity Z, and the constant radiative efficiency η.

Except for $(\eta, Z) = (0.1, 0.1 Z_{\odot})$, the time averaged Eddington ratio becomes larger when relative motion between dust and gas is allowed. For example, the time averaged Eddington ratio becomes about 10 times larger by allowing relative motion between dust and gas with $(n_{\rm gas}, \eta, Z) = (100\ {\rm cm}^{-3}, 0.3, 1.0\ Z_{\odot})$. In later (Section 'Spatial dust distribution'), we describe why accretion rate becomes large by allowing the relative motion.

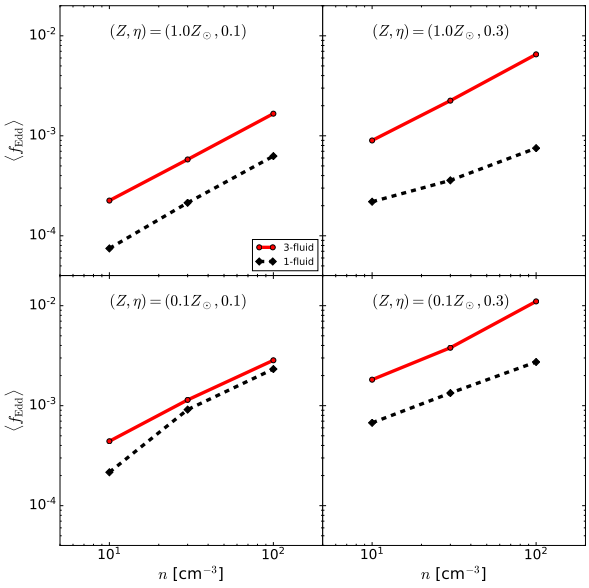

Figure 4.1: Time averaged Eddington ratio as a function of the hydrogen number density $n_{\rm H}$. Top panels show the results with the metallicity $Z = 1.0$ Z$_\odot$. Bottom panels show the results with the metallicity $Z = 0.1$ Z$_\odot$. Left panels show the results with the radiative efficiency $\eta = 0.1$. Right panels show the results with the radiative efficiency $\eta = 0.3$. The red solid lines represent the results of simulations that allow relative motion between dust and gas ('3-fluid'). The black dashed lines with filled diamond represent the results of simulations that assume dust and gas move together ('1-fluid').

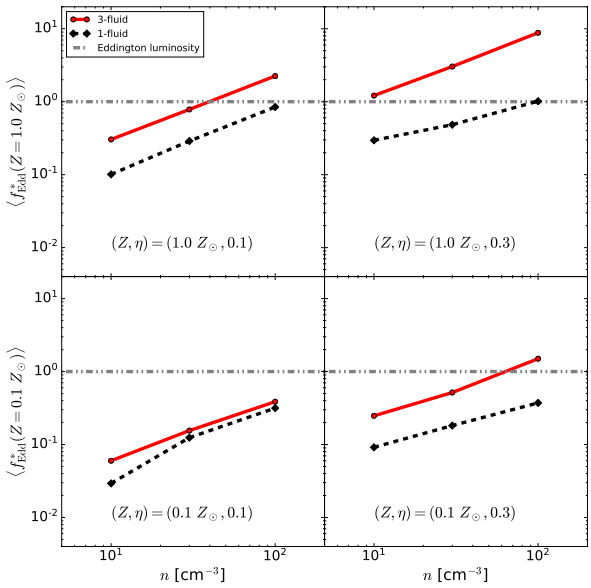

Figure 4.2: $\langle f^*_{\rm Edd}(Z)\rangle$ as a function of the hydrogen number density $n_{\rm H}$. Top panels show the results with metallicity $Z = 1.0$ Z$_\odot$. Bottom panels show the results with metallicity $Z = 0.1$ Z$_\odot$. Left panels show the results with radiative efficiency $\eta = 0.1$. Right panels show the results with radiative efficiency $\eta = 0.3$. The red solid lines represent the results of simulations that allow relative motion between dust and gas ('3-fluid'). The black dashed lines with filled diamond represent the results of simulations that assume dust and gas move together ('1-fluid'). The gray double dot-dashed lines represents $\langle f^*_{\rm Edd}(Z)\rangle = 1$.

Fig. 4.2 shows the time averaged Eddington ratio $\langle f^*_{\rm Edd}(Z)\rangle (\equiv \langle L_{\rm acc}\rangle / L^*_{\rm Edd}(Z))$, where $L^*_{\rm Edd}(Z)$ is the Eddington luminosity derived by the cross section of electron and dust. We define the $L^*_{\rm Edd}(Z)$ as follows:

$$L^*_{\rm Edd}(Z) \equiv \frac{4\pi G M_{\rm BH} m_{\rm p} c}{\sigma_{\rm T} + D(Z)\sigma_{\rm dust}}, \tag{4.10}$$

where $D(Z)$ is dust-to-gas mass ratio and $\sigma_{\rm dust}$ is the cross section of dust grains. From our dust model, we set $D(Z)\sigma_{\rm dust}$ as follows:

$$D(Z)\sigma_{\rm dust} \simeq 1.35 \times 10^3 (Z/Z_\odot)\sigma_{\rm T}. \tag{4.11}$$

The relation between $L_{\rm Edd}$ and $L^*_{\rm Edd}$ is $L_{\rm Edd} = L^*_{\rm Edd}(Z=0)$. As in Fig. 4.1, we present $\langle f^*_{\rm Edd}(Z)\rangle$ as functions of the hydrogen number density $n_{\rm H}$, the metallicity Z, and the constant radiative efficiency η in Fig. 4.2.

By allowing the relative motion, BH luminosity becomes about 10 times larger than the Eddington luminosity defined by cross section of dust and electron ($L^*_{\rm Edd}$) at most. Our result indicates that we may underestimate the BH luminosity if we use the parameter $L^*_{\rm Edd}$ to estimate the BH luminosity in sub-grid physics of cosmological simulations, for example.

According to equation (10) of Yajima et al. (2017), we estimate the accretion rate as follows:

$$\dot{M} = \dot{M}_{\rm B,HII}\left[1 - \frac{1.35\times 10^3 \sigma_{\rm T}\eta c}{4\pi G M_{\rm BH} m_{\rm p}}\left(\frac{Z}{Z_\odot}\right)\times \dot{M}\right]^2, \tag{4.12}$$

where

$$\dot{M}_{\rm B,HII} \equiv 4\pi\lambda_B (=0.75) G^2 M^2_{\rm BH}\rho_{\rm HII} c^{-3}_{\rm HII}, \tag{4.13}$$

$\rho_{\rm HII}$ is the number density of ionized hydrogen, and $c_{\rm HII}$ is the sound speed inside the H II region. We assume that the temperature of ionized gas is 7×10^4 K and the polytropic index γ is 1.3. Since the dust model is different from Yajima et al. (2017), our equation (4.12) is different from equation (10) of Yajima et al. (2017).

As in Fig. 4.1, we present the time averaged Eddington ratio as a functions of the hydrogen number density, metallicity, and constant radiative efficiency in Fig. 4.3. We also present the Eddington ratio obtained by equation (4.12).

We find that the accretion rate for $(\eta, Z) = (0.1, 0.1Z_\odot)$ does not become sufficiently large by allowing the relative motion between dust and gas, since the accretion rate by equation (4.12) shows that the accretion rate for $(\eta, Z) = (0.1, 0.1Z_\odot)$ does not differ from that for $(\eta, Z) = (0.1, 0.0Z_\odot)$ very much. The effect of radiation pressure on dust is almost negligible for $(\eta, Z) = (0.1, 0.1Z_\odot)$. We discuss the metallicity dependence on accretion rate in Appendix E.

As we show in Fig. 4.3, the accretion rate by '3-fluid' for $(Z, \eta) = (0.1\ Z_\odot, 0.3)$ agrees well with the accretion rate given by equation (4.12) with $(Z, \eta) = (0.0\ Z_\odot, 0.3)$. When we assume that the accretion rate by '3-fluid' for $(Z, \eta) = (0.1\ Z_\odot, 0.3)$ follows the accretion rate given by equation (4.12) with $(Z, \eta) = (0.0\ Z_\odot, 0.3)$

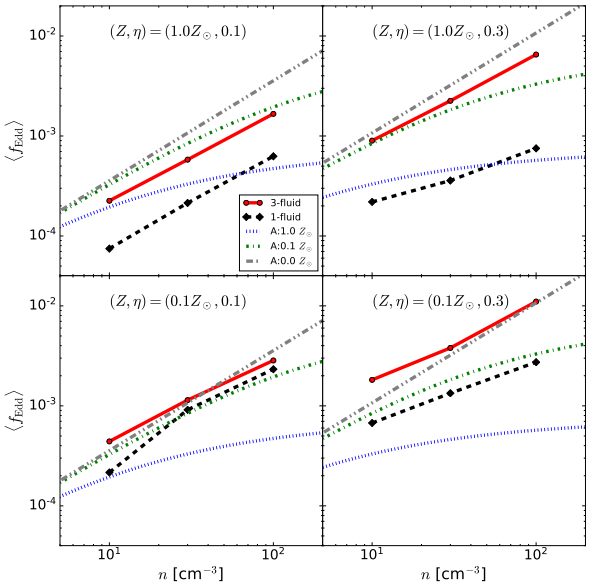

Figure 4.3: Time averaged Eddington ratio as a function of the hydrogen number density $n_{\rm H}$. Top panels show the results with metallicity $Z = 1.0$ Z$_\odot$. Bottom panels show the results with metallicity $Z = 0.1$ Z$_\odot$. Left panels show the results with radiative efficiency $\eta = 0.1$. Right panels show the results with radiative efficiency $\eta = 0.3$. The red solid lines represent the results of simulations that allow relative motion between dust and gas ('3-fluid'). The black dashed lines with filled diamond represent the results of simulations that assume dust and gas move together ('1-fluid'). The blue dotted lines, the green dot-dashed lines, and gray double dot-dashed lines represent the Eddington ratio given by equation (4.12) with metallicity 1.0 $Z_\odot$, 0.1 $Z_\odot$, and 0.0 $Z_\odot$.

even with the hydrogen number density $n_{\rm H} = 10^5$ cm^{-3}, the accretion rate of '3-fluid' with $(Z, \eta) = (0.1\ Z_\odot, 0.3)$ can reach the Eddington accretion rate for $(Z, \eta) = (0.0\ Z_\odot, 0.3)$. If the accretion rate of dusty gas is the Eddington accretion rate for $(Z, \eta) = (0.0\ Z_\odot, 0.3)$, it takes about 1 Gyr to be SMBHs of mass $10^9\ M_\odot$ from seed BHs of mass $10^5\ M_\odot$. A black hole might be able to grow even under dust rich environments by allowing the relative motion between dust and gas.

In the previous paragraph, we assume that the accretion rate by '3-fluid' for $(Z, \eta) = (0.1\ Z_\odot, 0.3)$ follows the rate given by equation (4.12) for $(Z, \eta) = (0.0\ Z_\odot, 0.3)$ even with higher gas number density. This assumption, however, may not be valid. Toyouchi et al. (2019) showed that the effect of infrared re-emission from dust grains on dusty gas accretion is not negligible in high density environments. We, therefore, need to carry out '3-fluid' simulations including the effect of re-emission from dust grains in high gas density to derive the accretion rate in dusty high density environments. Such simulations are. however, computationally too expensive.

Time evolution of Eddington ratio

We present the time evolution of Eddington ratio in Fig. 4.4. Time evolution of Eddington ratio also indicates that accretion rate increases by allowing the relative motion between dust and gas. In addition, by allowing the relative motion, time evolution of Eddington ratio shows large variation. As we discuss later (Section 4.5.2), the dust-to-gas mass ratio depends on the luminosity of BHs when we allow the relative motion between dust and gas. Since the effect of radiation pressure on dusty gas accretion also depends on the dust-to-gas mass ratio, changes of the luminosity also affects the role of radiation pressure on dusty gas accretion. This effect may cause the large and frequent fluctuation in time evolution of Eddington ratio in the '3-fluid' case.

Spatial dust distribution

We present densities, velocities, relative velocities between dust and gas ($\Delta v \equiv v_{\rm d} - v_{\rm g}$), the grain electric potential, and gas temperature as functions of radius in Fig. 4.5. In order to compare the simulation results with each other, we consider the specific epoch of each initial condition when the luminosity is median. [1]

We find that radiation pressure affects the dust distribution within an ionized regions. Except for the immediate vicinity of a BH, the dust-to-gas mass ratio decreases within an ionized region. The effect of radiation pressure on dusty gas, therefore, becomes small. This makes the accretion rate larger than the one-fluid case as we discussed in Section 'Time averaged Eddington ratio'.

We find that the relative speed between large dust and gas is larger than that between small dust and gas. This is because large dust grains have larger

[1] We select the specific epoch of each initial condition from 2 Myr to 10 Myr in order to remove the epochs when simulation results are largely affected by initial gas distribution.

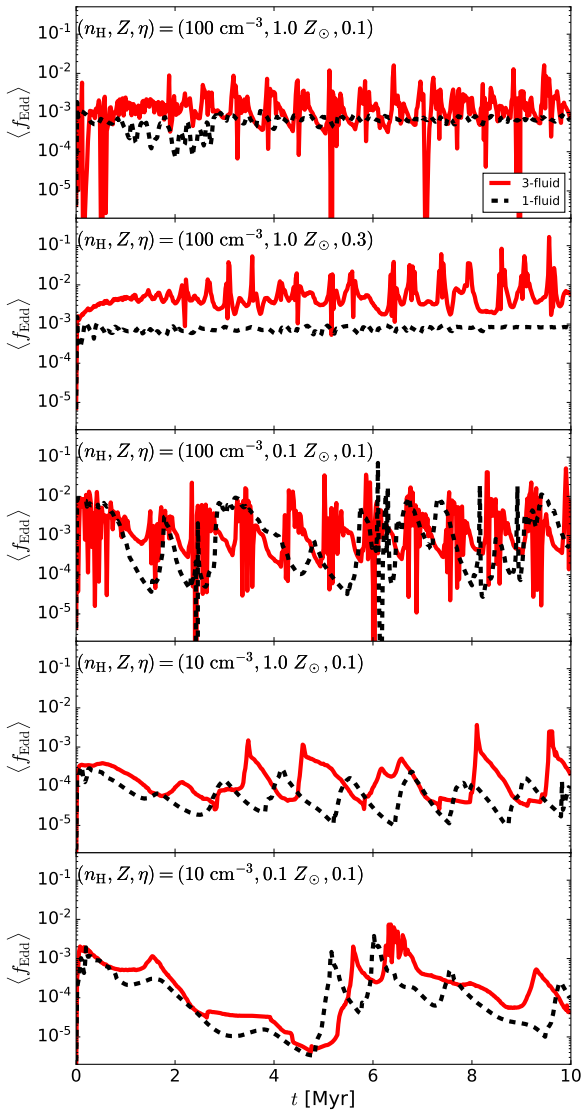

Figure 4.4: Eddington ratio as a function of time t. From top to bottom, panels show the results with $(n_{\rm H}, Z, \eta) = (100\ {\rm cm}^{-3}, 1.0\ {\rm Z}_\odot, 0.1)$, $(n_{\rm H}, Z, \eta) = (100\ {\rm cm}^{-3}, 1.0\ {\rm Z}_\odot, 0.3)$, $(n_{\rm H}, Z, \eta) = (100\ {\rm cm}^{-3}, 0.1\ {\rm Z}_\odot, 0.1)$, $(n_{\rm H}, Z, \eta) = (10\ {\rm cm}^{-3}, 1.0\ {\rm Z}_\odot, 0.1)$, and $(n_{\rm H}, Z, \eta) = (10\ {\rm cm}^{-3}, 0.1\ {\rm Z}_\odot, 0.1)$. The red solid lines represent the results of simulations that allow the relative motion between dust and gas ('3-fluid'). The black dashed lines represent the results of simulations that assume dust and gas move together ('1-fluid').

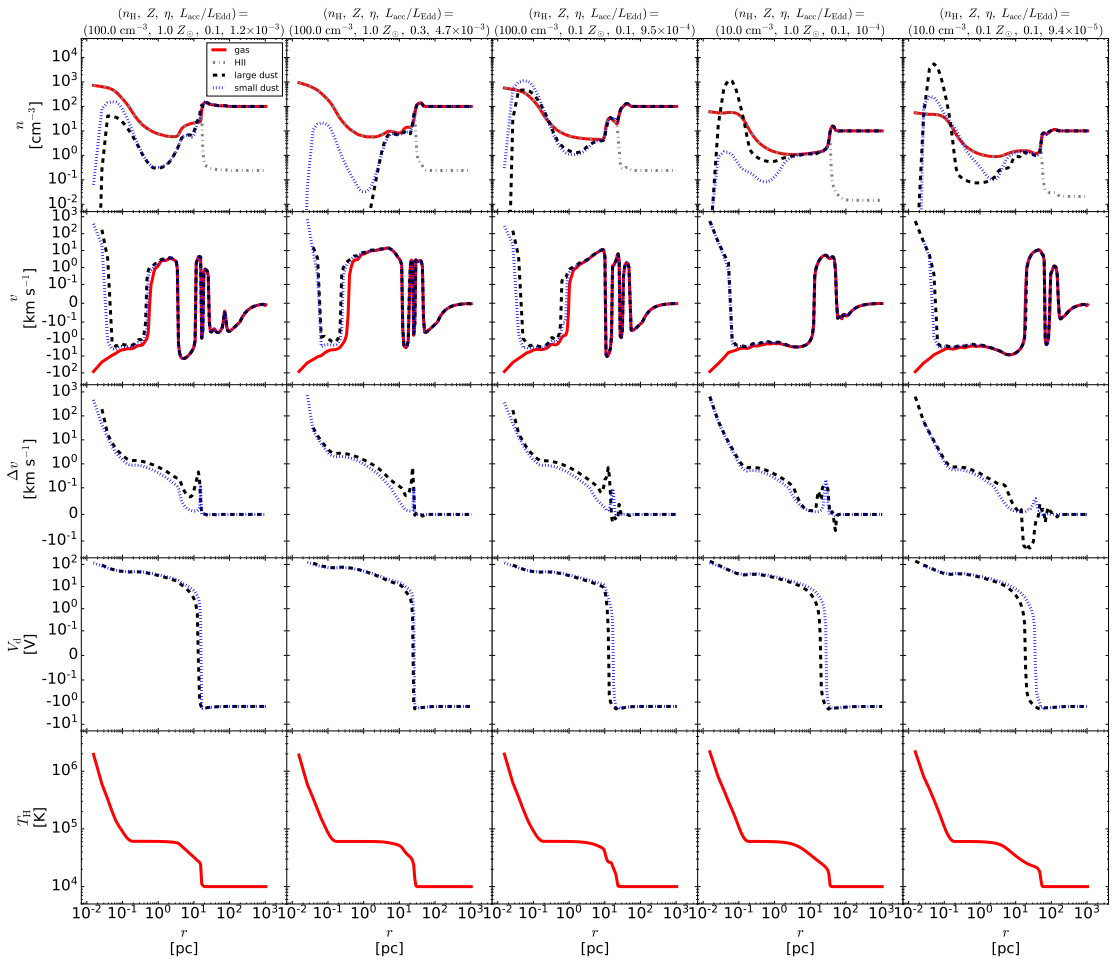

Figure 4.5: Density (top-row), velocity (second-row), relative velocity between dust and gas (third-row), grain electric potential (fourth-row), and gas temperature (bottom-row) profiles. From left to right, we show the results for $(n_{\rm H}, Z, \eta) = (100\ {\rm cm}^{-3}, 1.0\ {\rm Z}_{\odot}, 0.1)$, $(n_{\rm H}, Z, \eta) = (100\ {\rm cm}^{-3}, 1.0\ {\rm Z}_{\odot}, 0.3)$, $(n_{\rm H}, Z, \eta) = (100\ {\rm cm}^{-3}, 0.1\ {\rm Z}_{\odot}, 0.1)$, $(n_{\rm H}, Z, \eta) = (10\ {\rm cm}^{-3}, 1.0\ {\rm Z}_{\odot}, 0.1)$, and $(n_{\rm H}, Z, \eta) = (10\ {\rm cm}^{-3}, 0.1\ {\rm Z}_{\odot}, 0.1)$. All profile present the results during the median luminosity. In the top-row, the red solid lines and gray dot-dashed lines represent hydrogen number density and H II number density. The black dashed lines and blue dotted lines show the large dust number density normalized by hydrogen number density and the small dust number density normalized by hydrogen number density. In the second-row, the red solid lines, the black dashed lines, and blue dashed lines show the the velocity of gas, large dust, and small dust, respectively. In the third-row, the black dashed lines and blue dotted lines show the relative velocity between large dust and gas and between small dust and gas, respectively. In the forth-row, the black dashed lines and blue dotted lines show the electric potential of the large dust and the small dust, respectively. In the bottom panels, the red solid lines show the gas temperature. We do not plot the profiles of dust grains if the normalized number density of dust becomes smaller than 10^{-6}, since we assume different maximum velocity under low dust-to-gas mass ratio as we discuss in Section 4.3.3.

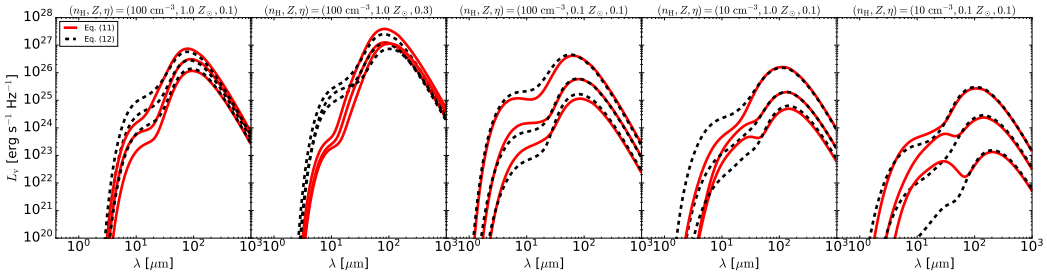

Figure 4.6: The spectral energy distribution (SED) of dust re-emission profiles as a function of wavelength when the BH luminosity is 'faint', 'median', and 'bright'. From left to right, we show the results for $(n_{\rm H}, Z, \eta) = (100\ {\rm cm}^{-3}, 1.0\ {\rm Z}_\odot, 0.1)$, $(n_{\rm H}, Z, \eta) = (100\ {\rm cm}^{-3}, 1.0\ {\rm Z}_\odot, 0.3)$, $(n_{\rm H}, Z, \eta) = (100\ {\rm cm}^{-3}, 0.1\ {\rm Z}_\odot, 0.1)$, $(n_{\rm H}, Z, \eta) = (10\ {\rm cm}^{-3}, 1.0\ {\rm Z}_\odot, 0.1)$, and $(n_{\rm H}, Z, \eta) = (10\ {\rm cm}^{-3}, 0.1\ {\rm Z}_\odot, 0.1)$. The red solid lines represent the results of simulations derived by equation (4.14). The black dashed lines represent the fixed SED derived by equation (4.15).

absorption coefficient (Draine & Lee 1984; Laor & Draine 1993), smaller dust charge [2], and larger drag time.

4.5.2 Spectral Energy Distribution of IR re-emission by dust grains

Spectral energy distribution & MRN like dust size distribution

We present the spectral energy distribution (SED) of dust re-emission as a function of wavelength in Fig. 4.6. In order to study the luminosity dependence of SED shapes, we select the specific snapshots when the luminosity is 'faint', 'median', and 'bright'. The definitions of 'faint', 'median' and 'bright' luminosity are as follows:

'faint': The BH luminosity is in the bottom 12.5% from 2 Myr to 10 Myr.

'median': The BH luminosity is in the median from 2 Myr to 10 Myr.

'bright': The BH luminosity is in the top 12.5% from 2 Myr to 10 Myr.

Since we are mainly interested in the SED in a quasi-steady phase, we do not include the data until 2 Myr. In Fig. 4.6, it is possible to differentiate these cases ('faint', 'median', and 'bright') by considering the value at wavelength $\lambda \sim 10^2\ \mu$m: 'faint' shows lowest value; whereas, 'bright' is highest; and 'median' is between these, as could be expected.

Red solid lines indicate the SEDs derived by the spatial distribution of dust grains obtained by the simulations. In order to estimate the effect of relative motion between dust and gas, we also present the SEDs with a fixed dust-to-gas

[2] Since photoelectric yield of large dust is smaller than that of small dust grains (Weingartner & Draine 2001a; Weingartner et al. 2006), electric potential of large dust grains is smaller than that of small dust grains.

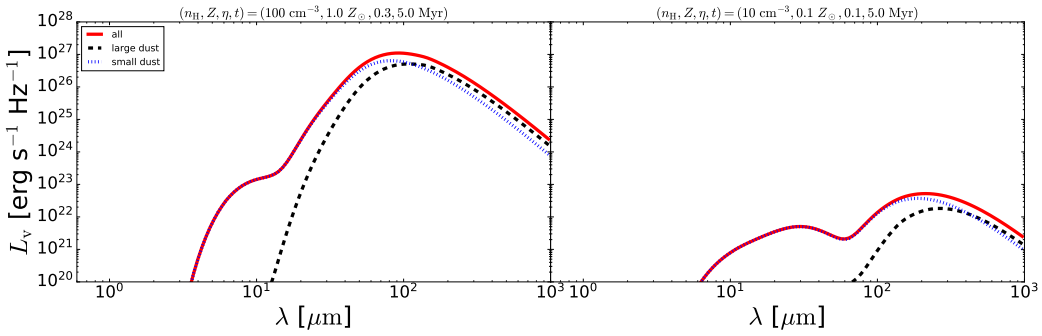

Figure 4.7: The spectral energy distribution (SED) from dust re-emission profiles as a function of wavelength at $t = 5.0$ Myr. From left to right, we show the results for $(n_{\rm H}, Z, \eta) = (100\ {\rm cm}^{-3}, 1.0\ {\rm Z}_\odot, 0.3)$ and $(n_{\rm H}, Z, \eta) = (10\ {\rm cm}^{-3}, 0.1\ {\rm Z}_\odot, 0.1)$. The red solid lines represent the total SED of dust re-emission from small dust and large dust. The black dashed lines represent the SED of dust re-emission from large dust. The blue dotted lines represent the SED of dust re-emission from small dust.

mass ratio by black dashed lines. In other words, we estimate the SEDs described by the red solid lines by the following radiative transfer equation:

$$\begin{aligned}\frac{dI_\nu}{ds} &= \rho_{\rm d,Large,\nu}\kappa_{\rm d,Large,\nu}(-I_\nu + B_\nu(T_{\rm d,Large})) \\ &\quad +\rho_{\rm d,Small,\nu}\kappa_{\rm d,Small,\nu}(-I_\nu + B_\nu(T_{\rm d,Small})),\end{aligned} \tag{4.14}$$

and we estimate the SEDs presented by the black dashed lines by the following radiative transfer equation:

$$\begin{aligned}\frac{dI}{ds} &= \rho_{\rm g}\left(\frac{\rho_{\rm d,Large}}{\rho_{\rm g}}\right)_{\rm int}\kappa_{\rm d,Large}(-I + B(T_{\rm d,Large})) \\ &\quad +\rho_{\rm g}\left(\frac{\rho_{\rm d,Small}}{\rho_{\rm g}}\right)_{\rm int}\kappa_{\rm d,Small}(-I + B(T_{\rm d,Small})),\end{aligned} \tag{4.15}$$

where $T_{\rm d,Large}$ is the temperature of large dust (dust grains with the size 0.1 μm), $T_{\rm d,Small}$ is the temperature of small dust (dust grains with the size 0.01 μm), $\kappa_{\rm d,Large}$ is the mass absorption coefficient of large dust, $\kappa_{\rm d,Small}$ is the mass absorption coefficient of small dust, $B(T)$ is the black body radiation with temperature T, $(\rho_{\rm d,Large}/\rho_{\rm gas})_{\rm int}$ is the initial large-dust-to-gas mass ratio, and $(\rho_{\rm d,Small}/\rho_{\rm gas})_{\rm int}$ is the initial small-dust-to-gas mass ratio.

Since the dust-to-gas mass ratio inside H II regions is largely changed by the relative motion between gas and dust as we showed in Section 4.5.1, the SEDs are also affected by the relative motion, in particular at $\lambda \simeq 10$ μm. The inclusion of the relative motion sometimes makes the luminosity at this wavelength fainter or brighter than the coupled cases. This indicates that the spatial distribution of high temperature dust with $\sim 10^3$ K is strongly affected by the radiation pressure.

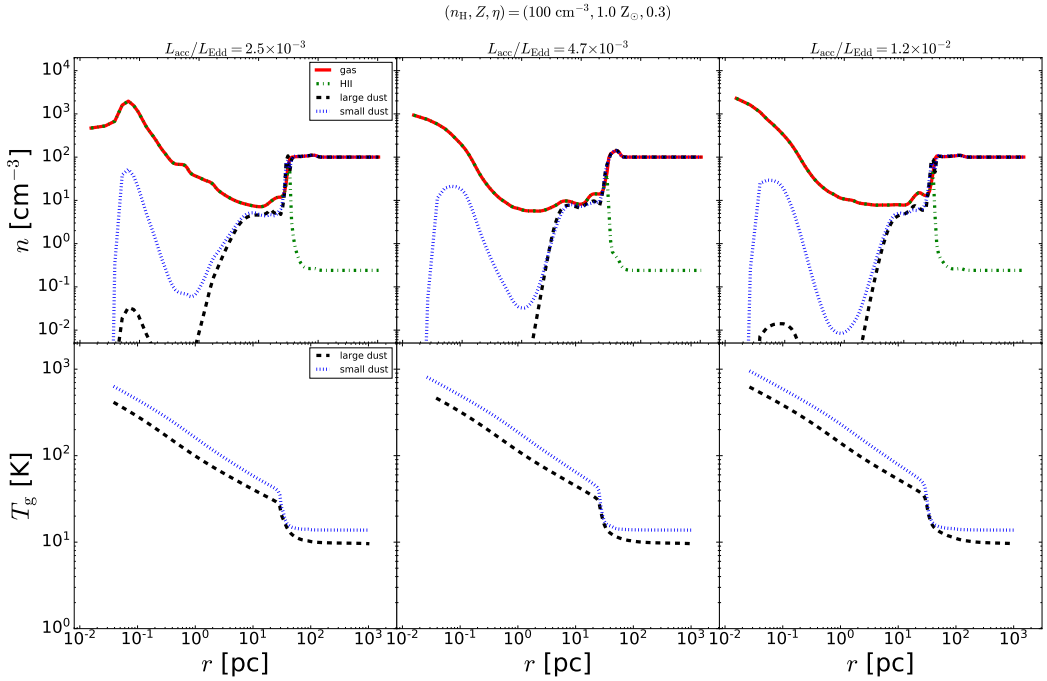

Figure 4.8: Density (top-row) and dust temperature (bottom-row) profiles. We show the results for $(n_{\rm H}, Z, \eta) = (100\ {\rm cm}^{-3}, 1.0\ {\rm Z}_\odot, 0.3)$. From left to right, we show the results when the BH luminosity is 'faint', 'median', and 'bright'. In the top-row, the red solid lines and gray dot-dashed lines represent the number density of hydrogen and H II. The black dashed lines and blue dotted lines show the large dust number density normalized by hydrogen number density and the small dust number density normalized by hydrogen number density. In the bottom-row, the black dashed lines and blue dotted lines represents the temperature of large dust and small dust.

To investigate which dust is responsible for this change, we present contributions of large dust and small dust separately in Fig. 4.7, in which we show the SEDs at $t = 5$ Myr for $(n_{\rm H}, Z, \eta) = (100{\rm cm}^{-3}, 1.0, 0.3)$ and $(n_{\rm H}, Z, \eta) = (10{\rm cm}^{-3}, 0.1, 0.1)$, respectively. The relative motion makes the luminosity at $\lambda \simeq 10\ \mu$m fainter for the former and brighter for the latter compared with the coupled cases. We find that small dust is responsible for the luminosity at this wavelength.

To study the connection between the distribution of small dust, which is accreted by radiation, and the dust re-emission luminosity at $\lambda \simeq 10\ \mu$m, we present densities and dust temperatures as functions of radius in Fig. 4.8 for $(n_{\rm H}, Z, \eta) = (100\ {\rm cm}^{-3}, 1.0\ \odot, 0.3)$ and Fig. 4.9 for $(n_{\rm H}, Z, \eta) = (10\ {\rm cm}^{-3}, 1.0\ \odot, 0.1)$. The profiles shown are again those at the black hole luminosity is 'faint', 'median', and 'bright' in Fig. 4.6.

We find that dust is removed from the H II region in the case of $(n_{\rm H}, Z, \eta) = (100\ {\rm cm}^{-3}, 1.0\ \odot, 0.3)$. This is because higher luminosity makes the relative velocity between dust and gas larger and removes the dust grains from the central

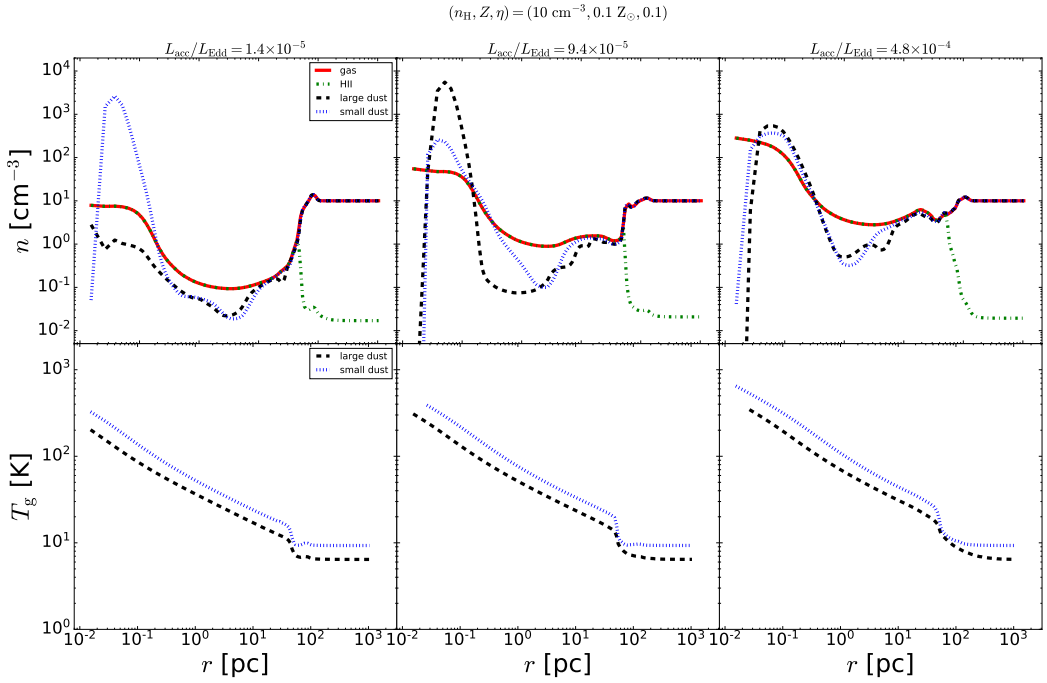

Figure 4.9: Density (top-row) and dust temperature (bottom-row) profiles. We show the results for $(n_{\rm H}, Z, \eta) = (10\ {\rm cm}^{-3}, 0.1\ {\rm Z}_\odot, 0.1)$. From left to right, we show the results when the BH luminosity is 'faint', 'median', and 'bright'. In the top-row, the red solid lines and gray dot-dashed lines represent the number density of hydrogen and H II. The black dashed lines and blue dotted lines show the large dust number density normalized by hydrogen number density and the small dust number density normalized by hydrogen number density. In the bottom-row, the black dashed lines and blue dotted lines represents the temperature of large dust and small dust.

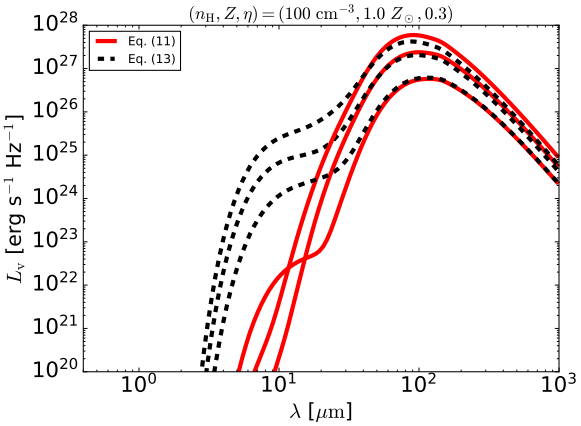

Figure 4.10: The spectral energy distribution (SED) of dust re-emission profiles as a function of wavelength when the BH luminosity is 'faint', 'median', and 'bright'. We show the results for $(n_{\rm H}, Z, \eta) = (100\ {\rm cm}^{-3}, 1.0\ {\rm Z}_\odot, 0.3)$. The red solid lines represent the results of simulations. The black dashed lines represent the fixed SED derived by equation (4.15). Compare with Fig. 4.6, dust with size 0.01 μm is not included in this numerical simulation.

region more efficiently, This decreases the amount of the high temperature dust. On the other hand, small dust is gathered around the BH at $r \sim 0.1$ pc in the case of $(n_{\rm H}, Z, \eta) = (10\ {\rm cm}^{-3}, 1.0\ \odot, 0.1)$, which is heated to $\sim 10^3$ K.

The effect of grain-size distribution on the SED

We perform an additional simulation only with large dust (dust grains at size 0.1 μm) and present the spectral energy distribution (SED) of the dust re-emission as a function of wavelength in Fig. 4.10. In order to estimate the BH radiative luminosity dependence on SED shapes, we select the epochs when the luminosity is 'faint', 'median', and 'bright' as in Fig. 4.6. Red solid lines and black dashed lines are the same as in Fig. 4.6.

We compare the SEDs in Fig. 4.10 and Fig. 4.6 around $\lambda \sim 10$ μm with initial condition $(n_{\rm H}, Z, \eta) = (100\ {\rm cm}^{-3}, 1.0\ {\rm Z}_\odot, 0.3)$ and find that decline of re-emission from high temperature dust becomes larger when we only include large dust.

We present densities and dust temperature as functions of radius in Fig. 4.11 as in Fig. 4.8 for $(n_{\rm H}, Z, \eta) = (100\ {\rm cm}^{-3}, 1.0\ Z_\odot, 0.3)$. Since radiation pressure removes large dust more effectively than small dust as we discussed in Section 4.5.1, the total amount of dust grains in the H II region shown in Fig. 4.11 becomes smaller than in the two size case. The decrease of SED around $\lambda \sim 10$ μm in Fig. 4.10, therefore, becomes larger than in Fig. 4.6.

The flux ratio & spatial distribution of dust grains

Yajima et al. (2017) showed that there are tight correlation between Eddington ratio and the flux density ratio between 14 μm and 140 μm. We, therefore,

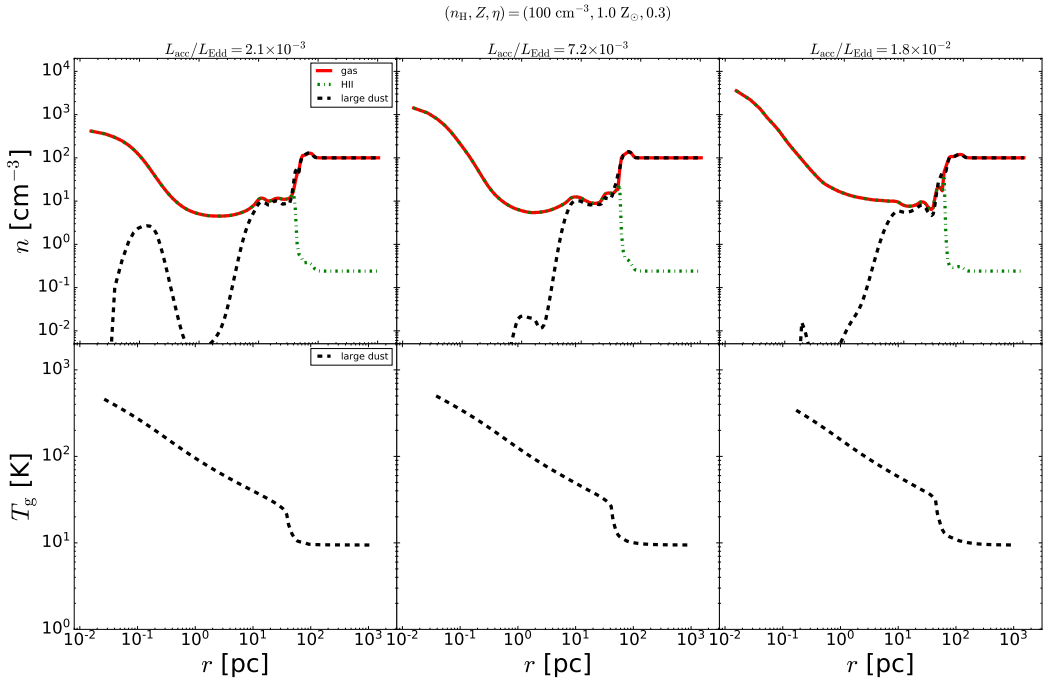

Figure 4.11: Density (top-row) and dust temperature (bottom-row) profiles. We show the results for $(n_{\rm H}, Z, \eta) = (100\ {\rm cm}^{-3}, 1.0\ {\rm Z}_{\odot}, 0.3)$. Compare with Fig. 4.8, dust with size 0.01 μm is not included in this numerical simulation. From left to right, we show the results when the BH luminosity is 'faint', 'median', and 'bright'. In the top-row, the red solid lines and gray dot-dashed lines represent the number density of hydrogen and H II. The black dashed lines show the large dust number density normalized by hydrogen number density. In the bottom-row, the black dashed lines represent the temperature of large dust.

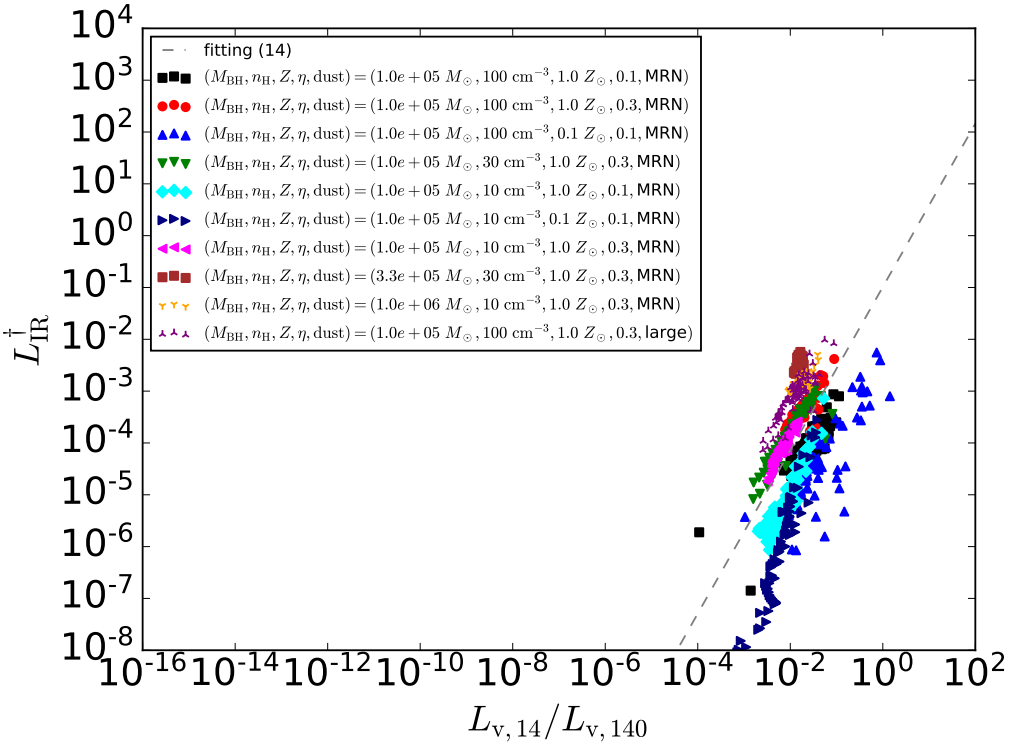

Figure 4.12: Normalized bolometric infrared luminosity $L^\dagger_{\rm IR}(\equiv L_{\rm IR}/(1.3\times10^{43}\mathrm{erg\ s^{-1}}))$ as a function of flux density ratio between 14 μm and 140 μm ($f_{14/140}$). Bolometric infrared luminosity $L_{\rm IR}$ is derived by equation (4.15). Different symbols represent simulation results with different BH mass ($M_{\rm BH}$), initial hydrogen number density ($n_{\rm H}$), metallicity (Z), radiative efficiency (η), and dust grain size distribution model (dust). 'MRN' represents the simulation results assuming MRN dust size distribution and 'large' represents the simulation results only with large dust. The gray dashed line represents fitting function (4.16).

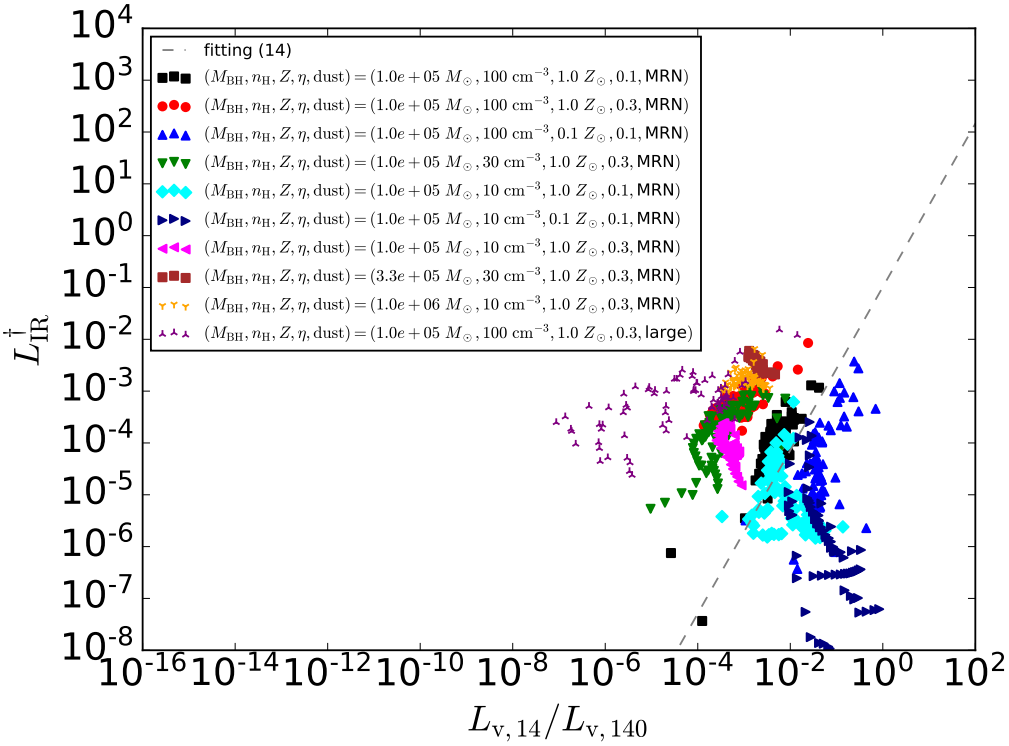

Figure 4.13: Normalized bolometric infrared luminosity $L^\dagger_{\rm IR}(\equiv L_{\rm IR}/(1.3\times10^{43}\mathrm{erg\ s^{-1}}))$ as a function of flux density ratio between 14 μm and 140 μm ($f_{14/140}$). Bolometric infrared luminosity $L_{\rm IR}$ is derived by equation (4.14). Different symbols represent simulation results with different BH mass ($M_{\rm BH}$), initial hydrogen number density ($n_{\rm H}$), metallicity (Z), radiative efficiency (η), and dust grain size distribution model (dust). 'MRN' represents the simulation results assuming MRN dust size distribution and 'large' represents the simulation results only with large dust. The gray dashed line represents fitting function (4.16).

show the relation between the normalized bolometric infrared luminosity $L^{\dagger}_{\rm IR}(\equiv L_{\rm IR}/(1.3\times10^{43}{\rm erg\ s^{-1}}))$ and the flux density ratio between 14 μm and 140 μm $f_{14/140}$ in Fig. 4.12 and 4.13. $L_{\rm IR}$ represents the bolometric infrared luminosity (i.e. total infrared luminosity emitted from dust grains). Fig. 4.12 is derived by assuming an uniform dust-to-gas mass ratio (equation (4.15)) and Fig. 4.13 is by the dust distribution obtained from the simulations (equation (4.14)).

We find that the relation between $L^{\dagger}_{\rm IR}$ and $f_{14/140}$ is tightly correlated in Fig. 4.12 even with different black hole mass, dust grain size distribution, initial number density of gas, initial dust-to-gas mass ratio, and radiative efficiency. This correlation can be roughly fitted by the following relationship:

$$L^{\dagger}_{\rm IR}\sim 0.1(f_{14/140})^{1.6}, \tag{4.16}$$

or

$$f_{14/140}\sim 4.3(L^{\dagger}_{\rm IR})^{0.6}\equiv F(L^{\dagger}_{\rm IR}). \tag{4.17}$$

The gray dashed lines in Fig. 4.12 and 4.13 represent fitting function (4.16). On the other hand, we can not find tight correlation when we use the dust distribution obtained from the simulation (Fig. 4.13). Since the infrared re-emission at wavelength 14 μm emitted by high temperature dust grains near BHs (i.e. $r\sim 0.1$ pc with black hole mass $M_{\rm BH}=10^5\ M_{\odot}$), this scatter may come from changes in dust-to-gas mass ratio near BHs. Fig. 4.5, 4.8, 4.9, and 4.11 show that the dust-to-gas mass ratio near BHs changes by allowing the relative motion between dust and gas.

In order to confirm that the scatter in Fig. 4.13 is originated by the variation in the dust-to-gas mass ratio near BHs, we present $(\rho_{\rm dust}/\rho_{\rm gas})_{\rm nearBH}/(\rho_{\rm dust}/\rho_{\rm gas})_{\rm init}$ (where $(\rho_{\rm dust}/\rho_{\rm gas})_{\rm nearBH}$ is the dust-to-gas mass ratio at $r_{\rm nearBH}\simeq 0.25r_{\rm Bondi}$ and $(\rho_{\rm dust}/\rho_{\rm gas})_{\rm init}$ is the initial dust-to-gas mass ratio) as a function of $f_{14/140}/F(L^{\dagger}_{\rm IR})$ in Fig. 4.14 by using the data in Fig. 4.13.

Fig. 4.14 shows that there is the tight correlation between $(\rho_{\rm dust}/\rho_{\rm gas})_{\rm nearBH}/(\rho_{\rm dust}/\rho_{\rm gas})_{\rm init}$ and $f_{14/140}/F(L^{\dagger}_{\rm IR})$. This tight correlation can also be roughly fitted by the following relationship:

$$\frac{(\rho_{\rm dust}/\rho_{\rm gas})_{\rm nearBH}}{(\rho_{\rm dust}/\rho_{\rm gas})_{\rm init}}\sim 0.13\left(\frac{f_{14/140}}{F(L^{\dagger}_{\rm IR})}\right)^{0.7}. \tag{4.18}$$

Gray dashed line in Fig. 4.14 represents the fitting function (4.18). This result indicates that we can derive dust-to-gas mass ratio near BHs from $f_{14/140}$, $L_{\rm IR}$, fitting function (4.17), and fitting function (4.18).

Fig. 4.6 and 4.10 indicate that the relative motion changes the flux density at 14 μm while it leaves the flux density at 140 μm unchanged. This result suggests that there must be some kind of relationship between the amount of hot dust near BHs and the flux density at 14 μm, which is emitted by hot dust. This can be explained as follows: The total absorption coefficient $\alpha_{{\rm d},\nu}$ of dust for a given frequency ν is:

$$\alpha_{{\rm d},\nu}=\sum_i\frac{\pi a^2_{{\rm d},i}Q_{i,\nu}}{M_{{\rm d},i}}\rho_{{\rm d},i}, \tag{4.19}$$

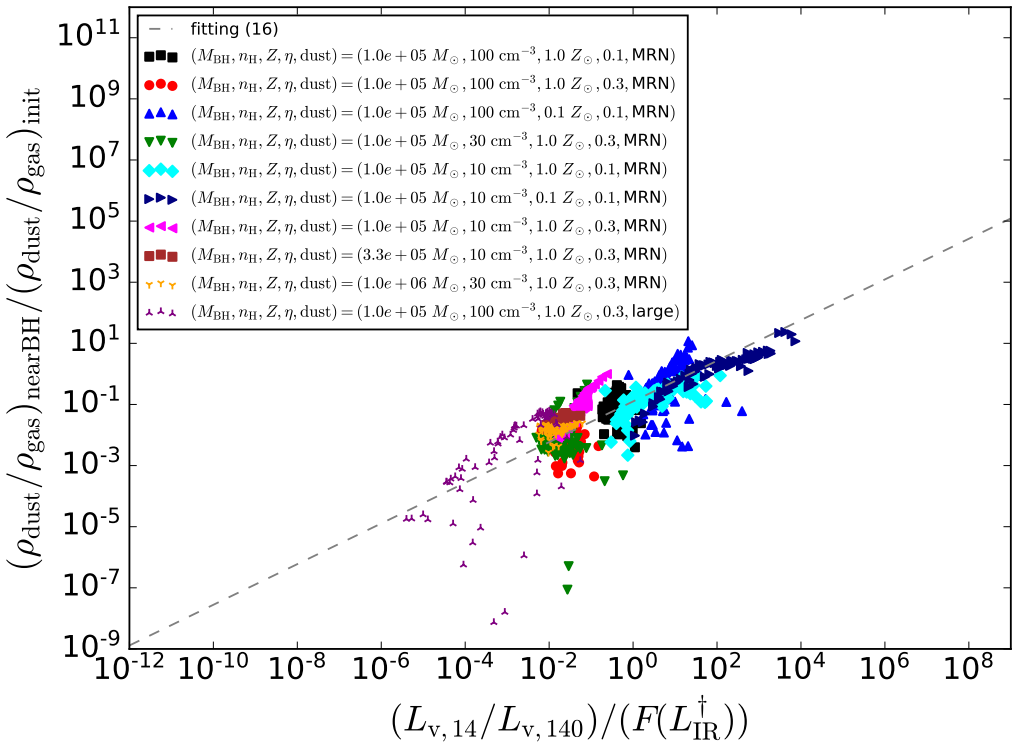

Figure 4.14: The rate between dust-to-gas mass ratio at radius $r \simeq 0.25 r_{\rm Bondi}$ and initial dust-to-gas mass ratio ($(\rho_{\rm dust}/\rho_{\rm gas})_{\rm nearBH}/(\rho_{\rm dust}/\rho_{\rm gas})_{\rm init}$) as a function of $f_{14/140}/F(L^{\dagger}_{\rm IR})$. Bolometric infrared luminosity $L_{\rm IR}$ is derived by equation (4.14). Different symbols represent simulation results with different BH mass ($M_{\rm BH}$), initial hydrogen number density ($n_{\rm H}$), metallicity (Z), radiative efficiency (η), and dust grain size distribution model (dust). 'MRN' represents the simulation results assuming MRN dust size distribution and 'large' represents the simulation results only with large dust. The gray dashed line represents fitting function (4.18).

where $\rho_{\mathrm{d},i}$ is the mass density of dust, $a_{\mathrm{d},i}$ is the radius of dust, $Q_{i,\nu}$ is the absorption coefficient of dust for a frequency ν, and $M_{\mathrm{d},i}$ is the dust mass of dust. The subscript i donates the dust species (small and large). Since the absorption coefficient Q_i is roughly proportional to dust radius $a_{\mathrm{d},i}$ at infrared wavelength and the dust mass $M_{\mathrm{d},i}$ is proportional to $a_{\mathrm{d},i}^3$, the absorption coefficient $\alpha_{\mathrm{d},\nu}$ is roughly proportional to the total dust mass density $\rho_{\mathrm{total,d}}(=\sum_i \rho_{\mathrm{d},i})$. If the flux density at 14 μm is dominated by the re-emission from hot dust grains at r_{nearBH}, the flux density at 14 μm is roughly proportional to the absorption coefficient at r_{nearBH}. Since the total number density of hot dust has a peak at $\sim r_{\mathrm{nearBH}}$, and hence the flux density at 14 μm should be roughly proportional to the total mass density of hot dust at $\sim r_{\mathrm{nearBH}}$, $(\rho_{\mathrm{dust}}/\rho_{\mathrm{gas}})_{\mathrm{nearBH}}/(\rho_{\mathrm{dust}}/\rho_{\mathrm{gas}})_{\mathrm{init}}$ is roughly proportional to $f_{14/140}/F(L_{\mathrm{IR}}^{\dagger})$ as we have shown in Fig. 4.14.

4.6 Discussions

4.6.1 The size of a dust deficient region

In this section, we derive the radius r_{dust}, inside which dust cannot enter. For simplicity, we assume that the relative velocity between dust and gas ($\Delta v \equiv v_{\mathrm{d}} - v_{\mathrm{g}}$) is equal to the terminal velocity $\Delta v_{\mathrm{terminal}}$ [3] and the maximum accretion speed of gas is equal to the free-fall speed ($|v_{\mathrm{free}}| \equiv \sqrt{GM_{\mathrm{BH}}/r_{\mathrm{dis}}}$, where r_{dis} the distance from a BH). From our definition, the terminal velocity $\Delta v_{\mathrm{terminal}}$ becomes

$$\Delta v_{\mathrm{terminal}} = \frac{f_{\mathrm{rad}}}{K_{\mathrm{d}}}, \tag{4.20}$$

where f_{rad} is the radiation pressure gradient force on dust. $|\Delta v_{\mathrm{terminal}}| < |v_{\mathrm{acc}}|$ for $r_{\mathrm{dis}} \to \infty$. If the magnitude of free-fall velocity becomes smaller than the magnitude of terminal velocity, dust cannot accrete. The relation between $\Delta v_{\mathrm{terminal}}$ and the radius r_{dust}, therefore, can be derived as follows:

$$\Delta v_{\mathrm{terminal}} = \sqrt{\frac{GM_{\mathrm{BH}}}{r_{\mathrm{dust}}}}. \tag{4.21}$$

From equation (4.4), (4.20), and (4.21),

$$r_{\mathrm{dust}} \simeq \left[\left(\sqrt{GM_{\mathrm{BH}}} \rho_{\mathrm{g}} c_{\mathrm{g}}^* \right)^{-1} \left(\frac{8}{3\sqrt{2\pi}} \frac{1}{\phi^2 \ln\Lambda} \right) \left(\frac{L}{4c\pi} \right) \right]^{2/3}, \tag{4.22}$$

where $c_{\mathrm{g}}^* \equiv \sqrt{k_{\mathrm{B}} T_{\mathrm{g}}/m_{\mathrm{p}}}$. In equation (4.22), we assume that Coulomb drag force is stronger than collisional drag force, the absorption coefficient of dust is unity, the extinction is negligible, $\rho_{\mathrm{d1}} \ll \rho_{\mathrm{g}}$, $\rho_{\mathrm{d2}} \ll \rho_{\mathrm{g}}$, and $\Delta v_{\mathrm{terminal}} \ll c_{\mathrm{g}}^*$. We check that these assumption are consistent with our simulations. For $(n_{\mathrm{H}}, Z, \eta) =$

[3] We assume that the terminal velocity is mainly driven by the radiation pressure on dust and the gas pressure is negligible.

$(100\ \mathrm{cm}^{-3}, 1.0\ \mathrm{Z}_\odot, 0.3)$, we determine the values of the parameters from the simulation (see, Fig. 4.5). We get

$$r_{\rm dust} \sim 6 \times 10^{-2} \left(\frac{M_{\rm BH}}{10^5\ M_\odot}\right)^{1/3} \left(\frac{n_{\rm g}}{6 \times 10^2\ [\mathrm{cm}^{-3}]}\right)^{-2/3} \times \left(\frac{c_{\rm g}^*}{70\ [\mathrm{km/s}]}\right)^{-2/3} \left(\frac{\phi^2 \ln(\Lambda)}{170}\right)^{-2/3} \left(\frac{L}{10^{-2} L_{\rm Edd}}\right)^{2/3} [\mathrm{pc}]. \tag{4.23}$$

The radius $r_{\rm dust}$ is consistent with our simulation results. This is larger than dust sublimation radius in equation (19) of Yajima et al. (2017).

4.7 Conclusions

We have investigated the impact of the relative motion of dust and gas on the accretion rate onto IMBHs with the mass of $10^5\ M_\odot$ by using one-dimensional radiation hydrodynamic simulations in clouds with the initial gas densities of $n_{\rm H} = 10$, 30, and 100 cm^{-3}. To investigate the effect of grain size distribution on the gas accretion, we introduce two additional fluid components which describe large (0.1 μm) and small (0.01 μm) dust grains in the simulations.

We find that the accretion rate is reduced due to the radiation force compared with dust free case. We also find that the dust-to-gas mass ratio significantly changes in H II regions because of the relative motion. The decoupling of dust from gas alleviates the suppression of BH growth compared with the complete coupling case. We show that the time averaged Eddington ratio $\langle f_{\rm Edd}^*(Z) \rangle$ exceeds unity by allowing the relative motion for some cases. If we extrapolate our results to higher density, the relative motion will allow an IMBH of $10^5\ M_\odot$ to grow into an SMBH of $10^9\ M_\odot$ in ~ 1 Gyr even in the dusty environment.

Since the change in the dust-to-gas mass ratio in the vicinity of BHs alters the amount of high-temperature dust, the luminosity at $\lambda \sim 10$ μm can be either brighter or fainter than the luminosity computed by assuming the uniform dust-to-gas mass ratio. For some initial conditions, the radiation pressure significantly decreases the amount of hot dust. This result may explain the lack of high-temperature dust around active galactic nuclei (Jiang et al. 2010; Lyu et al. 2017).

Tazaki & Ichikawa (2020) showed that the effect of sputtering on dust grains affects the abundance of dust grains near massive black holes. In our simulations, we do not include the effect of sputtering on dust grains. We, therefore, may overestimate the amount of dust grains near BHs and underestimate the accretion rate of dusty gas onto BHs.

Chapter 5

Conclusions and Future Prospects

We develop the numerical radiation hydrodynamic code to reveal the effect of radiation pressure from massive stars and black holes in the dusty interstellar medium. We find that the effect of photoionization heating and thermal pressure plays a key role in stellar radiation feedback compared with radiation pressure on dust grains. However, the effect of radiation pressure plays an important role on spatial distribution of dust grains. Radiation pressure leads to relative motion between dust grains and gas and affects dust grain size distribution inside ionized regions. Relative motion between dust grains and gas also affects the dusty gas accretion onto black holes. By assuming relative motion between dust and gas, the accretion rate becomes large compared with completely coupled case.

Our results show that the relative importance of radiation pressure on dust grains decreases comparing with thermal pressure. The effect of radiation pressure on dust grains is, however, even important in BH accretion or spatial distribution of dust grains. We need to consider the dust physics in order to reveal the real effect of dust grains on gas dynamics.

There are following remaining researches for the future work:

1. relative motion between dust grains and gas in galaxy evolutions
2. photoelectric grain heating and dust size evolution

We show that radiation from massive stars causes relative motion between dust grains and gas inside ionized regions. However, we do not discuss the relative motion outside ionized regions. Far-ultraviolet photons ($h\nu < 13.6$ eV) are able to escape from ionization regions. Radiation pressure by far-ultraviolet photons, therefore, may cause relative motion in interstellar medium. Since Bekki et al. (2015) explain the extinction feature in LMC/SMC by removing dust grains, we need to perform numerical simulation allowing relative motion between dust grains and gas in galactic scale to investigate whether we can remove dust grains by radiation pressure from LMC/SMC or not.

In this theme, we do not include the effect of photoelectric grain heating. Photoelectric grain heating is one of the important heating processes in interstellar

medium and Forbes et al. (2016) showed that this process suppress the star formation in dwarf galaxies. However, they assume dust-to-metal ratio as the Milky Way. In low metal regions, dust-to-metal ratio is smaller than the Milky Way (Aoyama et al. 2017) and we may overestimate the effect of photoelectric heating if we assume dust-to-metal ratio as Milky Way. We, therefore, need to perform numerical simulations including the effect of grain size evolution and relative motion between dust and gas to estimate the effect of photoelectric grain heating in dwarf galaxies.

Acknowledgements

First of all, I would like to express my sincere gratitude to examiners, K. Sorai (chief), K. Kuramoto, T. Kobayashi, and T. Okamoto for useful comments. I also heartily appreciate to my supervisor, T. Okamoto. Without his great advise, I could not accomplish my works. I would like to express my gratitude to my collaborators, A. K. Inoue and H. Yajima. By their wonderful advices, I can find the new research topics and improve my works. I also thank T. Hosokawa, H. Hirashita, S. Aoyama, K. Hou, T. Nozawa, K. Omukai, S. Inutsuka, K. Bekki, R. Schneider, H. Kimura, and M. Kirsanova for helpful comments. Especially, T. Hosokawa gives me the advices to recognize my mistakes in my research.

I deeply appreciate helps from my laboratory members. T. Kozasa did the special lecture for me to start my new research about dust physics. K. Sorai gives the good advices for my research and management in laboratory. A. Habe and A. R. Pettitt also give me helpful advices for my research. All other laboratory members also give me great comments to improve my works.

I acknowledge Grant-in-Aid for JSPS Research Fellow (17J04872).

Bibliography

Abel T., Anninos P., Zhang Y., Norman M. L., 1997, New Astron., 2, 181

Agertz O., Kravtsov A. V., Leitner S. N., Gnedin N. Y., 2013, ApJ, 770, 25

Akimkin V. V., Kirsanova M. S., Pavlyuchenkov Y. N., Wiebe D. S., 2015, MNRAS, 449, 440

Akimkin V. V., Kirsanova M. S., Pavlyuchenkov Y. N., Wiebe D. S., 2017, MNRAS, 469, 630

Aldrovandi S. M. V., Pequignot D., 1973, A&A, 25, 137

Alvarez M. A., Wise J. H., Abel T., 2009, ApJ, 701, L133

Anninos P., Zhang Y., Abel T., Norman M. L., 1997, New Astron., 2, 209

Aoyama S., Hou K.-C., Shimizu I., Hirashita H., Todoroki K., Choi J.-H., Nagamine K., 2017, MNRAS, 466, 105

Asano R. S., Takeuchi T. T., Hirashita H., Inoue A. K., 2013a, Earth, Planets, and Space, 65, 213

Asano R. S., Takeuchi T. T., Hirashita H., Nozawa T., 2013b, MNRAS, 432, 637

Asplund M., Grevesse N., Sauval A. J., Scott P., 2009, ARA&A, 47, 481

Aumer M., White S. D. M., Naab T., Scannapieco C., 2013, MNRAS, 434, 3142

Begelman M. C., Volonteri M., Rees M. J., 2006, MNRAS, 370, 289

Bekki K., 2015, MNRAS, 449, 1625

Bekki K., Hirashita H., Tsujimoto T., 2015, ApJ, 810, 39

Benjamin R. A., et al., 2003, PASP, 115, 953

Bertoldi F., Carilli C. L., Cox P., Fan X., Strauss M. A., Beelen A., Omont A., Zylka R., 2003, A&A, 406, L55

Bisbas T. G., et al., 2015, MNRAS, 453, 1324

Bromm V., Loeb A., 2006, ApJ, 642, 382

Brook C. B., Stinson G., Gibson B. K., Wadsley J., Quinn T., 2012, MNRAS, 424, 1275

Cen R., 1992, ApJS, 78, 341

Chini R., Kruegel E., Wargau W., 1987, A&A, 181, 378

Churchwell E., et al., 2006, ApJ, 649, 759

Dale J. E., Bonnell I. A., Whitworth A. P., 2007, MNRAS, 375, 1291

Dale J. E., Ercolano B., Bonnell I. A., 2012, MNRAS, 424, 377

Deharveng L., et al., 2010, A&A, 523, A6

Devecchi B., Volonteri M., 2009, ApJ, 694, 302

Draine B. T., 1978, ApJS, 36, 595

Draine B. T., 2003, ARA&A, 41, 241

Draine B. T., 2011a, Physics of the Interstellar and Intergalactic Medium. Princeton Univ. Press, Princeton, NJ.

Draine B. T., 2011b, ApJ, 732, 100

Draine B. T., Lee H. M., 1984, ApJ, 285, 89

Draine B. T., Salpeter E. E., 1979, ApJ, 231, 77

Draine B. T., Sutin B., 1987, ApJ, 320, 803

Elmegreen B. G., Falgarone E., 1996, ApJ, 471, 816

Falgarone E., Phillips T. G., Walker C. K., 1991, ApJ, 378, 186

Fioc M., Rocca-Volmerange B., 1997, A&A, 326, 950

Fioc M., Rocca-Volmerange B., 1999, astro-ph, 9912179

Forbes J. C., Krumholz M. R., Goldbaum N. J., Dekel A., 2016, Nature, 535, 523

Fukushima H., Yajima H., Omukai K., 2018, MNRAS, 477, 1071

Gail H.-P., Sedlmayr E., 1979a, A&A, 76, 158

Gail H. P., Sedlmayr E., 1979b, A&A, 77, 165

Gould R. J., Salpeter E. E., 1963, ApJ, 138, 393

Haiman Z., 2013, The Formation of the First Massive Black Holes. p. 293, doi:10.1007/978-3-642-32362-1˙6

Harper D. A., Low F. J., 1971, ApJ, 165, L9

Harries T. J., Haworth T. J., Acreman D. M., 2014, Astrophysics and Space Science Proceedings, 36, 395

Hashimoto T., et al., 2019, PASJ, 71, 71

Hirashita H., 2015, MNRAS, 447, 2937

Hirashita H., Inoue A. K., 2019, MNRAS, 487, 961

Hopkins P. F., Quataert E., Murray N., 2011, MNRAS, 417, 950

Hosokawa T., Inutsuka S.-i., 2006, ApJ, 646, 240

Hosokawa T., Omukai K., Yorke H. W., 2012, ApJ, 756, 93

Hosokawa T., Yorke H. W., Inayoshi K., Omukai K., Yoshida N., 2013, ApJ, 778, 178

Hosokawa T., Hirano S., Kuiper R., Yorke H. W., Omukai K., Yoshida N., 2015, arXiv preprint arXiv:1510.01407

Hou K.-C., Hirashita H., Nagamine K., Aoyama S., Shimizu I., 2017, MNRAS, 469, 870

Hummer D. G., 1994, MNRAS, 268, 109

Hummer D. G., Rybicki G. B., 1971, MNRAS, 152, 1

Hummer D. G., Storey P. J., 1998, MNRAS, 297, 1073

Ikeuchi S., Ostriker J. P., 1986, ApJ, 301, 522

Inayoshi K., Omukai K., Tasker E., 2014, MNRAS, 445, L109

Inayoshi K., Haiman Z., Ostriker J. P., 2016, MNRAS, 459, 3738

Inoue A. K., 2002, ApJ, 570, 688

Inoue T., Inutsuka S.-i., 2008, ApJ, 687, 303

Inoue A. K., et al., 2016, Science, 352, 1559

Ishida K., Kawajiri K., 1968, PASJ, 20, 95

Ishiki S., Okamoto T., 2017, MNRAS, 466, L123

Ishiki S., Okamoto T., Inoue A. K., 2018, MNRAS, 474, 1935

Janev R. K., Langer W. D., Post D. E., Evans K., 1987, Elementary Processes in Hydrogen-Helium Plasmas. Springer-Verlag, Berlin

Jiang L., et al., 2010, Nature, 464, 380

Katz N., Furman I., Biham O., Pirronello V., Vidali G., 1999, ApJ, 522, 305

Katz H., Sijacki D., Haehnelt M. G., 2015, MNRAS, 451, 2352

Kennicutt Robert C. J., 1998, ApJ, 498, 541

Kitamura K., Shima E., 2013, Journal of Computational Physics, 245, 62

Krumholz M. R., Matzner C. D., 2009, ApJ, 703, 1352

Krumholz M. R., Klein R. I., McKee C. F., 2007, ApJ, 656, 959

Kuiper R., Yorke H. W., 2013, ApJ, 772, 61

Kuiper R., Klahr H., Dullemond C., Kley W., Henning T., 2010a, A&A, 511, A81

Kuiper R., Klahr H., Beuther H., Henning T., 2010b, ApJ, 722, 1556

Kuiper R., Klahr H., Beuther H., Henning T., 2011, ApJ, 732, 20

Kuiper R., Klahr H., Beuther H., Henning T., 2012, A&A, 537, A122

Laor A., Draine B. T., 1993, ApJ, 402, 441

Larson R. B., 1981, MNRAS, 194, 809

Liou M.-S., 1996, Journal of Computational Physics, 129, 364

Lyu J., Rieke G. H., Shi Y., 2017, ApJ, 835, 257

Mac Low M.-M., Klessen R. S., 2004, Reviews of Modern Physics, 76, 125

Maiolino R., Schneider R., Oliva E., Bianchi S., Ferrara A., Mannucci F., Pedani M., Roca Sogorb M., 2004, Nature, 431, 533

Mathews W. G., 1967, ApJ, 147, 965

Mathis J. S., Rumpl W., Nordsieck K. H., 1977, ApJ, 217, 425

McKee C. F., Ostriker E. C., 2007, ARA&A, 45, 565

Milosavljević M., Couch S. M., Bromm V., 2009, ApJ, 696, L146

Mortlock D. J., et al., 2011, Nature, 474, 616

Murray N., Quataert E., Thompson T. A., 2005, ApJ, 618, 569

Nakano M., Kogure T., Sasaki T., Mizuno S., Sakka K., Wiramihardja S. D., 1983, Ap&SS, 89, 407

Netzer N., Elitzur M., 1993, ApJ, 410, 701

Nozawa T., Kozasa T., Habe A., 2006, ApJ, 648, 435

O'dell C. R., Hubbard W. B., 1965, ApJ, 142, 591

O'dell C. R., Hubbard W. B., Peimbert M., 1966, ApJ, 143, 743

Okamoto T., Yoshikawa K., Umemura M., 2012, MNRAS, 419, 2855

Okamoto T., Shimizu I., Yoshida N., 2014, PASJ, 66, 70

Omukai K., 2001, ApJ, 546, 635

Omukai K., Schneider R., Haiman Z., 2008, ApJ, 686, 801

Oppenheimer B. D., Davé R., 2006, MNRAS, 373, 1265

Osterbrock D. E. F. G. J., 2006, Astrophysics of Gaseous Nebulae and Active Galactic Nuclei, 2nd edn.. University Science Books, Mill Valley, CA.

Paladini R., et al., 2012, ApJ, 760, 149

Park K., Ricotti M., 2011, ApJ, 739, 2

Park K., Ricotti M., 2012, ApJ, 747, 9

Peters T., Banerjee R., Klessen R. S., Mac Low M.-M., Galván-Madrid R., Keto E. R., 2010, ApJ, 711, 1017

Portegies Zwart S. F., McMillan S. L. W., 2002, ApJ, 576, 899

Sales L. V., Marinacci F., Springel V., Petkova M., 2014, MNRAS, 439, 2990

Salpeter E. E., 1955, ApJ, 121, 161

Schlegel D. J., Finkbeiner D. P., Davis M., 1998, ApJ, 500, 525

Simpson R. J., et al., 2012, MNRAS, 424, 2442

Spitzer L., 1978, Physical processes in the interstellar medium. Wiley-Interscience, New York, doi:10.1002/9783527617722

Stinson G. S., Brook C., Macciò A. V., Wadsley J., Quinn T. R., Couchman H. M. P., 2013, MNRAS, 428, 129

Stutzki J., Bensch F., Heithausen A., Ossenkopf V., Zielinsky M., 1998, A&A, 336, 697

Sugimura K., Omukai K., Inoue A. K., 2014, MNRAS, 445, 544

Susa H., Hasegawa K., Tominaga N., 2014, ApJ, 792, 32

Tamura Y., et al., 2019, ApJ, 874, 27

Tanaka S., Yoshikawa K., Okamoto T., Hasegawa K., 2015, PASJ, 67, 62

Tazaki R., Ichikawa K., 2020, arXiv e-prints, p. arXiv:2002.01736

Thorne K. S., 1974, ApJ, 191, 507

Toyouchi D., Hosokawa T., Sugimura K., Nakatani R., Kuiper R., 2019, MNRAS, 483, 2031

Trumpler R. J., 1930, PASP, 42, 214

Venemans B. P., et al., 2012, ApJ, 751, L25

Venemans B. P., et al., 2017, ApJ, 851, L8

Walch S. K., Whitworth A. P., Bisbas T., Wünsch R., Hubber D., 2012, MNRAS, 427, 625

Watson D., Christensen L., Knudsen K. K., Richard J., Gallazzi A., Michałowski M. J., 2015, Nature, 519, 327

Weingartner J. C., Draine B. T., 2001a, ApJS, 134, 263

Weingartner J. C., Draine B. T., 2001b, ApJ, 548, 296

Weingartner J. C., Draine B. T., Barr D. K., 2006, ApJ, 645, 1188

Wise J. H., Abel T., Turk M. J., Norman M. L., Smith B. D., 2012, MNRAS, 427, 311

Wu X.-B., et al., 2015, Nature, 518, 512

Yajima H., Khochfar S., 2016, MNRAS, 457, 2423

Yajima H., Shlosman I., Romano-Díaz E., Nagamine K., 2015, MNRAS, 451, 418

Yajima H., Ricotti M., Park K., Sugimura K., 2017, ApJ, 846, 3

Yorke H. W., Welz A., 1996, A&A, 315, 555

Yoshida N., Omukai K., Hernquist L., 2008, Science, 321, 669

Appendix

A Shock tube tests

In order to investigate whether our method is reliable, we perform shock tube tests. Since the effect of the dust becomes almost negligible in shock tube tests if we assume dust-to-gas mass ratio as 6.7×10^{-3} (the value we assume in our simulations) and hence we will not be able to investigate whether the numerical code is reliable or not, we assume dust-to-gas mass ratio as 1 in the shock tube tests. The initial condition of the shock tube problem is as follows:

$$\begin{aligned} \rho_{\rm g} &= \rho_{\rm d} = \begin{cases} 1, & (x < 0.5), \\ 0.125, & (x > 0.5), \end{cases} \\ P_{\rm g} &= \begin{cases} 1, & (x < 0.5), \\ 0.1, & (x > 0.5), \end{cases} \\ \gamma &= 1.67, \end{aligned}$$

where γ is heat capacity ratio. Since the analytic solutions are known for $K_{\rm d} = 0$ and ∞, we perform test calculations for $K_{\rm d} = 0$ and $K_{\rm d} = 10^{10}$ ($\Delta t_{\rm sim} \gg (\rho_{\rm g}\rho_{\rm d})/(\rho_{\rm d} + \rho_{\rm g})K_{\rm d}^{-1} \equiv t_{\rm d}$), where $\Delta t_{\rm sim}$ is the time scale of the shock tube problem and $t_{\rm d}$ is the drag stopping time. We use linearly spaced 400 meshes between $x = 0$ and 1. Time steps we use for these simulations are $\Delta t = 2.5 \times 10^{-4}$ for $K_{\rm d} = 0$ and $\Delta t = 4.2 \times 10^{-4}$ for $K_{\rm d} = 10^{10}$. The results are shown in Fig. A.1. We confirm that the numerical results agree with the analytic solutions.

B Dust grains with two sizes and gas dynamics

In order to investigate the spatial variation of the grain size distribution inside H II regions, we solve following hydrodynamics equations, where we consider dust

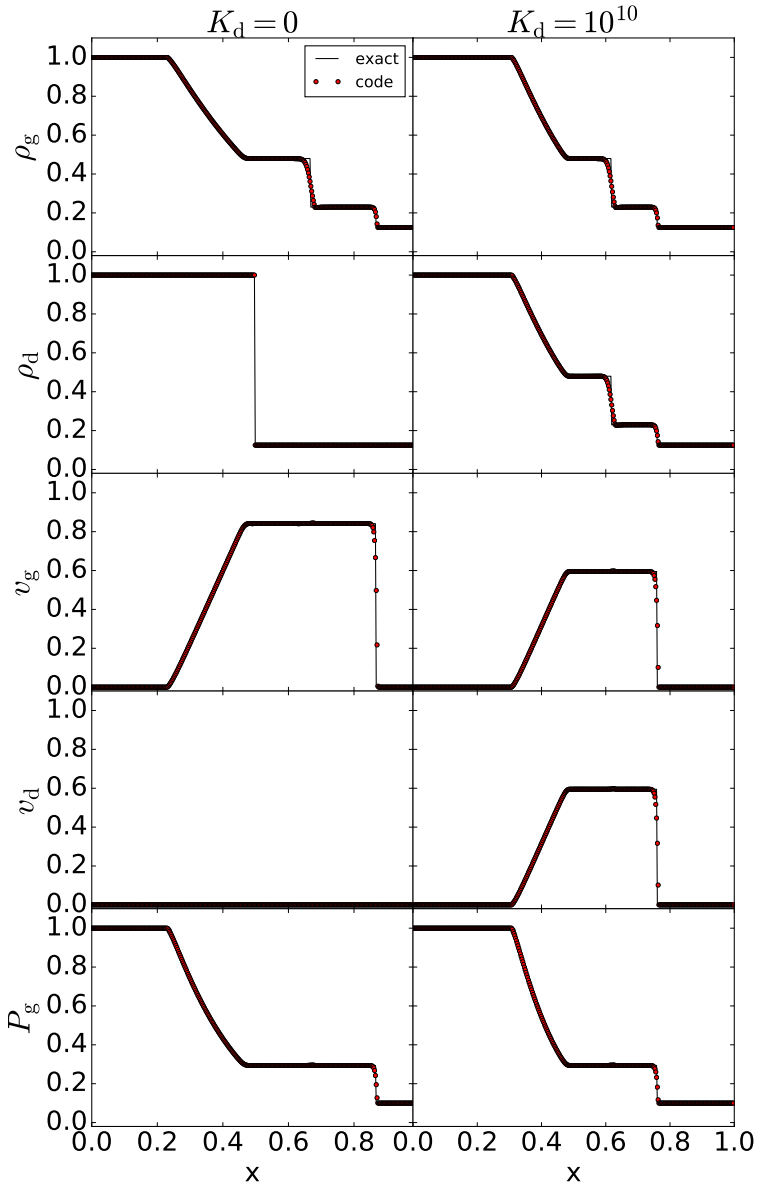

Figure A.1: Gas mass density (top), dust mass density (second from the top), gas velocity (middle), dust velocity (second from the bottom), and pressure (bottom) profiles. In the left and right panels, we show the results for $K_{\rm d} = 0$ and $K_{\rm d} = 10^{10}$, respectively. The red dots indicate the numerical results. The black solid lines at the left panels represent the exact solutions for $K_{\rm d} = 0$. The black solid lines at the right panels represent the exact solutions for $K_{\rm d} = \infty$. For both simulations, we show the results with the adiabatic index $\gamma = 1.67$ at $t = 0.2$.

grains with two sizes (dust-1 and dust-2):

$$
\begin{aligned}
\frac{\partial}{\partial t}\rho_{\rm g} + \frac{\partial}{\partial x}\rho_{\rm g} v_{\rm g} &= 0 \\
\frac{\partial}{\partial t}\rho_{\rm d1} + \frac{\partial}{\partial x}\rho_{\rm d1} v_{\rm d1} &= 0 \\
\frac{\partial}{\partial t}\rho_{\rm d2} + \frac{\partial}{\partial x}\rho_{\rm d2} v_{\rm d2} &= 0 \\
\frac{\partial}{\partial t}\rho_{\rm g} v_{\rm g} + \frac{\partial}{\partial x}\rho_{\rm g} v_{\rm g}^2 &= \rho_{\rm g} a_{\rm gra} + f_{\rm rad,g} - \frac{\partial}{\partial x} P_{\rm g} \\
&\quad + K_{\rm d1}(v_{\rm d1} - v_{\rm g}) + K_{\rm d2}(v_{\rm d1} - v_{\rm g}) \\
\frac{\partial}{\partial t}\rho_{\rm d1} v_{\rm d1} + \frac{\partial}{\partial x}\rho_{\rm d1} v_{\rm d1}^2 &= \rho_{\rm d1} a_{\rm gra} + f_{\rm rad,d1} \\
&\quad + K_{\rm d1}(v_{\rm g} - v_{\rm d1}) \\
\frac{\partial}{\partial t}\rho_{\rm d2} v_{\rm d2} + \frac{\partial}{\partial x}\rho_{\rm d2} v_{\rm d2}^2 &= \rho_{\rm d2} a_{\rm gra} + f_{\rm rad,d2} \\
&\quad + K_{\rm d2}(v_{\rm g} - v_{\rm d2}) \\
\frac{\partial}{\partial t}\left(\frac{1}{2}\rho_{\rm g} v_{\rm g}^2 + e_{\rm g}\right) &+ \frac{\partial}{\partial t}\left(\frac{1}{2}\rho_{\rm d1} v_{\rm d1}^2 + \frac{1}{2}\rho_{\rm d2} v_{\rm d2}^2\right) \\
+\frac{\partial}{\partial x}\left(\frac{1}{2}\rho_{\rm g} v_{\rm g}^2 + h_{\rm g}\right) v_{\rm g} &+ \frac{\partial}{\partial x}\left(\frac{1}{2}\rho_{\rm d1} v_{\rm d1}^3 + \frac{1}{2}\rho_{\rm d2} v_{\rm d2}^3\right) \\
&= \left(\rho_{\rm g} v_{\rm g} + \rho_{\rm d1} v_{\rm d1} + \rho_{\rm d2} v_{\rm d2}\right) a_{\rm gra} \\
&\quad + f_{\rm rad,g} v_{\rm g} + f_{\rm rad,d1} v_{\rm d1} + f_{\rm rad,d2} v_{\rm d2}
\end{aligned}
$$

where $\rho_{\rm d1}$ is the mass density of dust-1, $\rho_{\rm d2}$ is the mass density of dust-2, $v_{\rm d1}$ is the velocity of dust-1, $v_{\rm d2}$ is the velocity of dust-2, $f_{\rm rad,d1}$ is the radiation pressure gradient force on dust-1, $f_{\rm rad,d2}$ is the radiation pressure gradient force on dust-2, $K_{\rm d1}$ is the drag coefficient between gas and dust-1, and $K_{\rm d2}$ is the drag coefficient between gas and dust-2.

In order to solve dust drag force stably, we use following algorithm for the equation of momentum:

$$
\begin{bmatrix}
p_{\rm d1}^* \left(= \rho_{\rm d1}^{\rm t+\Delta t} v_{\rm d1}^*\right) \\
p_g^* \left(= \rho_{\rm g}^{\rm t+\Delta t} v_{\rm g}^*\right) \\
p_{\rm d2}^* \left(= \rho_{\rm d2}^{\rm t+\Delta t} v_{\rm d2}^*\right)
\end{bmatrix}
=
\begin{bmatrix}
p_{\rm d1}^t \\ p_g^t \\ p_{\rm d2}^t
\end{bmatrix}
+
\begin{bmatrix}
F_{\rm p,d1}(\rho_{\rm d1}^t, v_{\rm d1}^t) \\
F_{\rm p,g}(\rho_g^t, v_{\rm g}^t, e_g^t) \\
F_{\rm p,d2}(\rho_{\rm d2}^t, v_{\rm d2}^t)
\end{bmatrix}
\Delta t, \tag{B.1}
$$

$$
\begin{aligned}
&\begin{bmatrix} p_{\mathrm{d1}}^{\mathrm{t+\Delta t}} \\ p_{g}^{\mathrm{t+\Delta t}} \\ p_{\mathrm{d2}}^{\mathrm{t+\Delta t}} \end{bmatrix} \\
&= \begin{bmatrix} \rho_{\mathrm{d1}}^{t+\Delta t} \\ \rho_{\mathrm{g}}^{t+\Delta t} \\ \rho_{\mathrm{d2}}^{t+\Delta t} \end{bmatrix} \frac{p_{\mathrm{d1}}^{*} + p_{\mathrm{g}}^{*} + p_{\mathrm{d2}}^{*}}{\rho_{\mathrm{d1}}^{t+\Delta t} + \rho_{g}^{t+\Delta t} + \rho_{\mathrm{d2}}^{t+\Delta t}} \\
&+ \begin{bmatrix} \rho_{\mathrm{d1}}^{\mathrm{t+\Delta t}} \\ \rho_{g}^{\mathrm{t+\Delta t}} \\ \rho_{\mathrm{d2}}^{\mathrm{t+\Delta t}} \end{bmatrix} \left[a_{\mathrm{gra}} + \frac{f_{\mathrm{d1}} + f_{g} + f_{\mathrm{d2}}}{\rho_{\mathrm{d1}}^{\mathrm{t+\Delta t}} + \rho_{g}^{\mathrm{t+\Delta t}} + \rho_{\mathrm{d2}}^{\mathrm{t+\Delta t}}} \right] \Delta t \\
&+ \begin{bmatrix} \frac{b}{a+x} \\ 1 \\ \frac{c}{d+x} \end{bmatrix} \frac{\rho_{g} \mathrm{e}^{x\Delta t}}{x(x-y)} \left[b(d+x)v_{\mathrm{d1}}^{*} + (a+x)(d+x)v_{g}^{*} + c(a+x)v_{\mathrm{d2}}^{*} \right] \qquad \text{(B.2)} \\
&+ \begin{bmatrix} \frac{b}{a+y} \\ 1 \\ \frac{c}{d+y} \end{bmatrix} \frac{\rho_{g} \mathrm{e}^{y\Delta t}}{y(y-x)} \left[b(d+y)v_{\mathrm{d1}}^{*} + (a+y)(d+y)v_{g}^{*} + c(a+y)v_{\mathrm{d2}}^{*} \right] \\
&+ \begin{bmatrix} \frac{b}{a+x} \\ 1 \\ \frac{c}{d+x} \end{bmatrix} \frac{\mathrm{e}^{x\Delta t} - 1}{x^{2}(x-y)} \left[a(d+x)f_{\mathrm{d1}} + (a+x)(d+x)f_{g} + d(a+x)f_{\mathrm{d2}} \right] \\
&+ \begin{bmatrix} \frac{b}{a+y} \\ 1 \\ \frac{c}{d+y} \end{bmatrix} \frac{\mathrm{e}^{y\Delta t} - 1}{y^{2}(y-x)} \left[a(d+y)f_{\mathrm{d1}} + (a+y)(d+y)f_{g} + d(a+y)f_{\mathrm{d2}} \right],
\end{aligned}
$$

where f_{d1} is the force on dust-1 ($f_{\mathrm{d1}} = f_{\mathrm{rad,d1}}$), f_{d2} is the force on dust-2 ($f_{\mathrm{d2}} = f_{\mathrm{rad,d2}}$),

$$
\begin{aligned}
a &= \frac{K_{\mathrm{d1}}}{\rho_{\mathrm{d1}}^{\mathrm{t+\Delta t}}}, \\
b &= \frac{K_{\mathrm{d1}}}{\rho_{\mathrm{g}}^{\mathrm{t+\Delta t}}}, \\
c &= \frac{K_{\mathrm{d2}}}{\rho_{\mathrm{g}}^{\mathrm{t+\Delta t}}}, \\
d &= \frac{K_{\mathrm{d2}}}{\rho_{\mathrm{d2}}^{\mathrm{t+\Delta t}}}, \\
x &= -\frac{1}{2}\left[(a+b+c+d) + \sqrt{(a+b+c+d)^{2} - 4(ad+ac+bd)} \right],
\end{aligned}
$$

and

$$
y = \frac{(ad+ac+bd)}{x}.
$$

As in section 3.3.4, in order to determine the relative velocity between gas and

dust, we use equation (B.2) which is the exact solution of the following equations:

$$\begin{aligned}
\rho_{\rm d2}\frac{d}{dt}v_{\rm d2} &= f_{\rm rad,d2} + \rho_{\rm d2}a_{\rm gra} + K_{\rm d2}(v_{\rm g} - v_{\rm d2}),\\
\rho_{\rm g}\frac{d}{dt}v_{\rm g} &= f_{\rm rad,g} - \frac{\partial}{\partial x}P_{\rm g} + \rho_{\rm g}a_{\rm gra}\\
&\quad + K_{\rm d1}(v_{\rm d1} - v_{\rm g}) + K_{\rm d2}(v_{\rm d2} - v_{\rm g}),\\
\rho_{\rm d1}\frac{d}{dt}v_{\rm d1} &= f_{\rm rad,d1} + \rho_{\rm d1}a_{\rm gra} + K_{\rm d1}(v_{\rm g} - v_{\rm d1}).
\end{aligned} \tag{B.3}$$

In order to solve momentum equations, we therefore first solve the momentum advection (B.1), and then we solve the exact solution of the equation (B.3) by equation (B.2).

In the case for $|x|\Delta t \ll 1$ or $|y|\Delta t \ll 1$, we use Taylar expansion, $\mathrm{e}^{x\Delta t} \approx 1 + x\Delta t$ or $\mathrm{e}^{y\Delta t} \approx 1 + y\Delta t$, and prevent the numerical error in calculating $(\mathrm{e}^{x\Delta t} - 1)/x$ from becoming too large.

C The terminal velocity approximation

We here show that the terminal velocity approximation may give an unphysical result when the simulation time step Δt is shorter than the drag stopping time $t_{\rm d}$. In order to derive dust velocity and gas velocity, we have used the equation (3.2). On the other hand, Akimkin et al. (2017) used the terminal velocity approximation. When we employ the terminal velocity approximation, the equation (3.2) is transforms into the following form:

$$\begin{aligned}
\begin{bmatrix} p_{\rm d}^{\rm t+\Delta t} \\ p_{\rm g}^{\rm t+\Delta t} \end{bmatrix} &= \begin{bmatrix} \rho_{\rm d}^{\rm t+\Delta t} \\ \rho_{\rm g}^{\rm t+\Delta t} \end{bmatrix} \frac{p_{\rm d}^{*} + p_{\rm g}^{*}}{\rho_{\rm d}^{\rm t+\Delta t} + \rho_{g}^{\rm t+\Delta t}} + \begin{bmatrix} \rho_{\rm d}^{\rm t+\Delta t} \\ \rho_{\rm g}^{\rm t+\Delta t} \end{bmatrix} a_{\rm gra}\Delta t\\
&\quad + \begin{bmatrix} (\rho_{\rm d}^{\rm t+\Delta t}\Delta t + \rho_{\rm g}^{\rm t+\Delta t}t_{\rm d})f_{\rm d} \\ (\rho_{\rm g}^{\rm t+\Delta t}\Delta t + \rho_{\rm d}^{\rm t+\Delta t}t_{\rm d})f_{\rm g} \end{bmatrix} \frac{1}{\rho_{\rm g}^{\rm t+\Delta t} + \rho_{\rm d}^{\rm t+\Delta t}}\\
&\quad + \begin{bmatrix} \rho_{\rm d}^{\rm t+\Delta t}f_{\rm g} \\ \rho_{\rm g}^{\rm t+\Delta t}f_{\rm d} \end{bmatrix} \frac{(\Delta t - t_{\rm d})}{\rho_{\rm g}^{\rm t+\Delta t} + \rho_{\rm d}^{\rm t+\Delta t}}.
\end{aligned} \tag{C.4}$$

The advantage of the equation (3.2) is that it is accurate even for $\Delta t < t_{\rm d}$. In contrast, the equation (C.4) becomes inaccurate for $\Delta t \ll t_{\rm d}$, since the relation of Δt and $t_{\rm d}$ should be $\Delta t \gg t_{\rm d}$ in order the terminal velocity approximation to be valid. For example, the direction of $f_{\rm d}$ on gas and that of $f_{\rm g}$ on dust in the equation (C.4) becomes opposite for $\Delta t < t_{\rm d}$.

We perform simulations by using equation (C.4) in stead of equation (3.2) and compare the simulation results. Simulation results do not largely change for Cloud 2, 3, and 4. The numerical simulation of Cloud 1, however, is crashed, since the timestep becomes $\Delta t \ll t_{\rm d}$ at some steps.

The relation between Δt and $t_{\rm d}$ becomes $\Delta t < t_{\rm d}$ when the drag stopping time $t_{\rm d}$ is larger than the chemical timestep $\Delta t_{\rm chem}$ or the timestep $\Delta t_{\rm CFL}$ defined by Clourant-Friedrichs-Lewy condition. The chemical timestep is defined in equation (7) in Ishiki & Okamoto (2017).

Table C.1: Numerical setup for the IGM, the H II region, and the H I region. The number densities of hydrogen and ionized hydrogen are represented by $n_{\rm H}$ and $n_{\rm H\,II}$. The temperature of gas is represented by $T_{\rm g}$. The radius of a grain is represented by $a_{\rm dust}$. The grain electric potential of dust grains is represented by $V_{\rm d}$. The relative velocity between a dust grain and gas is represented by Δv.

	$n_{\rm H}$ ($\rm cm^{-3}$)	$n_{\rm H\,II}$ ($\rm cm^{-3}$)	$T_{\rm g}$ (K)	$a_{\rm dust}$ (μm)	$V_{\rm d}$ (V)	Δv ($\rm km\ s^{-1}$)
IGM	10^{-5}	10^{-5}	10^4	0.1	20	0
H II region	10	10	10^4	0.1	5	0
H I region	10^2	0	10^2	0.1	0	0

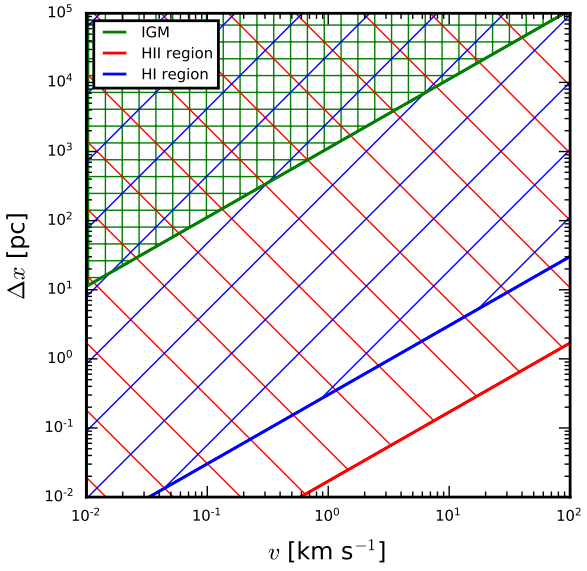

Figure C.2: The green, red, and blue hatched regions represent the condition of $t_{\rm CFL} > t_{\rm d}$ for the IGM, the H II region, and the H I region, respectively.

In Fig. C.2, we present the condition for $t_{\rm CFL}(\equiv \alpha\Delta x/v) > t_{\rm d}$ in the case of the intergalactic medium (IGM), the H II region, and the H I region, where α is constant (we assume $\alpha = 0.1$), Δx is the mesh size, and v is velocity. The details of numerical setup for the IGM, the H II region, and the H I region are listed in Tab C.1. The green, red, and blue hatched regions represent the condition for $t_{\rm CFL} > t_{\rm d}$ for the IGM, the H II region, and the H I region, respectively. If the relation between $t_{\rm CFL}$ and $t_{\rm d}$ becomes $t_{\rm CFL} \ll t_{\rm d}$, the simulation may become unstable.

D Definition of sound speed

The advection term of mass, momentum, and enthalpy $\boldsymbol{F}$ is defined as follows:

$$\boldsymbol{F} \equiv \boldsymbol{F}(\rho, v, \hat{c}, e_{\rm g}), \tag{D.5}$$

where ρ is the mass density, v is the velocity, $\hat{c}$ is the sound speed in numerical simulations, and $e_{\rm g}$ is the specific total energy of gas. In the chapter 4, for the numerical stability, we assume the sound speed of gas $\hat{c}_{\rm g}$, dust-1 $\hat{c}_{\rm d1}$, and dust-2 $\hat{c}_{\rm d2}$ in advection term as follows:

$$\begin{aligned}\frac{1}{c_{\rm g}^2}\begin{bmatrix}\hat{c}_{\rm d1}^2\\ \hat{c}_{\rm g}^2\\ \hat{c}_{\rm d2}^2\end{bmatrix} &= \frac{\rho_{\rm g}}{\rho_{\rm d1}+\rho_g+\rho_{\rm d2}}\begin{bmatrix}1\\1\\1\end{bmatrix}\\ &+ \begin{bmatrix}a(d+x)\\(a+x)(d+x)\\d(a+x)\end{bmatrix}\frac{{\rm e}^{xt}-1}{xt}\frac{1}{x(x-y)}\\ &+ \begin{bmatrix}a(d+y)\\(a+y)(d+y)\\d(a+y)\end{bmatrix}\frac{{\rm e}^{yt}-1}{yt}\frac{1}{y(y-x)},\end{aligned} \tag{D.6}$$

where $c_{\rm g} \equiv \sqrt{\gamma P_{\rm g}/\rho_{\rm g}}$. The definition of x, y, a, b, c, d is same as in Appendix B. We derive this assumption from equation (B.2).

Our new definition has the two features for $(K_{\rm d1}, K_{\rm d2}) \to (\infty, \infty)$ and $(K_{\rm d1}, K_{\rm d2}) \to (0, 0)$. For $(K_{\rm d1}, K_{\rm d2}) \to (\infty, \infty)$,

$$\frac{1}{c_{\rm g}^2}\begin{bmatrix}\hat{c}_{\rm d1}^2\\ \hat{c}_{\rm g}^2\\ \hat{c}_{\rm d2}^2\end{bmatrix} = \frac{\rho_{\rm g}}{\rho_{\rm d1}+\rho_g+\rho_{\rm d2}}\begin{bmatrix}1\\1\\1\end{bmatrix}, \tag{D.7}$$

and for $(K_{\rm d1}, K_{\rm d2}) \to (0, 0)$,

$$\frac{1}{c_{\rm g}^2}\begin{bmatrix}\hat{c}_{\rm d1}^2\\ \hat{c}_{\rm g}^2\\ \hat{c}_{\rm d2}^2\end{bmatrix} = \begin{bmatrix}0\\1\\0\end{bmatrix}. \tag{D.8}$$

Using our sound speed, the advection term $\boldsymbol{F}$ gets the following features: for $(K_{\rm d1}, K_{\rm d2}) \to (\infty, \infty)$, $\frac{\rho_{\rm d1}}{\rho_{\rm d1}+\rho_{\rm g}+\rho_{\rm d2}} = \text{const.}$, and $\frac{\rho_{\rm d2}}{\rho_{\rm d1}+\rho_{\rm g}+\rho_{\rm d2}} = \text{const.}$, [1]

$$\begin{aligned}
&\boldsymbol{F}(\rho_{\rm d1}+\rho_{\rm g}+\rho_{\rm d2}, v, c_{\rm g}\sqrt{\frac{\rho_{\rm g}}{\rho_{\rm d1}+\rho_{\rm g}+\rho_{\rm d2}}}, e_{\rm g}) \\
&= \boldsymbol{F}(\rho_{\rm d1}, v, \hat{c}_{\rm d1}, e_{\rm g}) \\
&+ \boldsymbol{F}(\rho_{\rm g}, v, \hat{c}_{\rm g}, e_{\rm g}) \\
&+ \boldsymbol{F}(\rho_{\rm d2}, v, \hat{c}_{\rm d2}, e_{\rm g}),
\end{aligned} \tag{D.9}$$

and for $(K_{\rm d1}, K_{\rm d2}) \to (0, 0)$,

$$\begin{aligned}
\boldsymbol{F}(\rho_{\rm d1}, v_{\rm d1}, 0, P_{\rm g}) &= \boldsymbol{F}(\rho_{\rm d1}, v_{\rm d1}, \hat{c}_{\rm d1}, P_{\rm g}), \\
\boldsymbol{F}(\rho_{\rm g}, v_{\rm g}, c_{\rm g}, P_{\rm g}) &= \boldsymbol{F}(\rho_{\rm g}, v_{\rm g}, \hat{c}_{\rm g}, P_{\rm g}), \\
\boldsymbol{F}(\rho_{\rm d2}, v_{\rm d2}, 0, P_{\rm g}) &= \boldsymbol{F}(\rho_{\rm d2}, v_{\rm d2}, \hat{c}_{\rm d2}, P_{\rm g}).
\end{aligned} \tag{D.10}$$

On the contrary, if we use assume the sound speed of gas $\hat{c}_{\rm g}$, dust-1 $\hat{c}_{\rm d1}$, and dust-2 $\hat{c}_{\rm d2}$ in advection term as:

$$\frac{1}{c_{\rm g}^2}\begin{bmatrix}\hat{c}_{\rm d1}^2 \\ \hat{c}_{\rm g}^2 \\ \hat{c}_{\rm d2}^2\end{bmatrix} = \begin{bmatrix}0 \\ 1 \\ 0\end{bmatrix}, \tag{D.11}$$

for $(K_{\rm d1}, K_{\rm d2}) \to (\infty, \infty)$, $\frac{\rho_{\rm d1}}{\rho_{\rm d1}+\rho_{\rm g}+\rho_{\rm d2}} = \text{const.}$, and $\frac{\rho_{\rm d2}}{\rho_{\rm d1}+\rho_{\rm g}+\rho_{\rm d2}} = \text{const.}$, the advection term $\boldsymbol{F}$ becomes

$$\begin{aligned}
&\boldsymbol{F}(\rho_{\rm d1}+\rho_{\rm g}+\rho_{\rm d2}, v, c_{\rm g}\sqrt{\frac{\rho_{\rm g}}{\rho_{\rm d1}+\rho_{\rm g}+\rho_{\rm d2}}}, e_{\rm g}) \\
&\neq \boldsymbol{F}(\rho_{\rm d1}, v, 0, e_{\rm g}) \\
&+ \boldsymbol{F}(\rho_{\rm g}, v, c_{\rm g}, e_{\rm g}) \\
&+ \boldsymbol{F}(\rho_{\rm d2}, v, 0, e_{\rm g}),
\end{aligned} \tag{D.12}$$

where advection term must be same for completely coupled case.

By using these definitions (D.6) and the hydrodynamic scheme SLAU2, we perform shock tube test as paper I and confirm that the numerical results agree with the analytic solutions.

E Accretion rate and the metallicity

In order to investigate the effect of metallicity on accretion rate, we perform an additional simulation with $(n_{\rm H}, \eta, Z) = (100\ {\rm cm}^{-3}, 0.1, 0.3\ Z_\odot)$. Fig. E.3 shows the time averaged Eddington ratio as a function of metallicity Z with $(M_{\rm BH}, n_{\rm H}, \eta) = (10^5\ M_\odot, 100\ {\rm cm}^{-3}, 0.1)$. We also present the Eddington ratio by equation (4.12) in Fig. E.3.

[1] The sound speed of complete coupled dusty-gas fluid (i.e. $(K_{\rm d1}, K_{\rm d2}) \to (\infty, \infty)$) becomes $\hat{c} = c_{\rm g}\sqrt{\frac{\rho_{\rm g}}{\rho_{\rm d1}+\rho_{\rm g}+\rho_{\rm d2}}}$.

We find that the difference between the '3-fluid' accretion rate and the '1-fluid' accretion rate becomes small as the metallicity decreases. The Eddington ratios estimated by equation (4.12) also show that the effect of radiation pressure on dust becomes smaller as the dust-to-gas mass ratio decreases. The effect of the relative motion on the accretion rate with low dust-to-gas mass ratio, therefore, becomes week.

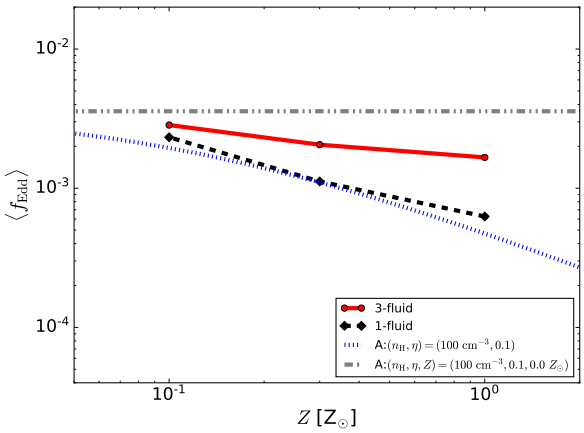

Figure E.3: Time averaged Eddington ratio as a function of metallicity Z. The red solid line with filled circles represents the results of simulations that allow relative motion between dust and gas ('3-fluid'). The black dashed line with filled diamonds represents the results of simulations that assume dust and gas move together ('1-fluid'). The blue dotted line represents the Eddington ratio given by equation (4.12) with $(n_{\rm H}, \eta) = (100\ {\rm cm}^{-3}, 0.1)$. The gray double dot-dashed line represents the Eddington ratio given by equation (4.12) with $(n_{\rm H}, \eta, Z) = (100\ {\rm cm}^{-3}, 0.1, 0.0\ Z_\odot)$.

F Accretion rate and the black hole mass

Park & Ricotti (2012) and Yajima et al. (2017) showed that the Eddington ratio does not change if $n_{\rm g} M_{\rm BH}$ is constant. We, therefore, perform additional simulations and compare the Eddington ratios with $(M_{\rm BH}, n_{\rm H}, \eta, Z) = (10^5\ M_{\rm BH}, 10^2 {\rm cm}^{-3}, 0.3, 1.0\ Z_\odot)$, $(3.33\times10^5 M_{\rm BH}, 30 {\rm cm}^{-3}, 0.3, 1.0\ Z_\odot)$, and $(10^6 M_\odot, 10\ {\rm cm}^{-3}, 0.3, 1.0\ Z_\odot)$ in Fig. F.4. We also present the Eddington ratio by equation (4.12). We find that the Eddington ratio by '3-fluid' does not change much if $n_{\rm g} M_{\rm BH}$ is constant. The simulation results with the different black hole mass also agree well with the analytic estimates.

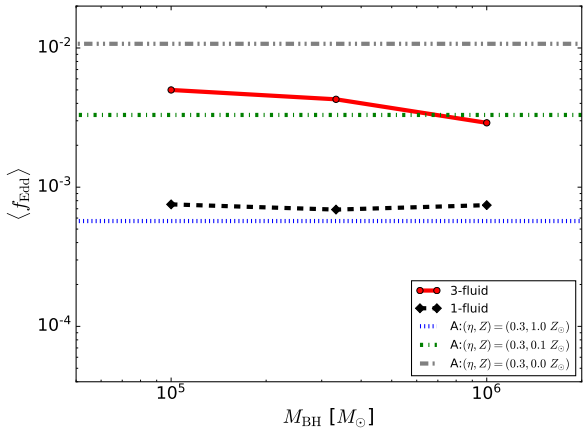

Figure F.4: Time averaged Eddington ratio as a function of black hole mass $M_{\rm BH}$. The red solid line with filled circles represents the results of simulations that allow relative motion between dust and gas ('3-fluid'). The black dashed line with filled diamonds represents the results of simulations that assume dust and gas move together ('1-fluid'). The blue dotted lines, the green dot-dashed lines, and gray double dot-dashed lines represent the Eddington ratio given by equation (4.12) with $(n_{\rm H}, \eta, Z) = (10^7 {\rm cm}^{-3}/(M_{\rm BH}\ [M_\odot]), 0.3, 1.0\ Z_\odot), (10^7 {\rm cm}^{-3}/(M_{\rm BH}\ [M_\odot]), 0.3, 0.1\ Z_\odot)$, and $(10^7 {\rm cm}^{-3}/(M_{\rm BH}\ [M_\odot]), 0.3, 0.0\ Z_\odot)$.